Electronic structure and transport in exotic nanostructures

Tsintzis, Athanasios

2023

Document Version:
Publisher's PDF, also known as Version of record

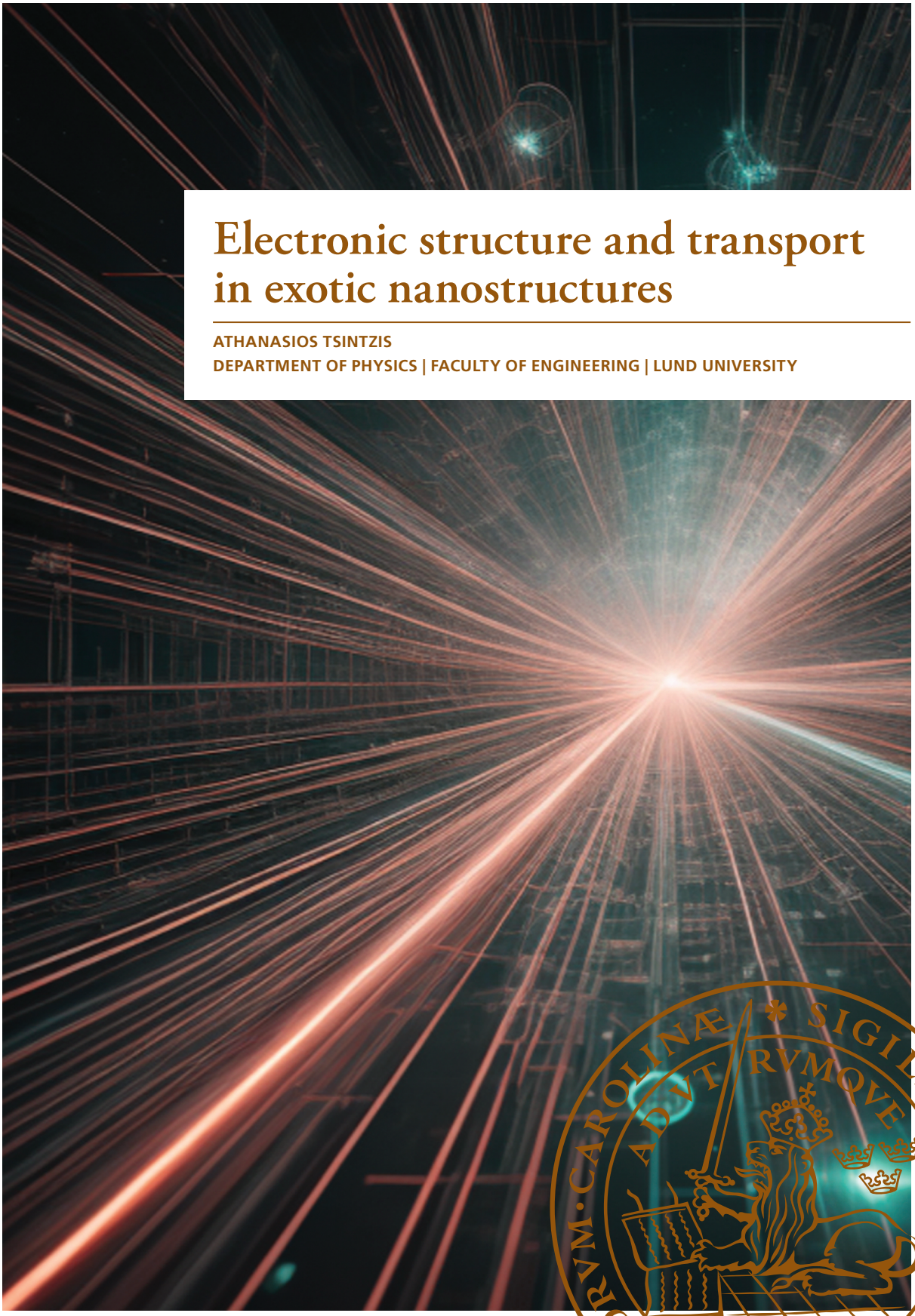

Electronic structure and transport in exotic nanostructures

ATHANASIOS TSINTZIS
DEPARTMENT OF PHYSICS | FACULTY OF ENGINEERING | LUND UNIVERSITY

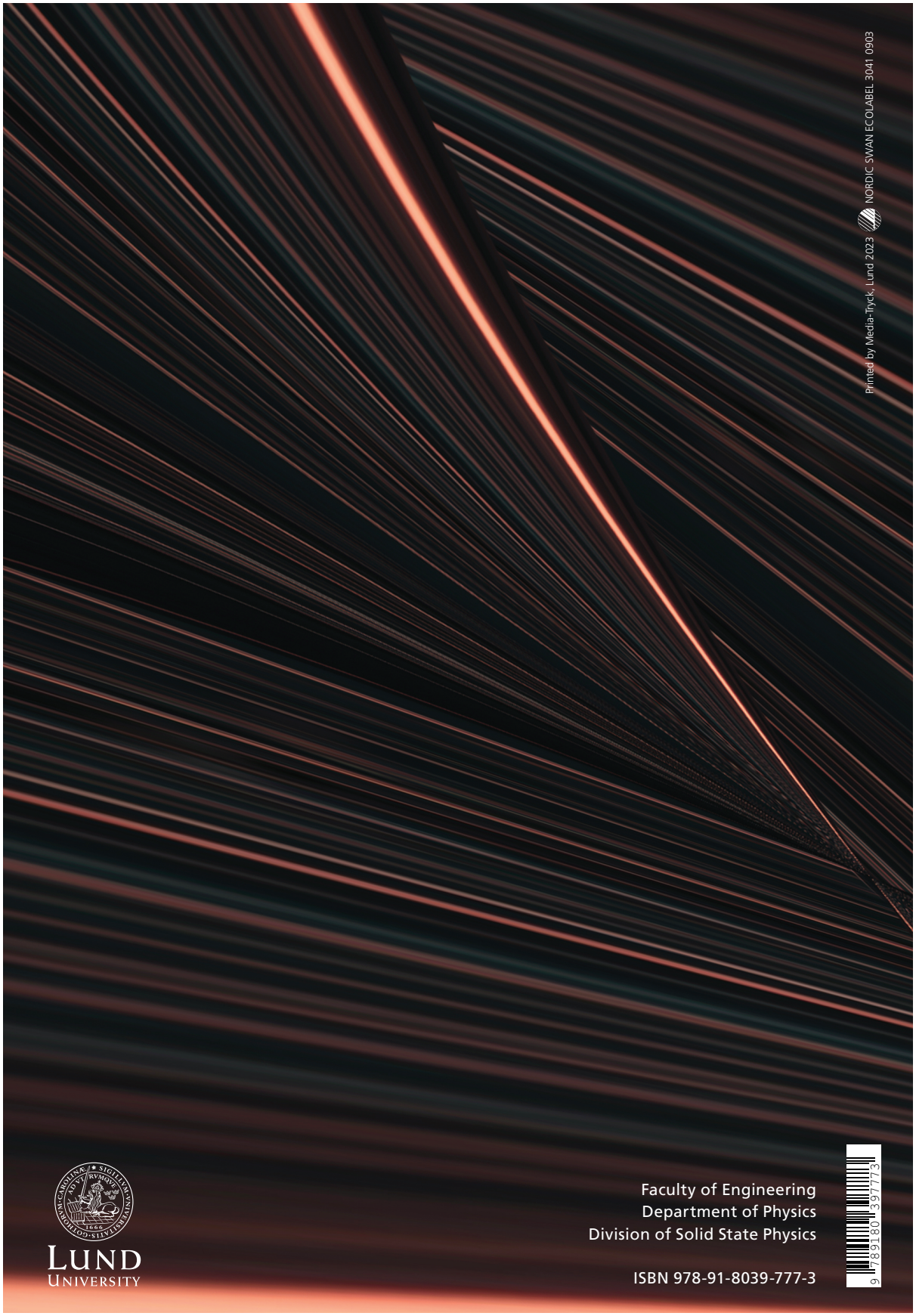

Printed by Media-Tryck, Lund 2023
NORDIC SWAN ECOLABEL 3041 0903

LUND UNIVERSITY

Faculty of Engineering
Department of Physics
Division of Solid State Physics

ISBN 978-91-8039-777-3

Electronic structure and transport in exotic nanostructures

Electronic structure and transport in exotic nanostructures

by Athanasios Tsintzis

LUND
UNIVERSITY

Thesis for the degree of Doctor of Philosophy

To be presented, with the permission of the Faculty of Engineering at Lund University, for public criticism in the Rydberg lecture hall (Rydbergsalen) at the Department of Physics on Friday, the 13th of October 2023 at 09:15.

Thesis advisor
Professor Martin Leijnse

Supporting advisors
Associate Professor Claes Thelander, Professor Ferdi Aryasetiawan

Faculty opponent
Professor Wolfgang Belzig
University of Konstanz, Germany

Organization
LUND UNIVERSITY
Department of Physics
Box 118
SE–221 00 LUND
Sweden

Document name
DOCTORAL DISSERTATION

Date of disputation
2023-10-13

Sponsoring organization

Author(s)
Athanasios Tsintzis

Title and subtitle
Electronic structure and transport in exotic nanostructures

Abstract
This thesis explores the physics of nanostructures involving nanowires, quantum dots, superconductors, and topological insulators. These systems serve as excellent platforms for fundamental physics studies and quantum technology applications.

The introduction contains information on the band structures of crystalline materials and transport phenomena in quantum dots. It is followed by discussions on nanostructures involving superconductors. One-dimensional topological superconductors and Majorana bound states, as well as two-dimensional topological insulators and relevant material systems, are also presented. The theoretical tools used for modeling the various nanostructures are discussed.

The thesis includes six research articles. The first two articles theoretically investigate the possibility of creating high-quality Majorana bound states in a system with two quantum dots coupled via a third quantum dot that is proximitized by a superconductor. The study not only confirms the possibility of creating these states, but also offers a roadmap for their detection, quality assessment, and the demonstration of their nonabelian properties. The third and fourth articles experimentally and theoretically study a parallel-coupled double quantum dot system epitaxially defined in an InAs nanowire. It was found that certain orbital crossings lead to the formation of ring-like states associated with giant g-factors. The same system was studied at higher magnetic fields. The main finding was that, for an increasing magnetic flux through the structure, crossings with ring-like states periodically turn to crossings without ring-like states and vice versa, with a period equal to one flux quantum. The fifth article focused on a similar double quantum dot system coupled to superconducting leads to form a Josephson junction. We found that, control over the hybridization between the quantum dot orbitals can induce a $\pi - 0$ transition in the current-phase relation. In the sixth article, a core/shell/shell InAs/GaSb nanowire was theoretically studied. The study revealed that the structure exhibits a finite hybridization gap and hosts highly-localized end states, which are only partially protected against disorder.

Key words
Nanostructures, electronic structure, quantum transport, nanowires, quantum dots, superconductors, Majorana bound states, topological insulators

Classification system and/or index terms (if any)

Supplementary bibliographical information

Language
English

ISSN and key title

ISBN
978-91-8039-777-3 (print)
978-91-8039-778-0 (pdf)

Recipient's notes

Number of pages
235

Price

Security classification

Signature

Date 2023-08-28

Electronic structure and transport in exotic nanostructures

by Athanasios Tsintzis

LUND
UNIVERSITY

Division of Solid State Physics
Department of Physics
Faculty of Engineering
Lund University

A doctoral thesis at a university in Sweden takes either the form of a single, cohesive research study (monograph) or a summary of research papers (compilation thesis), which the doctoral student has written alone or together with one or several other author(s).

In the latter case the thesis consists of two parts. An introductory text puts the research work into context and summarizes the main points of the papers. Then, the research publications themselves are reproduced, together with a description of the individual contributions of the authors. The research papers may either have been already published or are manuscripts at various stages (in press, submitted, or in draft).

Cover illustration: *Transitions through dimensions* by Vassilis Xenofontos.

Division of Solid State Physics
Department of Physics
Faculty of Engineering
Lund University

Box 118
SE–221 00 LUND
Sweden

ISBN: 978-91-8039-777-3 (print)
ISBN: 978-91-8039-778-0 (pdf)

Printed in Sweden by Media-Tryck, Lund University, Lund 2023

Dedicated to Polyxeni Fitsioula and Eleni Koutsargioti

Contents

List of publications

This thesis is based on the following publications, referred to by their Roman numerals:

I **Creating and detecting poor man's Majorana bound states in interacting quantum dots**
A. Tsintzis, R. S. Souto, and M. Leijnse
Physical Review B 106, L201404 (2022)

I was the main responsible for developing the theoretical model. This involved both analytical and numerical calculations and writing simulation software. I also made all the figures and contributed significantly to the writing.

II **Roadmap towards Majorana qubits and nonabelian physics in quantum dot-based minimal Kitaev chains**
A. Tsintzis, R. S. Souto, K. Flensberg, J. Danon, and M. Leijnse
Manuscript submitted to Physical Review X Quantum (2023)

I was the main responsible for developing the theoretical model in most sections of the paper. This involved both analytical and numerical calculations and writing simulation software. I also made most of the figures and contributed significantly to the writing.

III **Electrical control of spins and giant g-factors in ring-like coupled quantum dots**
H. Potts, I.-J. Chen, **A. Tsintzis**, M. Nilsson, S. Lehmann, K. A. Dick, M. Leijnse, and C. Thelander
Nature Communications 10, 5740 (2019)

I was the main responsible for developing the tight-binding model and the perturbation theory analysis. This involved analytical calculations and writing simulation software. I was also responsible for writing the corresponding part of the manuscript, as well as a detailed theory section in the supplementary material.

IV **Effects of parity and symmetry on the Aharonov-Bohm phase of a quantum ring**
R. Debbarma, H. Potts, C. J. Stenberg, **A. Tsintzis**, S. Lehmann, K. Dick, M. Leijnse, and C. Thelander
Nano Letters 2022 22 (1), p. 334-339 (2021)

I supervised CJS who performed the theoretical calculations. I also wrote the corresponding part of the manuscript, as well as a detailed theory section in the supplementary material.

V **Supercurrent $\pi - 0$ transition induced by orbital hybridization in a double quantum dot**
R. Debbarma, **A. Tsintzis**, M. Aspegren, R. S. Souto, S. Lehmann, K. Dick, M. Leijnse, and C. Thelander
Manuscript submitted to Physical Review Letters (2023)

I was the main responsible for developing the theoretical model. This involved writing simulation software. I was also responsible for writing the corresponding part of the manuscript and the theory section in the supplementary material.

VI **Band structure and end states in InAs/GaSb core-shell-shell nanowires**
F. Viñas Boström, **A. Tsintzis**, M. Hell, and M. Leijnse
Physical Review B 102, 195434 (2020)

I was the main responsible for developing the tight-binding model. This involved analytical calculations and writing simulation software. I was also responsible for writing the corresponding part of the manuscript.

All papers are reproduced with permission of their respective publishers.

Publications not included in this thesis:

Probing Majorana localization in minimal Kitaev chains through a quantum dot
R. S. Souto, **A. Tsintzis**, K. Flensberg, M. Leijnse, and J. Danon
Manuscript in preparation (2023)

Acknowledgements

First and foremost, I would like to express my gratitude to my advisor Martin. During these past years you have been a great source of inspiration for me. Working with you, I have been constantly gaining new insights, not only into physics, but also into how research should be conducted. You have been a supportive, understanding, and pleasant collaborator and your guidance has proven to be invaluable on numerous occasions.

I would also like to thank all my collaborators who have contributed to the projects during my PhD studies, and especially Claes, Florinda, and Rubén. Claes, I have always found the interplay between theory and experiment in our projects to be very intriguing. Florinda, it is always fun and fruitful discussing physics with you. Rubén, I always learn a lot from our discussions, thank you for your support and guidance.

I am also particularly grateful to the former and current members of the Leijnse group not mentioned so far, Martin J., Max N., Simon, William, Morten, Ola, Stephanie, Viktor, Konstantin, and Quinn. Thank you all for creating and maintaining a nice atmosphere in the group. I value our interactions both during work hours and outside the workplace. Special thanks to Stephanie for proofreading the thesis manuscript.

I would also like to thank former and present staff at FTF for maintaining a pleasant workplace and an intriguing research environment. It has been a great pleasure knowing all of you. I particularly want to thank the alumni Jonatan, David, and Sven, for a very fruitful recent collaboration. I also want to thank my current office mates, Frida and Matteo, for being great companions during work hours.

I would also like to express my gratitude to the people in QuSpin for their hospitality during my research visit in Trondheim, especially to Jeroen and Verena. Jeroen, you were a great host and I am happy that we keep working on projects

together. Verena, you made it very easy for me to feel included both at work and in social activities. Extra thanks to Max H., Jacob, and Vemund, I had a lot of fun during our gaming nights and excursions!

During the past two years, I have been visiting QDev in Copenhagen quite often. I would like to thank the people in QDev, and especially Karsten, for giving me the opportunity to participate in very interesting meetings and discussions.

Angeliki, thank you for your support, encouragement, and guidance during my PhD studies. I also appreciate your feedback on the thesis manuscript.

Dimitra, you probably cannot be thanked enough, but I'm deeply grateful for your patience and support during my PhD time.

A lot of people I do not meet very often, and who are not directly related to my research, have been very important to me during my PhD time. Tasos, Vassilis X., Thodoris, Vaggoulis, Kostas, Jimbo, Maria, Konstantinos, Nikos, Katerina, Dimitris, Andreas, Stathis, Thanos, and Isidora, thank you for recharging my batteries every time we meet. Extra thanks to Vassilis X. for designing the front and back covers of this thesis. I'm also very grateful for the support of my parents, Vassilis and Christina, and my sister Jenny.

Abstract

This thesis explores the physics of nanostructures involving nanowires, quantum dots, superconductors, and topological insulators. These systems serve as excellent platforms for fundamental physics studies and quantum technology applications.

The introduction contains information on the band structures of crystalline materials and transport phenomena in quantum dots. It is followed by discussions on nanostructures involving superconductors. One-dimensional topological superconductors and Majorana bound states, as well as two-dimensional topological insulators and relevant material systems, are also presented. The theoretical tools used for modeling the various nanostructures are discussed.

The thesis includes six research articles. The first two articles theoretically investigate the possibility of creating high-quality Majorana bound states in a system with two quantum dots coupled via a third quantum dot that is proximitized by a superconductor. The study not only confirms the possibility of creating these states, but also offers a roadmap for their detection, quality assessment, and the demonstration of their nonabelian properties. The third and fourth articles experimentally and theoretically study a parallel-coupled double quantum dot system epitaxially defined in an InAs nanowire. It was found that certain orbital crossings lead to the formation of ring-like states associated with giant g-factors. The same system was studied at higher magnetic fields. The main finding was that, for an increasing magnetic flux through the structure, crossings with ring-like states periodically turn to crossings without ring-like states and vice versa, with a period equal to one flux quantum. The fifth article focused on a similar double quantum dot system coupled to superconducting leads to form a Josephson junction. We found that, control over the hybridization between the quantum dot orbitals can induce a $\pi - 0$ transition in the current-phase relation. In the sixth article, a core/shell/shell InAs/GaSb nanowire was theoretically studied. The study revealed that the structure exhibits a finite hybridization gap and hosts highly-localized end states, which are only partially protected against disorder.

Popular science summary

This thesis focuses on the electronic properties of nanostructures, which are systems with dimensions ranging from around 1 to 1000 nanometers. Due to their small sizes, classical physics fails to fully explain the unique properties exhibited by these structures, which are more appropriately described in the framework of quantum mechanics. The electronic states of a nanostructure – meaning, the states of electrons within the structure – can be efficiently manipulated with electric and magnetic fields. Furthermore, nanostructures can be precisely manufactured atom by atom, which grants a high degree of control over their shapes and properties. These inherent characteristics render nanostructures highly appealing for both fundamental physics studies and potential applications.

More complicated nanostructures can be built by combining nanostructures which can be identified as "building blocks". One example of such a building block is a nanowire, a relatively long and thin piece of material in which electrons are free to move along the long dimension but are confined along the other two, significantly shorter dimensions. Another example is a quantum dot, a piece of material so small that the electrons "feel" the confinement effects along all directions. Electrons in quantum dots are not completely immobilized, but, because of this confinement, they are only allowed to occupy a discrete set of energy levels. This electronic structure is similar to the one of atoms, which is why quantum dots are often referred to as "artificial atoms". Another important building block is a superconductor, a material that shows zero electrical resistivity; electrons in a superconductor are allowed to travel unhindered for arbitrarily long distances and times. Some metals exhibit this behavior, undergoing a sudden transition into a superconducting state at low temperatures, where their resistivity becomes exactly zero. Different combinations of nanowires, quantum dots and superconductors offer countless platforms with peculiar and interesting electronic states. These are some of the main building blocks whose combinations lead to new physics phenomena and to pioneering applications in the emerging field of quantum technology. Quantum technology encompasses a wide

range of applications that leverage the unique properties of quantum systems. An example is a quantum computer – a computer that operates with quantum bits, called qubits. Quantum computers can perform certain tasks much faster than classical computers. Another application is quantum cryptography, which introduces heightened security measures in communication protocols, ensuring enhanced protection for sensitive data.

A significant portion of our research efforts concentrates on the theoretical study of a series of three quantum dots. The quantum dots are coupled, meaning that electrons can "hop" from one quantum dot to another. The middle quantum dot is additionally coupled to a superconductor, inheriting some of its properties. We found that the system can be tuned so that exotic states emerge on the outer quantum dots, the so-called Majorana bound states. In the context of condensed matter physics, Majoranas can be viewed as "half-electrons" localized in space (one on each of the outer quantum dots in our case) and can be combined to make a de-localized electron with finite components in both outer quantum dots. We quantify the quality of the Majoranas by calculating how well they are localized in their respective quantum dots, and we propose experimental protocols that could be used to unambiguously distinguish them from other quantum states. Majoranas can, in principle, be used to create qubits and build a quantum computer. It is, in fact, predicted that Majorana qubits are more stable than the qubits of other quantum computing platforms. Additionally, Majoranas are predicted to have properties which have not been exhibited by any other quantum state before. For example, exchanging the positions of two Majoranas two times, the system does not return to its original state as one would expect.

In cooperation with an experimental group, we also studied a double quantum dot embedded in a nanowire. Quantum dots in nanowires can be formed by changing the material along the nanowire axis which results in the formation of thin, disk-like segments. With precise control of the electronic states in the quantum dots the system can be tuned to form quantum rings. This is advantageous because electrons in quantum rings can be more efficiently manipulated with small magnetic fields, which is often desirable as a large magnetic field destroys the superconducting properties. Introducing an additional outer shell in the nanowire, almost perfect quantum rings are formed without the need to fine-tune the system. A similar double quantum dot system was also placed between two superconductors to form a Josephson junction. Josephson junctions consist of two superconductors connected via a small, non-superconducting segment (in our case a double quantum dot) and they are used in various applications including sensitive devices that detect weak magnetic fields and superconducting

quantum computers. We found that the direction of the electrical current in the system (which is the opposite direction of electron hopping from one superconductor into the double quantum dot and into the other superconductor) can be tuned by tuning the coupling between the two quantum dots.

We additionally theoretically studied a core-shell-shell nanowire, a cylindrical nanowire whose core and two shells are built with different materials. One of the shells contained mainly electrons and the other one holes, which are defined as absences of electrons. We found that the electrons and holes from the two shells mix, which leads to the formation of states with both electron and hole components. We also found that the nanowire hosts electronic states localized at its ends. This could be reminiscent of the Majorana bound states discussed above, but there is in fact no relation between these two types of states.

The results of our work could facilitate demonstrating the exotic properties of Majoranas in the near future and the studied nanowires and quantum dots could, in the long run, constitute integral ingredients of exciting technological applications.

Populärvetenskaplig sammanfattning

Denna avhandling fokuserar på de elektroniska egenskaperna hos nanostrukturer, vilka är system med dimensioner som sträcker sig från cirka 1 till 1000 nanometer. Eftersom de är så små misslyckas klassisk fysik med att fullständigt förklara de unika egenskaperna som dessa strukturer uppvisar, vilka mer lämpligen beskrivs med hjälp av kvantmekanik. Nanostrukturer ger fysiker möjlighet att effektivt manipulera deras elektroniska tillstånd – det vill säga elektronernas tillstånd inom systemet. Dessutom kan nanostrukturer exakt tillverkas atom för atom, vilket ger en hög grad av kontroll över deras former och egenskaper. Dessa inneboende egenskaper gör nanostrukturer mycket attraktiva både för att utforska ny grundläggande fysik och för potentiella tillämpningar.

Mer komplexa nanostrukturer kan byggas genom att kombinera nanostrukturer som kan identifieras som "byggstenar". Ett exempel på en sådan byggsten är en nanotråd, en relativt lång och tunn bit material där elektroner kan röra sig fritt längs den långa dimensionen men är begränsade längs de andra två, betydligt kortare dimensionerna. Ett annat exempel är en kvantprick, en bit material så liten att elektronerna "känner av" begränsningseffekter längs alla riktningar. Elektroner i kvantprickar är inte helt immobiliserade, men på grund av denna begränsning tillåts de bara existera i vissa bestämda energinivåer. Denna elektroniska struktur liknar den hos atomer och därför kallas kvantprickar ofta "konstgjorda atomer". En annan viktig byggsten är en supraledare, ett material som uppvisar noll resistans; elektroner i en supraledare kan färdas obehindrat godtyckligt långa avstånd och tider. Vissa metaller uppvisar dessa egenskaper och genomgår en plötslig övergång till ett supraledande tillstånd vid låga temperaturer, där deras resistans blir exakt noll. Olika kombinationer av nanotrådar, kvantprickar och supraledare erbjuder otaliga plattformar med speciella och intressanta elektroniska tillstånd. Dessa är några av de främsta byggstenarna vars kombinationer leder till nya fysikaliska fenomen och banbrytande tillämpningar

inom det växande området kvantteknologi. Kvantteknologi omfattar en mängd olika tillämpningar som utnyttjar de unika egenskaperna hos kvantsystem. Ett exempel är en kvantdator – en dator som fungerar med kvantbitar istället för klassiska bitar. Kvantdatorer kan utföra vissa uppgifter mycket snabbare än klassiska datorer. En annan tillämpning är kvantkryptografi, som möjliggör nya säkrare kommunikationsprotokoll och säkerställer förbättrat skydd för känsliga data.

En betydande del av den forskning som beskrivs i denna avhandling handlar om teoretiska studier av tre seriellt kopplade kvantprickar. Kopplingen mellan kvantprickarna innebär att elektroner kan "hoppa" från en kvantprick till en annan. Den mellersta kvantpricken är dessutom kopplad till en supraledare och får därmed några av dess egenskaper. Vi har funnit att systemet kan justeras så att exotiska tillstånd uppstår på de yttre kvantprickarna, så kallade Majorana-tillstånd. Inom kondenserad materiens fysik kan Majorana-tillstånd ses som "halva elektroner" som är lokaliserade (en på varje av de yttre kvantprickarna i vårt fall) och kan kombineras för att bilda en icke-lokaliserad elektron med ändliga komponenter i båda yttre kvantprickarna. Vi kvantifierar kvaliteten hos Majorana-tillstånden genom att beräkna hur väl de är lokaliserade i sina respektive kvantprickar, och vi föreslår experimentella protokoll som skulle kunna användas för att entydigt särskilja dem från andra kvanttillstånd. Majorana-tillstånd kan i princip användas för att skapa kvantbitar och bygga en kvantdator. Det finns anledning att tro att kvantbitar som baseras på Majorana-tillstånd är ovanligt stabila. Dessutom förutsägs Majorana-tillstånd ha egenskaper som inte har uppvisats av någon annan typ av kvanttillstånd. Till exempel, om man byter plats på två Majorana-tillstånd två gånger, återvänder inte systemet till sitt ursprungliga tillstånd som man skulle förvänta sig.

I samarbete med en experimentell grupp har vi även studerat en dubbel-kvantprick inbäddad i en nanotråd. Kvantprickar i nanotrådar kan bildas genom att ändra materialet längs nanotrådens axel, vilket resulterar i bildandet av tunna skivliknande segment. Med noggrann kontroll av de elektroniska tillstånden i kvantprickarna kan systemet justeras för att bilda kvantringar. Detta är fördelaktigt eftersom elektroner i kvantringar kan manipuleras mer effektivt med små magnetfält, vilket ofta är önskvärt eftersom ett stort magnetfält förstör de supraledande egenskaperna. Genom att introducera ett ytterligare yttre skal i nanotråden bildas nästan perfekta kvantringar utan behov av finjustering av systemet. Ett liknande system med en dubbel-kvantprick placerades också mellan två supraledare för att bilda en Josephson-övergång. Josephson-övergångar består av två supraledare som är sammankopplade via ett litet icke-supraledande segment (i vårt fall en dubbel-kvantprick) och de används i olika tillämpningar, till exempel för att mäta svaga magnetfält och i supraledande kvantdatorer. Vi

fann att riktningen för den elektriska strömmen i systemet (vilken är motsatt den riktning i vilken elektronerna hoppar från en supraledare till den dubbelkvantpricken och in i den andra supraledaren) kan justeras genom att justera kopplingen mellan de två kvantprickarna.

Vi har dessutom teoretiskt studerat en cylindrisk nanotråd som består av en kärna och två skal byggda av olika material. Ett av skalen innehöll främst elektroner medan det andra innehöll hål, vilka definieras som saknade av elektroner. Vi fann att elektronerna och hålen från de två skalen blandades, vilket ledde till bildandet av tillstånd med både elektron- och hålkomponenter. Vi fann också att nanotråden har elektroniska tillstånd lokaliserade vid sina ändar. Detta kan påminna om de Majorana-tillstånd som diskuterades ovan, men det finns inte någon relation mellan dessa två typer av tillstånd.

Resultaten av vårt arbete kan underlätta att demonstrera Majorana-tillståndens exotiska egenskaper inom en snar framtid och de studerade nanotrådarna och kvantprickarna skulle på sikt kunna utgöra ingredienser i spännande teknologiska tillämpningar.

List of abbreviations

2DEG	2D electron gas
ABS	Andreev bound state
AR	Andreev reflection
BCS	Bardeen-Cooper-Schrieffer
BdG	Bogoliubov-de Gennes
BHZ	Bernevig-Hughes-Zhang
CAR	crossed Andreev reflection
CB	conduction band
CP	Cooper pair
DOS	density of states
DQD	double quantum dot
ECT	elastic cotunneling
HH	heavy hole
LH	light hole
MBS	Majorana bound state
MF	mean field
MNW	Majorana nanowire
MP	Majorana polarization
NR	normal reflection
NW	nanowire
PMM	poor man's Majorana bound state
QD	quantum dot
QP	quasiparticle
QW	quantum well
SEM	scanning electron microscope
SIA	structural inversion asymmetry
SO	spin-orbit
SQUID	superconducting quantum interference device
TB	tight-binding
VB	valence band
WZ	wurtzite
YSR	Yu-Shiba-Rusinov
ZB	zinc blende
ZBW	zero bandwidth

Introduction

Nanowires (NWs), quantum dots (QDs), and quantum wells (QWs) are examples of nanostructures intensively studied in the field of mesoscopic physics [1]. The field lies in the middle of the vast gap between macroscopic physics described by the classical theories (e.g., classical thermodynamics, Newton's laws, etc.) and microscopic physics described by quantum mechanics. In a physical system, an important length scale is set by the de Broglie wavelength, λ_{dB}, of the charge carriers in the system ($\lambda_{\mathrm{dB}} = h/p$, where h is Planck's constant and p is the carrier's momentum). Nanostructures have dimensions that are comparable to the de Broglie wavelenght of their carriers, and quantum confinement effects giving rise to the quantization of the energy spectrum become important. At this scale a microscopic description – even though exact – would be cumbersome, as the dimensions are still too large. As a result, mesoscopic physics has been developed as a separate field with its own formalism and nomenclature. The interest in mesoscopic physics and nanostructures is at least two-fold.

On the one hand, the unique properties of nanostructures have led to various

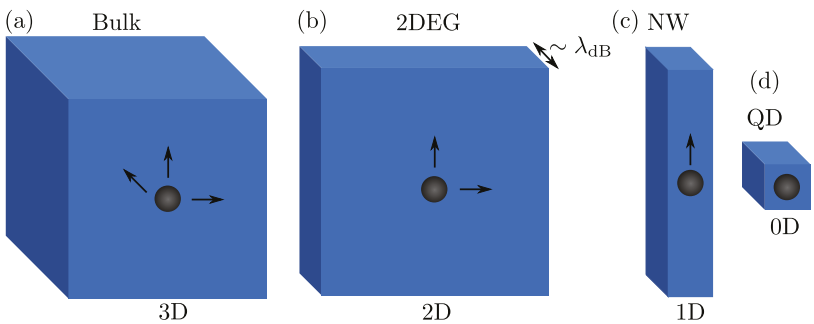

Figure 1: (a) In a bulk system, a carrier (grey ball) can move freely in all three spatial dimensions. (b) If the system's size in one dimension is comparable to the carrier's λ_{dB}, confinement effects along that dimension become important and the system is practically 2D. A 2DEG is an example of such a system. (c) A system confined in two dimensions is effectively 1D. A NW is an example of such a system. (d) In QDs carriers are confined in all three dimensions.

technological applications as they are small enough to exhibit quantum properties but large enough to be manufactured and controlled efficiently. For example, NWs already have various applications in integrated circuits [2] and solar cells [3], while QDs are utilized in opto-electronic applications [4, 5] and have been proposed as platforms for quantum computation with spin qubits [6–8]. Additionally, certain combinations of semiconductor QWs have a topological insulator phase [9–12]. Topological insulators are materials that exhibit an insulating bulk and metallic states at their boundaries and they are important for applications in the field of spintronics [13].

On the other hand, nanostructures offer the opportunity to explore fundamental physics. While macroscopic systems have significant extent in all three dimensions (3D), nanoscale systems can practically be 2D [such as 2D electron gases (2DEGs) in QWs], 1D (NWs) or even 0D (QDs) (see Figure 1), and the idealized concept of a lower-dimensional object can actually be manufactured. QDs are often called artificial atoms [14] because of their point-like dimensions and quantized energy spectrum. In the same spirit, systems with multiple QDs are called artificial molecules and concepts from molecular physics such as bonding and anti-bonding orbitals become relevant in QD spectroscopy.

Introducing superconductivity to nanostructures leads to even richer physics and advanced technological applications. For example, a Josephson junction consists of two superconductors coupled via a narrow non-superconducting segment [15–17]. Josephson junctions are integral parts of superconducting quantum interference devices (SQUIDs) [18] and superconducting quantum computers [19–21]. Another example is a Cooper pair (CP) splitter. CP splitters consist of two QDs coupled to a superconductor and can be used to generate and study CPs that are split into spatially separated entangled electrons [22–29]. Under certain conditions, a semiconductor NW proximitized by a superconductor is predicted to be a 1D topological superconductor [30, 31]. 1D topological superconductors host exotic states at their ends, named Majorana bound states (MBSs) [32–37], which constitute the basis for one of the proposed quantum computing platforms [38–41].

The aim of this thesis is to provide a background on the properties and the theoretical modelling of nanostructures similar to the ones described above and to present the results of our research efforts which are reported in papers I to VI. In the following, a brief description of our research results is given and the thesis outline is presented.

Papers I and II theoretically study a system of two QDs coupled via a third QD which is proximitized by a superconductor. We showed that this system

can host high-quality MBSs which are similar to the ones mentioned above, but only emerge at fine-tuned sweet spots of the parameter space. For this reason they are called poor man's MBSs (PMMs). It was also concluded that it is possible to demonstrate nonabelian physics with PMMs under realistic experimental conditions.

Papers III to V resulted from collaborations with an experimental group. Papers III and IV focus on a double QD (DQD) system which was found to host ring-like states and exhibited giant and electrostatically tunable g-factors. Both these features are advantageous for the efficient manipulation of electronic states in QDs. In paper V a similar DQD was coupled to two superconductors to form a Josephson junction. The main finding of this paper is that the direction of the electrical current through the junction can be controlled through the coupling strength between the two QDs.

In paper VI a core-shell-shell NW was theoretically investigated. The layering of the NW is similar to the layering of QWs in a previously known 2D topological insulator proposal. We found that in this new quasi-1D geometry the topological features survive only partially.

The thesis is organized as follows: The remainder of this introductory chapter highlights important band structure features of crystalline materials and presents transport phenomena in setups involving QDs. The second chapter provides an introduction to properties of superconductors relevant for the work presented in this thesis and discusses processes at the interface between superconducting and non-superconducting materials. Furthermore, the chapter describes various setups involving superconductors, including QD-superconductor hybrids. The third chapter is mostly dedicated to 1D topological superconductors and MBS physics. It begins by introducing a toy model for topological superconductivity and then presents a more realistic model. Experimental signatures of the emergence of the topological phase are also discussed, along with schemes to probe the nonabelian nature of MBSs and a minimal system that hosts PMMs. The fourth chapter focuses on the physics of 2D topological insulators and two material systems suitable for their realization. In the fifth chapter the main theoretical tools used to model the systems under study are covered. This includes a tight-binding (TB) discretization recipe for continuous Hamiltonians, and the chapter concludes with a model for transport through QDs. The sixth chapter provides extended summaries of papers I to VI and the original papers are attached in the final chapter.

1 Band structure of solids

Solving the Schrödinger equation including the interactions between all the electrons and nuclei in a solid state system in order to obtain its energy levels and wavefunctions is a hopelessly complicated task. Various theoretical tools and approximations have been developed in order to circumvent exactly that difficulty [42]. Here we begin with a heuristic approach and consider the simplest possible case of one electron being trapped in a cubic area that represents our solid. For large solid dimensions the electron is practically free and its dispersion is given by the energy-momentum relation $E(k) = \hbar^2 k^2/(2m_e)$, where $k = |\mathbf{k}| = |\mathbf{p}|/\hbar = p/\hbar$. Here, $\mathbf{p}$, $\mathbf{k}$, m_e are the electron's momentum, wavenumber and mass respectively, while $\hbar = h/(2\pi)$ is the reduced Planck's constant. Surprisingly, this simple model turns out to describe metals quite well, at least qualitatively. Metals are good conductors, meaning that under a small bias voltage a current will run through them. In practice, this happens because electrons can be accelerated and gain energy higher than their equilibrium energy which can be accommodated by the fact that the parabolic energy dispersion is continuous and there are no gaps in the energy spectrum. This model cannot explain the electrical resistance of semiconductors and insulators though, which exhibit a suppressed conductance at low temperatures.

A lot can be gained by adding an extra feature to the simple model, namely a periodic potential from the positively charged nuclei in the solid which can be considered to be approximately immobilized. With the use of Bloch's theorem [43] it is found that the available electron states in systems with crystal structure form energy bands while there are also gaps in the spectrum [44, 45]. The characterization of a material as a metal, semiconductor, or insulator can then be done as follows: Placing the electrons in the bands according to the Pauli exclusion principle, the highest energy electron can be within an energy band (unfilled band) or it can just have completed a band (filled band). In the former case, there are higher energy states easily accessible to electrons and the material is a metal. In the latter case, higher energy levels are in the next energy band. If there is a finite gap E_g between the filled band and the next unfilled band, the material is a semiconductor or an insulator. The difference between semiconductors and insulators is a quantitative one and materials with $E_g \lesssim 4$ eV are considered to be semiconductors while materials with $E_g \gtrsim 4$ eV insulators[1]. For insulators and semiconductors, the highest occupied completely filled band is called the valence band (VB) and the next band with available

[1]The terminology used in practice is not always consistent with this classification. Topological insulators usually have band gaps much smaller than 4 eV [46], yet they are still called "insulators".

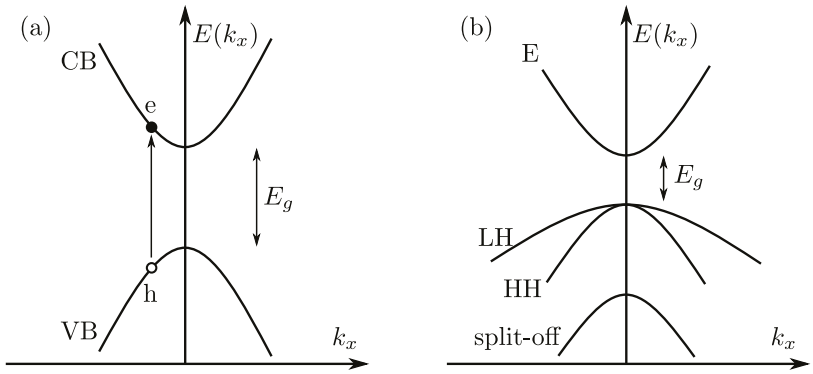

Figure 2: (a) Schematic representation of the VB and CB of a semiconductor with a direct band gap E_g at $k_x = 0$. An electron (e) can be excited from the VB to the CB leaving a hole (h) behind. The CB and VB are often referred to as electron and hole bands respectively. (b) For III-V semiconductors the VB is split to the LH, HH and split-off bands with different curvatures. The CB (E) is also shown.

electron states the conduction band (CB). These concepts are depicted schematically in Figure 2(a), where the energy dispersions of the CB and the VB are plotted with respect to k_x ($k_y = k_z = 0$), $\mathbf{k} = (k_x, k_y, k_z)$ being the Bloch vector. As it is suggestively drawn, the energy dispersions are again parabolic. This is, in fact, approximately the case for many semiconductors and insulators close to the Γ point ($\mathbf{k} = 0$) [47]. The difference is that m_e is replaced by an effective mass given by

$$\Big(\frac{1}{m_n^*(\mathbf{k})}\Big)_{ij} = \frac{1}{\hbar^2}\frac{\partial^2 E_n(\mathbf{k})}{\partial k_i \partial k_j}, \tag{1}$$

where n is the band index. A difference in the effective mass translates to a difference in the curvature of the bands. The dispersions are given by

$$E_{\mathrm{CB}}(k_x) = E_{\mathrm{CB}} + \frac{\hbar^2 k_x^2}{2m_{\mathrm{CB}}^*}, \quad E_{\mathrm{VB}}(k_x) = E_{\mathrm{VB}} + \frac{\hbar^2 k_x^2}{2m_{\mathrm{VB}}^*}, \tag{2}$$

where E_{CB} (E_{VB}) is the minimum (maximum) of energy and m_{CB}^* (m_{VB}^*) the effective mass in the CB (VB). Note that $m_{\mathrm{CB}}^* > 0$ while $m_{\mathrm{VB}}^* < 0$. An electron from the VB can be excited to the CB leaving a hole behind. The VB can then be more easily described as a band occupied by a hole rather than a band that misses one electron. For this reason the VB is frequently referred to as the hole band while the CB as the electron band.

Many of the NWs, QDs, and QWs studied in this thesis are made of compound III-V semiconductors which are created combining elements from Group III (B, Al, Ga, In) and Group V (N, P, As, Sb) of the periodic table. We look at the band structure of III-V semiconductors a bit more closely. The first thing

to note is that the VB in these materials is formed by electrons occupying p atomic orbitals and the CB by electrons from s orbitals [48]. As a result, an extra three-fold degeneracy is introduced in the VB. Second, these materials have very strong spin-orbit (SO) interaction. Electrons moving in the positive ionic background experience an effective magnetic field which couples to the orbital degrees of freedom [49]. This field is referred to as the SO field. The SO field lifts the three-fold degeneracy of the VB leaving three separated VBs, the light hole (LH), heavy hole (HH) and split-off bands [50] shown in Figure 2(b). Note that, in contrast to an external magnetic field, the SO field does not break time-reversal symmetry. This form of the band structure close to the Γ point is in fact also shared by other semiconductors which are important in applications, such as Ge [49] and CdTe [9].

1.1 Confinement effects

As we saw in the previous section, for many semiconductors the energy dispersion of the CB close to the Γ point is approximately parabolic:

$$E_{\mathrm{CB}}^{\mathrm{3D}}(k) - E_{\mathrm{CB}} = \frac{\hbar^2 k^2}{2m_{\mathrm{CB}}^*}. \tag{3}$$

Band-structure calculations assume that the crystal momentum $\mathbf{p} = \hbar\mathbf{k}$ is a good quantum number, which is true for a periodic system with infinite extent along all spatial dimensions. Suppose now that the system is confined in the z direction so that a (practically) 2D system is formed in the xy plane [see Figure 1(b)]. The crystal momentum is not a good quantum number along z any more, the confinement leads to the quantization of energy, and the CB dispersion becomes [51]

$$E_{\mathrm{CB}}^{\mathrm{2D}}(k_x, k_y) - E_{\mathrm{CB}} = E_l + \frac{\hbar^2(k_x^2 + k_y^2)}{2m_{\mathrm{CB}}^*}, \tag{4}$$

where E_l is a discrete set of energy levels with $l = 1, 2, ...$ ($l \in \mathbb{N}$). For each value of l a new parabolic sub-band is introduced, E_l higher in energy than E_{CB}. Further confining the system along y first and along x next for 1D and 0D systems [see Figures 1(c, d)] one obtains

$$E_{\mathrm{CB}}^{\mathrm{1D}}(k_x) - E_{\mathrm{CB}} = E_{ml} + \frac{\hbar^2 k_x^2}{2m_{\mathrm{CB}}^*} \quad \text{and} \quad E^{\mathrm{0D}} = E_{nml}, \tag{5}$$

where E_{ml} and E_{nml} also are discrete sets of energy levels ($n, m, l \in \mathbb{N}$). The spectrum becomes completely discrete for 0D systems like QDs.

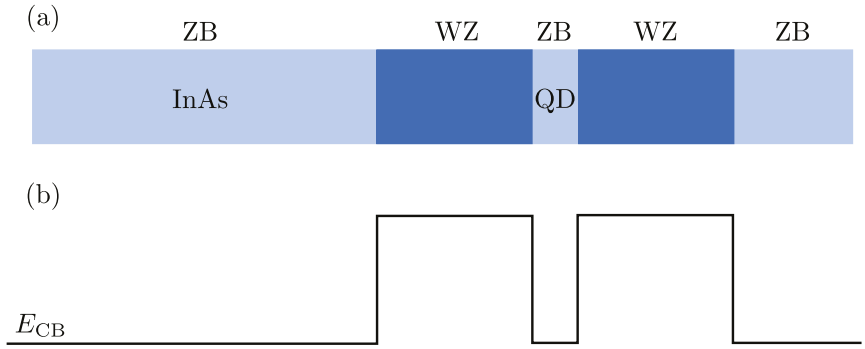

Figure 3: (a) Sketch of a ZB InAs NW with two WZ segments forming a QD. (b) Corresponding band diagram showing the CB edge.

1.2 Epitaxially-defined quantum dots in nanowires

The QDs studied in papers III to V are created in NWs which are quasi-1D structures. Adding two potential barriers along the NW axis, axial confinement is also achieved and the confined area can be considered quasi-0D, a QD. The barriers can either be made of a different material [52] or the same material in a different crystal phase, the latter being the case for the InAs QDs studied in Papers III to V. InAs NWs can be grown in two crystal phases, wurtzite (WZ) and zinc blende (ZB), with different structure and electronic properties (for details see, e.g., Ref. [53]). Figure 3(a) shows a sketch of a NW that takes advantage of this feature in order to form a QD. Two thick, closely-spaced WZ barriers are grown in an otherwise ZB InAs NW and a ZB QD is formed because the CB edge in the ZB phase is lower in energy than the CB edge in the WZ phase [54]. This is more clearly illustrated in the band diagram of Figure 3(b) where the CB edge of the heterostructure is drawn along the NW axis.

2 Transport phenomenology in quantum dots

Spectroscopic information on QDs can be obtained from transport experiments. The standard setting for studying transport through a QD is shown in Figure 4(a). Source (S) and drain (D) contacts are tunnel-coupled to the QD so that electrons can tunnel from S/D to the QD and vice versa. The setup also includes a gate contact (G) which is only capacitively coupled to the QD. In order to calculate the energy levels in the QD, both electrostatic contributions (from the voltages V_S, V_D, V_G and the electrons in the QD) and the energies of single-particle orbitals must be taken into account. The constant interaction

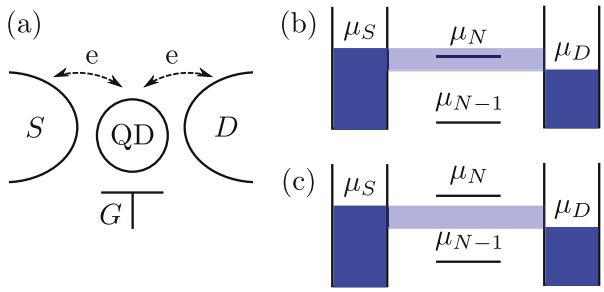

Figure 4: (a) Transport setup for a QD with tunnel-coupled leads S and D and capacitively coupled gate G. (b, c) Energy level diagrams for the transport setup in (a), showing the QD, S, and D chemical potentials. In (b) the QD chemical potential μ_N is in the bias window leading to finite current. The Coulomb blockade regime is depicted in (c); no QD chemical potentials are in the bias window.

model [55, 56] provides an approximate description of the QD spectrum. The basic assumption is that the energies of the many-body states can be calculated by occupying single-particle orbitals with electrons and adding the electrostatic contributions. Here, only the main results are mentioned and rigorous derivations can be found in Refs. [57–59]. In this framework, the QD (electro-)chemical potentials are central quantities. The chemical potential μ_N is defined as the energy required to add one electron to a QD with $N-1$ electrons. We note that the present analysis concerns transitions from the many-body ground state with $N-1$ electrons to the many-body ground state with N electrons and the role of excited many-body states in the QD will be examined in Section 2.2. For total QD energies E_N, E_{N-1}, μ_N is given by

$$\mu_N = E_N - E_{N-1} = \varepsilon_N + \frac{e^2}{C_\Sigma}\left(N - \frac{1}{2}\right) - e\sum_j \alpha_j V_j. \tag{6}$$

In Eq. (6), ε_N is the energy of the single-particle orbital occupied by the Nth electron. For a QD isolated from the environment and without Coulomb interactions, one would have $E_N = \varepsilon_N$ due to confinement alone. The index j runs through $j = S, D, G$ and $-e$ is the electron charge. The quantities $\alpha_j = -C_j/C_\Sigma$ are called lever arms and they quantify the strength of the electrostatic coupling of each contact to the QD, while C_j stands for the capacitance between the QD and contact j. The quantity C_Σ is the self-capacitance of the QD and is equal to $-\sum_j C_j$, so that $\sum_j \alpha_j = 1$. The current through the QD depends on the relative positions of the chemical potentials in the QD and in the contacts S, D. For a finite bias voltage $V_{DS} = V_D - V_S$ an asymmetry in the chemical potentials of the contacts is introduced ($\mu_S - \mu_D = eV_{DS}$). If a QD chemical potential is placed in the bias window as shown in Figure 4(b), electrons can tunnel from S to D through the QD level, leading to a finite current. If there are no QD chemical potentials in the bias window [see Figure 4(c)] there are no available

states for the electrons to travel through the QD and the current is suppressed[2]. The QD is then in the Coulomb blockade regime [60, 61]. The distance between two consecutive chemical potentials is the addition energy:

$$E_{\mathrm{add}}(N) = \mu_N - \mu_{N-1} = \varepsilon_N - \varepsilon_{N-1} + \frac{e^2}{C_\Sigma} = E_{\mathrm{Q}}(N) + U, \tag{7}$$

which naturally consists of a quantum-mechanical part $E_{\mathrm{Q}}(N) = \varepsilon_N - \varepsilon_{N-1}$ and an electrostatic part $U = e^2/C_\Sigma$, the charging energy. For a spin-degenerate QD and for an even N, one has $\varepsilon_N = \varepsilon_{N-1}$ and the addition of the Nth electron only costs U. The states of circularly symmetric systems such as carbon nanotube QDs [62] or ring QDs (see papers III and IV) are four-fold degenerate (due to angular momentum and spin) in the absence of interactions and E_{Q} is finite only for every fourth added electron. The concepts described in this section are crucial to understand the features of a charge stability diagram, which are presented in the following section.

2.1 Charge stability diagrams

When investigating the transport properties of QD systems, it is useful to study charge stability diagrams in order to extract relevant system parameters, such as U and C_Σ. Figure 5 shows a sketch of a charge stability diagram, where the differential conductance dI_D/dV_{DS} is plotted as a function of V_{DS} and V_G. When a QD chemical potential enters the bias window the current increases and a finite differential conductance is measured. Lines with negative (positive) slopes correspond to μ_S (μ_D) aligning with a QD chemical potential. The conductance lines define areas of fixed electron numbers which correspond to the white areas with $N = 0 - 4$, the so-called Coulomb diamonds. The Coulomb diamonds define the Coulomb blockade regimes. The addition energy can be extracted from the width or the height of the Coulomb diamonds. According to the previous section $E_{\mathrm{add}} = U$ at odd-N diamonds and $E_{\mathrm{add}} = E_{\mathrm{Q}}(N) + U$ at even-N ones (for a spin-degenerate QD).

Starting at point A, the QD is in a regime with zero electrons as the chemical potential for having one electron (μ_1) is higher than both μ_S and μ_D, which are aligned for $V_{DS} = 0$. Increasing V_G lowers the QD chemical potentials until μ_1, μ_S, and μ_D are aligned at point C. Any further increase of V_G will cause μ_1 to drop below μ_S and μ_D and the QD to enter the one-electron (1e) regime. At

[2]Note that this analysis is exact at zero temperature. At finite temperatures, electrons in S and D can be found at energy levels above μ_S and μ_D and transport of electrons via the QD can occur even when a QD chemical potential is outside the bias window.

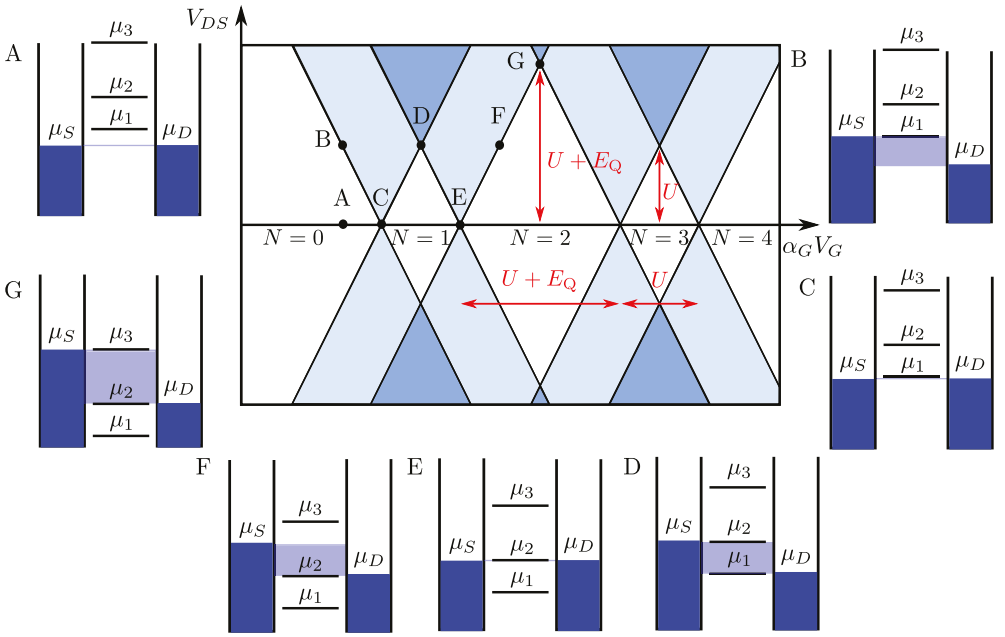

Figure 5: Sketch of the charge stability diagram for a spin-degenerate QD with symmetrically applied bias and equal lever arms for S and D. The black lines correspond to finite differential conductance. Regimes with transport via one and two levels in the QD are denoted with the light blue and darker blue colors respectively. The panels A to G show the energy level diagrams for the points marked in the charge stability diagram.

point E the 2e regime is reached and it is now μ_2 that is aligned with μ_S and μ_D. Starting again from A and going vertically in the direction of increasing V_{DS} this time, the system arrives at point B where μ_1 just enters the bias window from above. Any further increase of V_{DS} will place μ_1 inside the bias window leading to a finite current. Electrons from S can tunnel into the QD and sequentially out to D and the number of electrons in the QD changes between 0 and 1. Regimes that correspond to finite current via one level in the QD are denoted with the light blue color. At point D, μ_1 is aligned with μ_D, and μ_2 is aligned with μ_S. Any further increase of V_{DS} will place both μ_1 and μ_2 inside the bias window leading to a current via both levels. Regimes that correspond to finite current via two levels in the QD are denoted with the darker blue color. The charging energy can be read-off at D as $U = \mu_2 - \mu_1 = \mu_S - \mu_D = eV_{DS}$. Having found U and thus C_Σ, C_G can be calculated through α_G as

$$\alpha_G = \frac{U}{e(V_G^{\mathrm{E}} - V_G^{\mathrm{C}})} \Rightarrow C_G = \frac{e}{V_G^{\mathrm{E}} - V_G^{\mathrm{C}}}\,, \tag{8}$$

where V_G^{C} and V_G^{E} are the gate voltages at points C and E. At point F, it is μ_D that is aligned with μ_2 while at point G the addition energy can be extracted as $E_{\mathrm{add}} = eV_{DS}^{\mathrm{G}}$.

It is worth mentioning that the particularly symmetric diamonds drawn in Figure 5 correspond to the case where the bias voltage is applied symmetrically ($V_S = -V_{DS}/2$, $V_D = V_{DS}/2$) and $\alpha_S = \alpha_D$. In experiments the bias is usually asymmetric ($V_S \neq -V_D$) and the Coulomb diamonds in the corresponding charge stability diagrams are tilted.

2.2 Transport via excited states

Single-electron tunneling processes

Transport experiments in QDs reveal additional features not depicted in Figure 5. Coulomb diamonds describe transitions between ground states, while the many-body quantum states of a QD also include excited states for each electron number N. Figure 6 shows a sketch of the upper half of a Coulomb diamond corresponding to the N-electron ground state of a QD. The red line denotes conductance via an excited N-electron state with chemical potential μ_N^{ex}. Along the red line and within the Coulomb diamond, the bias voltage is not high enough to induce a transition via μ_{N+1}, but it is high enough to access a transport path via μ_N^{ex}. At point A, μ_N^{ex} is aligned with μ_S, and μ_N is aligned with μ_D.

Cotunneling

In all the transport processes described so far, only one electron is involved. Coherent tunneling of two or more electrons also plays a role in transport when the coupling between the QD and the S and D leads is significant. One example of such processes is cotunneling [61, 63]. The process described at point B is elastic cotunneling (ECT). It can take place at any bias voltage and results in background conductance inside the Coulomb diamonds, denoted by the light blue color inside the diamond areas. An electron occupying an orbital can tunnel out to one of the contacts and a second electron can tunnel in from the other contact and occupy the newly available orbital. The initial and the final QD states are identical and the energy is conserved for the whole process. There is a violation of energy conservation in the intermediate state (after electron 1 has tunnelled out and before electron 2 tunnels in), which is allowed for short enough times according to the energy-time uncertainty relation. At point C, the onset of inelastic cotunneling can be seen, denoted by the deeper blue color. In such processes the final state of the QD is different from the initial one. In order to observe inelastic cotunneling, eV_{DS} must be at least equal to $\Delta E = \mu_N^{\text{ex}} - \mu_N$, see the left C panel. Similarly to ECT, an electron initially in the QD can tunnel

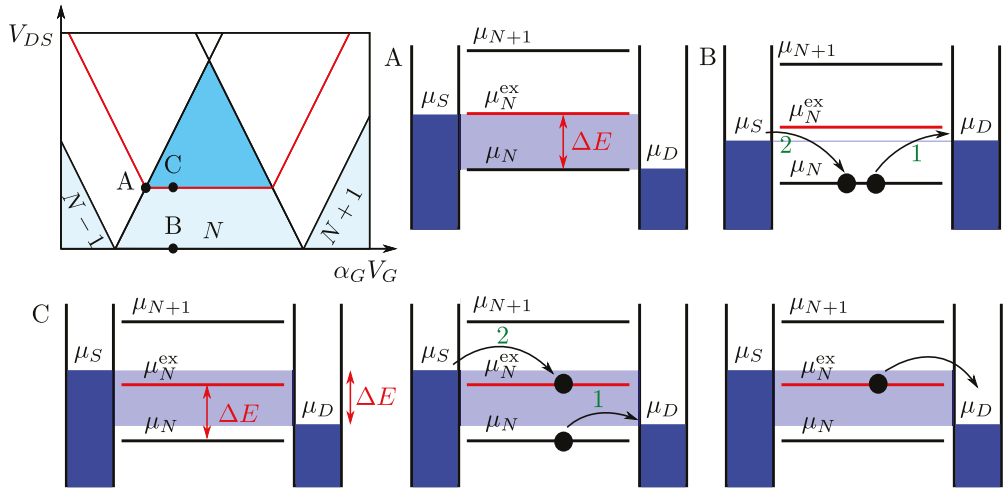

Figure 6: Sketch of the upper half of a Coulomb diamond corresponding to the N-electron ground state of a QD. Transport via an excited N-electron state is denoted with the red line, while the lighter and deeper blue colors depict the regimes with ECT and inelastic cotunneling respectively. The panels A to C depict energy level diagrams for the points marked in the Coulomb diamond. At point A, single-electron tunneling via the excited N-electron state with chemical potential μ_N^{ex} can take place. Panels B and C show ECT and inelastic cottuneling respectively.

out to one of the contacts (electron 1). The difference here is that electron 2 tunnels into the excited state (middle C panel). If the chemical potential of the excited state is in the bias window and the de-excitation rate to the ground state is small, electron 2 can tunnel out to the other side as shown in the right C panel. This process is called cotunneling-assisted single-electron tunneling. QD spectroscopy in the cotunneling regime is heavily employed in papers III and IV in order to obtain information on excited states.

2.3 Parallel-coupled double quantum dots

DQD systems have received a lot of attention because of the possibility to tune and hybridize orbitals belonging to different QDs [64–70]. In serial DQDs, one QD is coupled exclusively to a lead S and the other QD is coupled exclusively to another lead D, while the QDs are additionally coupled to each other. In order to observe single-electron transport at zero-bias voltage the individual QD chemical potentials must be aligned. Reference [71] provides a detailed analysis of the transport properties of serial DQDs and of relevant experimental setups. In parallel-coupled DQDs, both QDs are coupled to both leads and aligning the QD chemical potentials is not required to observe transport. A thorough description of experimental setups and a detailed spectroscopic analysis of parallel-coupled DQD systems in general and epitaxially-defined parallel-coupled DQDs in InAs

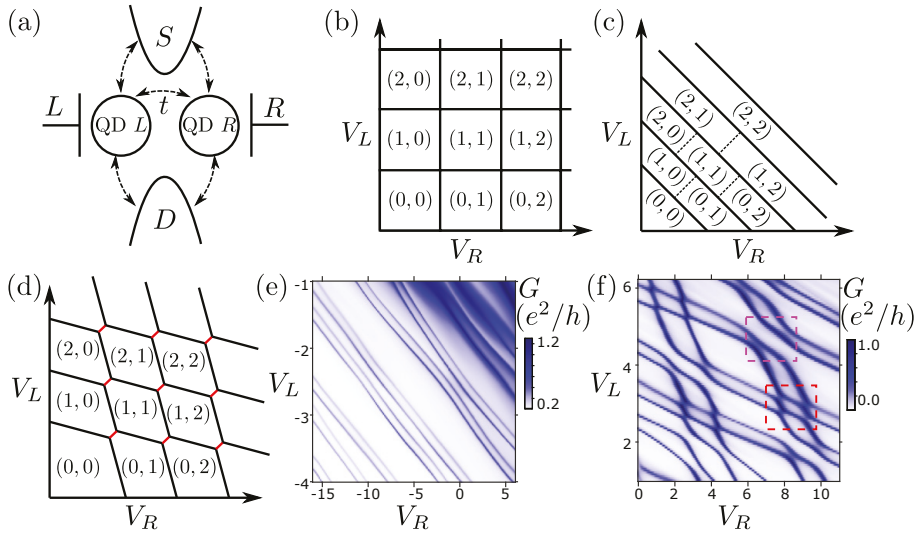

Figure 7: (a) Parallel-coupled DQD setup. QDs L and R are capacitively and tunnel-coupled to S, D, and to each other and only capacitively coupled to gates L and R. (b, c, d) Sketch of the charge stability diagram for the DQD in the (b) uncoupled, (c) strongly coupled, and (d) intermediate regime. (e, f) Measurements of zero-bias conductance as a function of V_L and V_R for (e) a ring QD and (f) a DQD. In (f), crossings and anti-crossings are highlighted with the red and magenta rectangles respectively. (b, d) are adapted from Ref. [65] and (e, f) from paper IV.

NWs in particular can be found in Ref. [59]. Here, we focus on the parallel-coupled DQD system, which is also the system of focus in papers III to V.

The setup is shown schematically in Figure 7(a). Two QDs – left (L) and right (R) – are capacitively and tunnel-coupled to leads S and D and to each other. Gates L and R are only capacitively coupled to QDs L and R and control their chemical potentials. Cross-capacitances C_{LR} and C_{RL} are also present and affect the electrostatics of the system. The capacitance between contact i and QD j is denoted as C_{ij}, the inter-dot one as C_{int}, while the inter-dot tunnel coupling is quantified by the parameter t. In order to gain insight into conductance measurements in parallel-coupled DQDs we first explore two extreme parameter regimes.

Figure 7(b) shows a sketch of a charge stability diagram at zero bias for $C_{LR} = C_{RL} = C_{\text{int}} = t = 0$ for varying V_L, V_R. The lines separate regimes with different electron numbers (N_L, N_R) in QDs L and R and correspond to the aligning of a chemical potential in QD L (horizontal lines) or QD R (vertical lines) with μ_S and μ_D. As $C_{LR} = C_{RL} = 0$, horizontal (vertical) lines are parallel to the V_R (V_L) axis. One can also find points where regimes that differ by two electrons are degenerate – for example $(0, 0)$ and $(1, 1)$ or $(1, 1)$ and $(2, 2)$ – since $C_{\text{int}} = 0$ and electrons in the one QD do not affect the electrostatics in the other QD.

The other extreme with large C_{LR}, C_{RL}, C_{int}, t is shown in Figure 7(c). In this regime the DQD behaves as one QD with charge $N = N_R + N_L$. All solid lines have a single slope as the individual chemical potentials of the QDs cannot be independently changed. The electrons are not localised and the dashed lines are included to aid the eye for the intermediate case shown in Figure 7(d), where the characteristic DQD honeycomb pattern appears [65]. In this case C_{LR}, C_{RL}, and C_{int} are finite but significantly smaller than $C_{LL(RR)}$. It is also noted that $t \simeq 0$ here and electrons are well-localised in each QD. The red lines connect triple points where three charge states are degenerate. Their length increases with C_{int} and they do not appear in transport experiments as they only denote the limit between having an electron in QD L or R. Crossing these lines in the V_L, V_R parameter space does not change the electron number in the DQD and does not lead to a conductance peak.

Figure 7(e) shows conductance measurements for a single QD from paper IV for comparison with Figure 7(c). Lines with a single slope appear, in agreement to the single QD picture. Note that here, the states come in groups of four because of spin and orbital degeneracy, as the QD is actually ring-shaped. Figure 7(f) shows conductance measurements for a parallel-coupled DQD from the same paper and is included for comparison with Figure 7(d). The honeycomb pattern appears but one also notices that there exist sharp crossings and anti-crossings highlighted with the red and magenta rectangles respectively. The sharp crossings are in agreement with Figure 7(d) and correspond to $t \simeq 0$, whereas the anti-crossings appear in regimes where t is large. See papers III and IV and Section 16 for details.

Nanostructures involving superconductors

3 A glance at the BCS theory of superconductivity

The superconducting state of a material is characterized by the absence of resistivity [72, 73] which leads to dissipationless electric currents called supercurrents. Superconductors are also perfect diamagnets exhibiting the Meissner-Ochsenfeld effect [74]. These properties could be described by early phenomenological models such as the London equations [75] or the Ginzburg-Landau theory of superconductivity [76], but a microscopic theory describing the underlying processes leading to a superconducting state was missing. In 1957, John Bardeen, Leon Cooper, and John Robert Schrieffer proposed the first microscopic theory of superconductivity, the BCS theory [77]. According to the BCS theory, below a critical temperature T_c and for momenta close to the Fermi surface, electrons in a metal can form pairs with opposite momenta and spins, the so-called CPs [78]. The pairing occurs because of effectively attractive electron-electron interactions attributed to interactions between electrons and phonons, which are excitations of the positively charged ionic lattice [79, 80]. The theory admits a mean field (MF) description [81, 82]:

$$H_{\mathrm{BCS}}^{\mathrm{MF}} = \sum_{\mathbf{k}\sigma} \xi_{\mathbf{k}} c_{\mathbf{k}\sigma}^{\dagger} c_{\mathbf{k}\sigma} - \Delta \sum_{\mathbf{k}} c_{\mathbf{k}\uparrow}^{\dagger} c_{-\mathbf{k}\downarrow}^{\dagger} - \Delta^{*} \sum_{\mathbf{k}} c_{-\mathbf{k}\downarrow} c_{\mathbf{k}\uparrow}, \tag{9}$$

where $\xi_{\mathbf{k}} = \varepsilon_{\mathbf{k}} - \mu_{\mathrm{S}}$, $\varepsilon_{\mathbf{k}}$ is the energy dispersion relation in the normal metal state, μ_{S} is the chemical potential of the superconductor, and $c_{\mathbf{k}\sigma}^{\dagger}$ creates an electron with momentum $\mathbf{k}$ and spin $\sigma = \uparrow, \downarrow$. The superconducting order parameter Δ obtains a finite value for temperatures below T_c. In general $\Delta = |\Delta| e^{i\theta}$, where θ is the superconducting phase. When we consider a single superconductor this phase can be gauged away and Δ can be taken to be real. In a system with multiple superconductors this is no longer the case and the phase differences

between the superconductors give rise to interesting phenomena, see Section 4.2. Equation (9) can be written in the diagonal form [82]

$$H_{\mathrm{BCS}}^{\mathrm{MF}} = \sum_{\mathbf{k}\sigma} E_{\mathbf{k}} B_{\mathbf{k}\sigma}^{\dagger} B_{\mathbf{k}\sigma}, \tag{10}$$

in terms of the Bogoliubov operators

$$B_{\mathbf{k}\uparrow} = u_{\mathbf{k}}^{*} c_{\mathbf{k}\uparrow} + v_{\mathbf{k}} c_{-\mathbf{k}\downarrow}^{\dagger}, \quad B_{-\mathbf{k}\downarrow}^{\dagger} = -v_{\mathbf{k}}^{*} c_{\mathbf{k}\uparrow} + u_{\mathbf{k}} c_{-\mathbf{k}\downarrow}^{\dagger}, \tag{11}$$

where

$$|u_{\mathbf{k}}|^2 = \frac{1}{2}\Big(1 + \frac{\xi_{\mathbf{k}}}{E_{\mathbf{k}}}\Big), \quad |v_{\mathbf{k}}|^2 = \frac{1}{2}\Big(1 - \frac{\xi_{\mathbf{k}}}{E_{\mathbf{k}}}\Big), \tag{12}$$

and

$$E_{\mathbf{k}} = \sqrt{\xi_{\mathbf{k}}^2 + |\Delta|^2}. \tag{13}$$

Viewing the electron annihilation operators as creation operators for holes[3], the quasiparticles (QPs) described by the Bogoliubov operators are coherent superpositions of electrons and holes and the quantities $u_{\mathbf{k}}$, $v_{\mathbf{k}}$ are the coherence factors. The BCS ground state is characterized by the absence of QPs. The energy required to add a QP to the system is $E_{\mathbf{k}}$. Comparing this to the normal metal case, where adding an electron costs $\xi_{\mathbf{k}}$ and removing an electron (or adding a hole) costs $-\xi_{\mathbf{k}}$, we see that a superconducting gap of $2|\Delta|$ between $E_{\mathbf{k}}$ and $-E_{\mathbf{k}}$ is present around μ_{S} at the Fermi momentum $\mathbf{k} = \mathbf{k}_{\mathrm{F}}$ where $\xi_{\mathbf{k}} = 0$. The QPs in a superconductor are more electron-like for $k \equiv |\mathbf{k}| > k_{\mathrm{F}}$ ($\xi_{\mathbf{k}} > 0$) and more hole-like for $k < k_{\mathrm{F}}$ ($\xi_{\mathbf{k}} < 0$), as can be seen from their defining Eqs. (11–12). The minimum energy required to add an electron to the system is $|\Delta|$, whereas to break a CP an energy of at least $2|\Delta|$ is needed as it involves the excitation of two electrons.

From the QP dispersion relation in Eq. (13), the density of states (DOS) in the superconductor $D(E_{\mathbf{k}})$ can be calculated equating the number of QP states in the interval $dE_{\mathbf{k}}$ with the number of electron states in the interval $d\xi_{\mathbf{k}}$, $D(E_{\mathbf{k}})dE_{\mathbf{k}} = D(\xi_{\mathbf{k}})d\xi_{\mathbf{k}}$, which gives

$$D(E_{\mathbf{k}}) = \frac{E_{\mathbf{k}}}{\sqrt{E_{\mathbf{k}}^2 - |\Delta|^2}} D(\xi_{\mathbf{k}}) \quad \text{for} \quad E_{\mathbf{k}} > |\Delta| \quad \text{and} \tag{14}$$

$$D(E_{\mathbf{k}}) = 0 \quad \text{for} \quad E_{\mathbf{k}} < |\Delta|, \tag{15}$$

where the absence of states within the gap was used and only states above μ_{S} were accounted for. Equation (14) exhibits a divergence in the DOS for $E_{\mathbf{k}} = |\Delta|$ and converges to the normal metal 3D DOS ($D(E_{\mathbf{k}}) \propto \sqrt{E_{\mathbf{k}}}$) for $E_{\mathbf{k}} \gg |\Delta|$. Figure 8 highlights many of the concepts described above.

[3]In this context, holes are defined as absences of electrons below the Fermi level in the CB, while in Section 1 they were defined as absences of electrons in the VB.

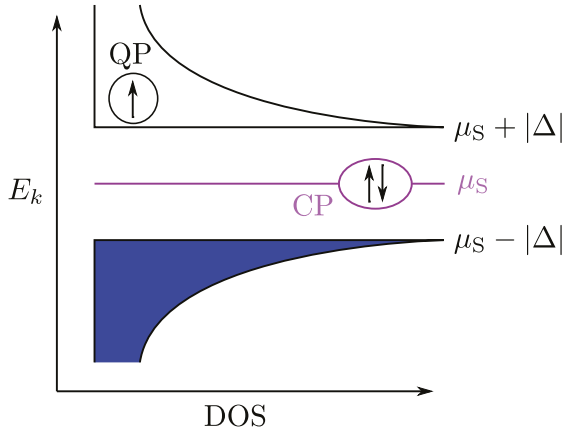

Figure 8: Sketch of the DOS with respect to energy E_k for QPs in a superconductor close to the Fermi level μ_S. The blue (white) color denotes occupied (unoccupied) states. CPs (shown encircled by a purple ellipse) are at the Fermi level of the superconductor μ_S (denoted with the purple line). In order to add a QP (spin in the black circle) to the superconductor, an energy $|\Delta|$ must be paid with respect to μ_S.

4 Superconducting junctions

4.1 Andreev reflection and Andreev bound states

According to the previous section, superconductors are characterized by the absence of states within the superconducting gap. Coupling a superconductor to, for example, a metal in the normal state, this is no longer the case and states with energies below the gap can develop in the combined system [83]. In order to see how sub-gap states come about, it is instructive to look at possible scattering processes close to the interface between a metal in the normal state (N) and a superconductor (S), an NS junction [see Figure 9(a)]. An electron approaching the interface from the N side can be reflected as an electron with the same spin (spin not shown in the Figure). This process is referred to as normal reflection (NR, $1 \rightarrow 2$). There exists another process in which an electron can be reflected as a hole with opposite spin (retroreflection, $1 \rightarrow 2'$). This process is called Andreev reflection (AR) [84, 85]. Upon AR a CP is transmitted into the S side. AR is the dominant transport mechanism for electron energies below the gap and it is suppressed for energies above the gap and for non-transparent interfaces [86]. The opposite process in which a hole is reflected as an electron with the subtraction of a CP from the S side is also possible. For a system with an N part sandwiched between two S parts (an SNS junction), one can imagine coherent repeated ARs at the SN and the NS interfaces leading to bound states, similarly to the particle-in-a-box case, see Figure 9(b). These states are called

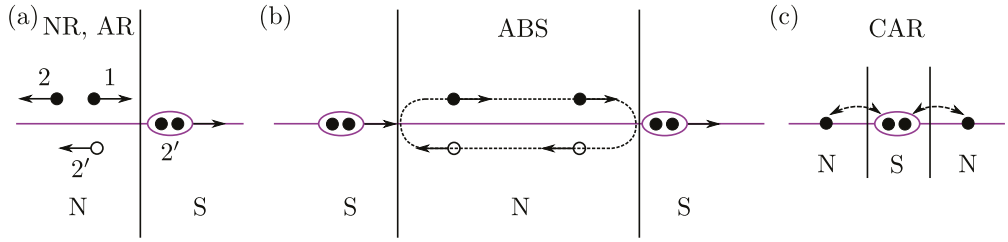

Figure 9: (a) Sketch of an NS junction. Electrons are depicted as filled black dots and holes as unfilled ones, while the arrows point to the direction of the group velocities. Process $1 \to 2$ is NR while $1 \to 2'$ is AR, which includes adding a CP to the S side. (b) Sketch of an SNS junction. Multiple ARs at the right (NS) and the left (SN) interface lead to the formation of ABSs which carry CPs between the two S sides. (c) Sketch of a CP splitter. With CAR the two electrons of a CP are separated and can tunnel into different N parts.

Andreev bound states (ABSs) [87] and they are responsible for the coherent transport of CPs in SNS junctions. For a system with a narrow S part sandwiched between two N parts, crossed AR (CAR) can take place, see Figure 9(c). The two electrons of a CP are separated and can tunnel into different N parts. Controlling and boosting CAR is important for CP splitters [22–29] and for the realization of minimal Kitaev chains [88, 89], see also Section 10 and papers I and II.

4.2 Josephson junctions

A Josephson junction [15–17] is schematically depicted in Figure 10(a). It consists of two superconductors, S_L and S_R, separated by a narrow non-superconducting part which can, for example, be a metal, an insulator, or a QD. We consider equal magnitudes of the order parameters in S_L, S_R, but, in general, different superconducting phases θ_L, θ_R. In a Josephson junction, CPs from S_L can tunnel into S_R and vice versa, giving rise to the so-called Josephson current [15–17]. Within the simplest models, Josephson junctions are governed by the following equations [90, 91]:

$$I(t) = I_c \sin \Theta(t), \tag{16}$$

$$\frac{d\Theta(t)}{dt} = \frac{2e}{\hbar} V(t). \tag{17}$$

In Eq. (16), $I(t)$ is the Josephson current and I_c is the critical current, a quantity characteristic for a Josephson junction. The phase $\Theta(t)$ is given by $\Theta(t) = \theta_{LR}(t) + \delta$, where $\theta_{LR}(t) = [\theta_L - \theta_R](t)$ and δ is the intrinsic phase of the junction. The intrinsic phase can in principle have any value, but in this thesis (and in paper V) we focus on the cases $\delta = 0$ and $\delta = \pi$ which are referred to as a "0-junction" and a "π-junction" respectively. Equation (16) describes the behavior of the junction under two different experiments. First, for a constant

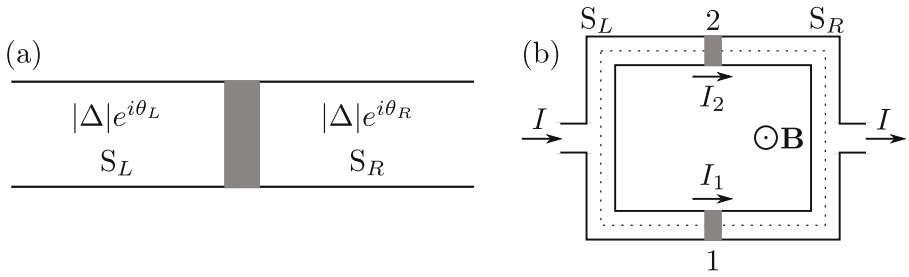

Figure 10: (a) Sketch of a Josephson junction. Two superconductors S_L and S_R with superconducting phases θ_L and θ_R are separated by a narrow, non-superconducting material (gray area). (b) Sketch of a DC SQUID biased with current I and subjected to a magnetic field $\mathbf{B}$. Superconductors S_L and S_R are connected through narrow, non-superconducting parts (shown in gray), forming two Josepshon junctions, 1 and 2.

$\theta_{LR} \neq 0$, a DC current will flow through the junction. For $0 < \theta_{LR} < \pi$, the current flows from S_L to S_R (S_R to S_L) for a $0(\pi)$-junction. The maximum current $|I| = I_c$ develops for $\theta_{LR} = \pi/2$. Second, if one injects a DC current into the junction, a finite, constant θ_{LR} will develop. In the first case, current flow takes place without the appearance of a voltage difference between S_L and S_R. This is also true in the second case, as long as the magnitude of the injected current is smaller than I_c. For $|I| > I_c$, Eq. (16) is no longer valid and a finite voltage difference will also appear.

In Eq. (17), $V(t) = [V_L - V_R](t)$ is the voltage difference between S_L and S_R. Considering a constant V applied on the junction, integration of Eq. (17) gives

$$\Theta(t) = \Theta(0) + \frac{2eV}{\hbar}t, \tag{18}$$

and substituting Eq. (18) in Eq. (16) we get an alternating current with angular frequency $2eV/\hbar$.

Using Eqs. (16) and (17) one can calculate the energy stored in a Josephson junction. With the initial conditions $\Theta(0) = 0$, $I(0) = 0$, the energy stored after current-biasing the junction for time t is

$$E = \int_0^t I(t)V(t)dt = \frac{I_c\hbar}{2e}\int_0^{\Theta(t)} \sin\Theta' d\Theta' = \frac{I_c\hbar}{2e}[1 - \cos\Theta(t)]. \tag{19}$$

Note that the Josephson current can be calculated from this energy as

$$I = \frac{2e}{\hbar}\frac{dE(\Theta)}{d\Theta}. \tag{20}$$

Equation (20) is in fact quite general and valid for any Josephson-type junction with a Θ-dependent thermodynamic potential E [92].

4.3 Superconducting quantum interference devices

SQUIDs are superconducting circuits containing Josephson junctions, see Refs. [18, 81, 91] for detailed descriptions of different SQUID types and their properties. Here, we focus on a DC SQUID with two Josephson junctions, like the one shown in Figure 10(b). A current I is injected from the S_L side and splits in two currents I_1 and I_2 passing through junctions 1 and 2. A perpendicular magnetic field $\mathbf{B}$ can control the current through the system. In the following, we derive an expression that gives the current I as a function of the magnetic flux Φ through the SQUID loop. For the derivation certain assumptions are made. The inductance L of the circuit is considered to be negligible ($LI \approx 0$) and the effect of the magnetic field on the junctions themselves is disregarded. It is also assumed that the injected current is sufficiently small so that $I_1 < I_{c1}$ and $I_2 < I_{c2}$, where I_{c1} and I_{c2} are the critical currents of junctions 1 and 2.

In a superconductor, the change of the superconducting phase along a path $A \to B$ is attributed to the current density $\mathbf{j}$ and the magnetic vector potential $\mathbf{A}$ [91]:

$$\theta_B - \theta_A = \theta_{BA} = -\frac{m_e}{e\hbar n_{\mathrm{CP}}} \int_A^B \mathbf{j} d\mathbf{l} - \frac{2e}{\hbar} \int_A^B \mathbf{A} d\mathbf{l}, \tag{21}$$

where m_e is the electron mass and n_{CP} the density of CPs in the superconductor. If the path is a closed loop, $\theta_{BA} = 2\pi s$ ($s \in \mathbb{Z}$) in order to have a single-valued superconducting phase. Gathering phase contributions along the closed loop shown in Figure 10(b) (dashed line), the current density contribution can be disregarded if the thickness of the circuit is larger than the London penetration depth [75] and the loop is deep in the superconducting bulk. Considering also that the parts of the loop in the non-superconducting (gray) areas of 1 and 2 have negligible length, the vector potential contribution in the counter-clockwise direction is

$$(\theta_{L1} - \theta_{L2}) + (\theta_{R2} - \theta_{R1}) = -\frac{2e}{\hbar} \int_{L2}^{L1} \mathbf{A} d\mathbf{l} - \frac{2e}{\hbar} \int_{R1}^{R2} \mathbf{A} d\mathbf{l} \approx -\frac{2e}{\hbar} \oint \mathbf{A} d\mathbf{l}, \tag{22}$$

where $L(R)1(2)$ is the position of the left (right) edge of the non-superconducting area of junction 1 (2) along the loop. The integral in the last step of the above expression is the magnetic flux Φ through the loop. Including the phase contributions from the junctions, the total phase change along the loop is

$$\theta_{RL1} + \theta_{LR2} - 2\pi \frac{\Phi}{\Phi_0} = -2s\pi \Rightarrow \theta_{LR1} + \theta_{RL2} = 2\pi \left[s - \frac{\Phi}{\Phi_0} \right] \doteq \tilde{\theta}, \tag{23}$$

where $\theta_{RL1(2)} = \theta_{R1(2)} - \theta_{L1(2)} = -\theta_{LR1(2)}$, $\Phi_0 = h/(2e)$ is the superconducting flux quantum, and $s \in \mathbb{Z}$. Without loss of generality, θ_{LR1}, θ_{RL2} can be expressed as $\theta_{LR1} = \tilde{\theta}/2 + \theta_0$, $\theta_{RL2} = \tilde{\theta}/2 - \theta_0$.

For 0-junctions with sinusoidal current-phase relations, I_1 and I_2 are given by

$$I_1 = I_1^0 = I_{c1}\sin(\theta_{LR1}) = I_{c1}\sin\left[\pi\left(s - \frac{\Phi}{\Phi_0}\right) + \theta_0\right], \tag{24}$$

$$I_2 = I_2^0 = I_{c2}\sin(\theta_{LR2}) = -I_{c2}\sin(\theta_{RL2}) = -I_c\sin\left[\pi\left(s - \frac{\Phi}{\Phi_0}\right) - \theta_0\right], \tag{25}$$

while for π-junctions, $I_1 = I_1^\pi = -I_1^0$ and $I_2 = I_2^\pi = -I_2^0$. Thus, different combinations of 0- and π-junctions, lead to a different total current $I = I_1 + I_2$. For intrinsic phases δ_1 and δ_2 corresponding to the junctions 1 and 2, it can be shown that the maximum value of $|I|$ (and thus the critical current for the SQUID) is [18, 93, 94]

$$|I|_{\max} = \sqrt{(I_{c1} - I_{c2})^2 + 4I_{c1}I_{c2}\left|\cos\left(\pi\frac{\Phi}{\Phi_0} + \frac{\delta_1 + \delta_2}{2}\right)\right|^2}. \tag{26}$$

For $\delta_1 = \delta_2 = 0$ both junctions are 0-junctions ($0-0$ SQUID), while for $\delta_1 = 0$, $\delta_2 = \pi$ we have a $0-\pi$ SQUID. From the above expression, we see that $|I|_{\max}$ oscillations are shifted by π for a $0-\pi$ SQUID. This feature is utilized in Paper V to determine whether the SQUID under study is in the $0-0$ or in the $0-\pi$ regime.

5 Quantum dots coupled to superconductors

ABSs do not only form in N parts of SNS junctions. They can also appear as sub-gap localized states in QDs coupled to superconductors. For concreteness, we consider a QD with a single spinful level coupled to a superconductor. The Hamiltonian describing the system is $H_{\rm SQD} = H_{\rm QD} + H_{\rm BCS}^{\rm MF} + H_{\rm T}$. The Hamiltonian $H_{\rm BCS}^{\rm MF}$ is given in Eq. (9) and corresponds to the superconductor, while the QD and the tunneling Hamiltonians are

$$H_{\rm QD} = \sum_\sigma \varepsilon_\sigma n_\sigma + U n_\uparrow n_\downarrow, \tag{27}$$

$$H_{\rm T} = \sum_k t_k^{\rm S} c_{k\sigma}^\dagger d_\sigma + \text{H.c.} \tag{28}$$

In Eq. (27), ε_σ is the energy of the QD single-particle orbital with spin $\sigma = \uparrow, \downarrow$, $n_\sigma = d_\sigma^\dagger d_\sigma$, $d_\sigma^\dagger$ creates an electron with spin σ in the QD and U is the QD charging energy. In Eq. (28), $t_k^{\rm S}$ is the tunneling amplitude between the QD orbitals and the state with momentum k in the superconductor. The magnitude

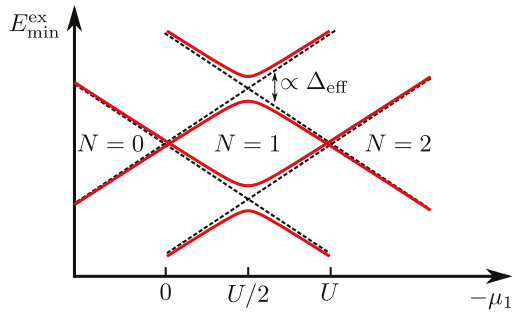

Figure 11: Lowest energy excitations for the combined SQD system and for $U < |\Delta|$ as a function of the negative 1e chemical potential in the QD, $-\mu_1$. The red lines correspond to a QD with an induced superconducting pairing potential $\Delta_{\rm eff}$, while the black dashed lines correspond to $\Delta_{\rm eff} = 0$.

of the charging energy U with respect to the superconducting order parameter $|\Delta|$ determines the nature of the emerging ABSs and two important regimes can be identified [95]. In the following, we describe these regimes qualitatively and provide effective versions of $H_{\rm SQD}$ that adequately capture the physics in each regime.

For $U < |\Delta|$, the QP excitations in the superconductor are high in energy compared to the QD chemical potentials, and the effect of the coupling between the QD and the superconductor can be understood in terms of CPs tunneling in and out of the QD, coupling the 0e and 2e regimes with an induced superconducting pairing $\Delta_{\rm eff}$. Figure 11 shows the minimum excitation energy $E_{\rm min}^{\rm ex}$ for the combined SQD system as a function of the negative 1e QD chemical potential $-\mu_1$ (red lines). The $\Delta_{\rm eff} = 0$ Coulomb diamonds are also shown (black dashed lines). Due to the superconducting pairing, the charge degeneracy at the peak of the $N = 1$ Coulomb diamond is lifted and a state appears within the diamond. For a very strong coupling to the superconductor we have $|\Delta_{\rm eff}| > U$. There is no regime with an 1e ground state in this case and the red-line crossings disappear.

The features described in the above paragraph are captured in the infinite Δ model, a frequently used approximation in QD-superconductor hybrid structures, see Refs. [96–103]. Integrating out the superconductor and taking the limit $|\Delta| \to \infty$, $H_{\rm SQD}$ becomes

$$H_{\rm SQD}^{|\Delta|\to\infty} = \sum_\sigma \varepsilon_\sigma n_\sigma + U n_\uparrow n_\downarrow + \left[\Delta_{\rm eff} d_\uparrow^\dagger d_\downarrow^\dagger + \text{H.c.}\right], \tag{29}$$

where, like in the qualitative analysis above, $\Delta_{\rm eff}$ is the induced superconducting pairing on the QD.

For $U > |\Delta|$, the QP excitations in the superconductor can couple to uncoupled

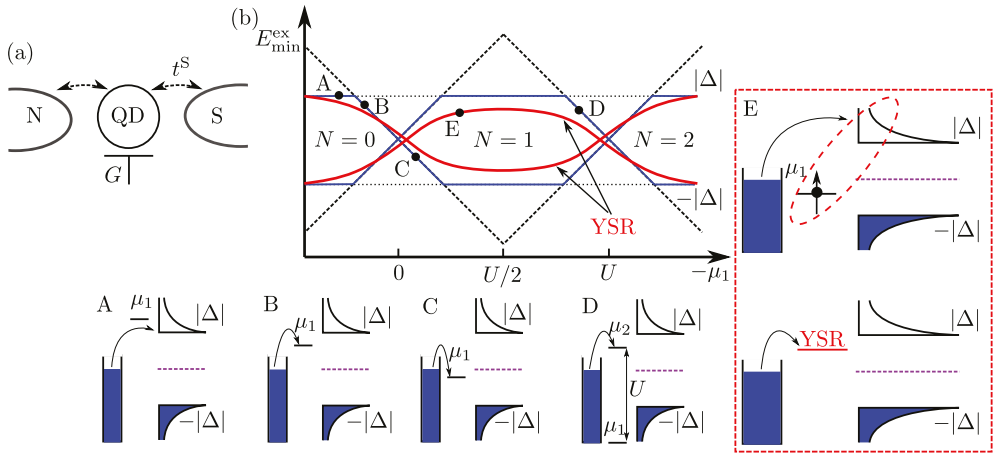

Figure 12: (a) Transport setup that probes the spectrum of the combined SQD system. The QD is tunnel-coupled to a normal lead N and a superconductor S (tunneling amplitude t^S) and capacitively coupled to gate G. (b) Lowest energy excitations for the combined SQD system as a function of the negative 1-electron chemical potential in the QD, $-\mu_1$. The blue lines correspond to $t^S = 0$, the red lines to $t^S \neq 0$, while the black dashed lines to excitations of an isolated QD. The YSR states are the sub-gap states in the $N = 1$ Coulomb diamond and Δ is the superconductor's order parameter. For panels A to E, μ_S is at the purple dashed line.

spins in the QD. The situation is equivalent to having a magnetic impurity in the superconductor which leads to the formation of Yu-Shiba-Rusinov (YSR) states below the superconducting gap [104–106]. The spectrum of the combined SQD system can be studied with a weakly coupled N probe [107, 108], see Figure 12(a). Excitations for the completely uncoupled SQD system correspond to occupying either QD levels or QP states in the superconductor. The minimum energy E^{ex}_{min} for such excitations as a function of the negative 1e QD chemical potential $-\mu_1$ is depicted with the blue lines in Figure 12(b). At point A, $\mu_1 > |\Delta|$ and $E^{ex}_{min} = |\Delta|$. Note that for a completely uncoupled SQD system the process depicted in panel A cannot actually take place and the corresponding line would not appear in a transport experiment. At B and C, $E^{ex}_{min} = \mu_1$ but $\mu_1 > 0$ for B and $\mu_1 < 0$ for C. Finally at D, the system is past the particle-hole symmetric point $\mu_1 = -U/2$ and $E^{ex}_{min} = \mu_2$. For the depicted QD $U > 2|\Delta|$ in fact, so that $E^{ex}_{min} = |\Delta|$ at $\mu_1 = -U/2$. The excitation energies of the opposite processes are also drawn. As the coupling between the QD and the superconductor increases, the exchange interaction between the electron in the QD and the QPs in the superconductor pushes E^{ex}_{min} below $|\Delta|$. For point E, a QP excitation can create a singlet with the QD electron, as shown with the dashed red ellipse in frame E. The reduced E^{ex}_{min} for this singlet can be seen as a YSR state below the gap and YSR excitations are shown in red both in the lower E panel and in the $N = 1$ Coulomb diamond. The diamonds correspond to the minimum excitation energies for an isolated QD.

YSR physics can be captured by employing another approximation for H_{SQD}, the zero-bandwidth (ZBW) approximation [109–112]. The main assumption of the ZBW approximation is that the QD mainly couples to QPs with energy $|\Delta|$. In the ZBW approximation, H_{SQD} becomes

$$H_{\mathrm{SQD}}^{\mathrm{ZBW}} = \sum_{\sigma} \varepsilon_{\sigma} n_{\sigma} + U n_{\uparrow} n_{\downarrow} + \left[\Delta c_{\uparrow}^{\dagger} c_{\downarrow}^{\dagger} + \tilde{t}^{\mathrm{S}} c_{\sigma}^{\dagger} d_{\sigma} + \mathrm{H.c.} \right], \tag{30}$$

where $\tilde{t}^{\mathrm{S}}$ is the renormalized coupling between the QD and the superconductor.

Summarizing this section, coupling a QD to a superconductor results in the appearance of states within the $N = 1$ Coulomb diamond. For $U < |\Delta|$ this happens because of the coupling between the $N = 0$ and $N = 2$ states in the QD and for $U > |\Delta|$ because of the coupling between the $N = 1$ state in the QD and QPs in the superconductor [95].

Majorana bound states in 1D condensed matter systems

In high energy physics, Majorana fermions are elementary chargeless particles that are their own antiparticles [113]. They are described by Hermitian operators and are predicted as special solutions of the Dirac equation. In condensed matter systems, Majoranas are predicted to emerge as collective excitations in topological superconductors and are referred to as MBSs [33–37].

A fermionic operator can, in general, be decomposed in terms of two MBSs as

$$c = \frac{1}{2}(\gamma_A + i\gamma_B), \tag{31}$$

where $\gamma^\dagger_{A(B)} = \gamma_{A(B)}$. The inverse transformation is

$$\gamma_A = c^\dagger + c, \quad \gamma_B = i(c^\dagger - c). \tag{32}$$

From the above equations and the fermionic anticommutation relations, the following MBS properties can be derived:

$$\gamma^2_{A(B)} = 1, \quad \{\gamma_A, \gamma_B\} = \delta_{AB}. \tag{33}$$

MBSs are nonabelian anyons [38–40]; in contrast to ordinary electrons, for example, considering a system of two MBSs and exchanging their positions twice, the system does not return to its original quantum state. Apart from the apparent fundamental physical interest in these properties, the nonabelian nature of MBSs constitutes also the basis of topological quantum computation proposals [38–41].

This chapter focuses on MBSs in 1D condensed matter systems. We begin by showing how MBSs appear in a simple model proposed by Kitaev, the Kitaev chain [32]. Next, we briefly present a theoretical model of a Majorana NW

(MNW) [30, 31], the low-energy sector of which maps onto a continuum version of the Kitaev chain [114], and whose realizations have been in the spotlight of MBS-related experimental activity during the past decade [115–122]. We continue with discussing experimental signatures of MBSs, focusing on local [123–132] and nonlocal [88, 121, 133–138] conductance signatures and MBS quality assessment with the help of an additional QD [118, 139–141]. The nonabelian properties of MBSs and schemes that can be used to probe them [142–150] are the focus of Section 9. The last part of this chapter is dedicated to minimal Kitaev chains, which are predicted to host states similar to MBSs, called PMMs [151]. Minimal Kitaev chains have received a lot of attention very recently, due to important theoretical (see Ref. [152] and papers I and II) and experimental [27–29, 88, 89] advances.

6 The Kitaev chain

The Kitaev chain [32] is a TB chain of spinless fermions with p-wave superconducting pairing. The Hamiltonian describing the system is given by

$$H_{\text{Kitaev}} = -\sum_{n=1}^{N} \mu c_n^\dagger c_n - \sum_{n=1}^{N-1} (t c_n^\dagger c_{n+1} + \text{H.c.}) + \sum_{n=1}^{N-1} (\Delta c_n c_{n+1} + \text{H.c.}), \quad (34)$$

where c_n annihilates an electron on cite n, $-\mu$ is the energy associated with occupying a site, t quantifies the hopping between neighbouring sites, and Δ is the superconducting pairing between neighbouring sites. We will, in the following, take t and Δ to be real. The system is shown in Figure 13(a), where the fermionic sites are denoted with the black dashed ellipses. Each fermionic mode can be decomposed in terms of two MBSs on the same site as $c_n = \frac{1}{2}(\gamma_{n,A} + i\gamma_{n,B})$ [MBSs are denoted with red dots in Figure 13(a)]. In terms of the MBSs, Eq. (34) becomes

$$\begin{aligned} H_{\text{Kitaev}} = &-\frac{1}{2}\sum_{n=1}^{N} \mu(1 + i\gamma_{n,A}\gamma_{n,B}) \\ &+ \frac{1}{2}\sum_{n=1}^{N-1} \left[i(\Delta + t)\gamma_{n,B}\gamma_{n+1,A} + i(\Delta - t)\gamma_{n,A}\gamma_{n+1,B} \right]. \end{aligned} \quad (35)$$

Depending on the values of the parameters μ, t, and Δ, two distinct cases can be identified. For $t = \Delta = 0$ and $\mu \neq 0$, Eq. (35) becomes

$$H_{\text{Kitaev}} = -\frac{1}{2}\sum_{n=1}^{N} \mu(1 + i\gamma_{n,A}\gamma_{n,B}) = -\sum_{n=1}^{N} \mu c_n^\dagger c_n, \quad (36)$$

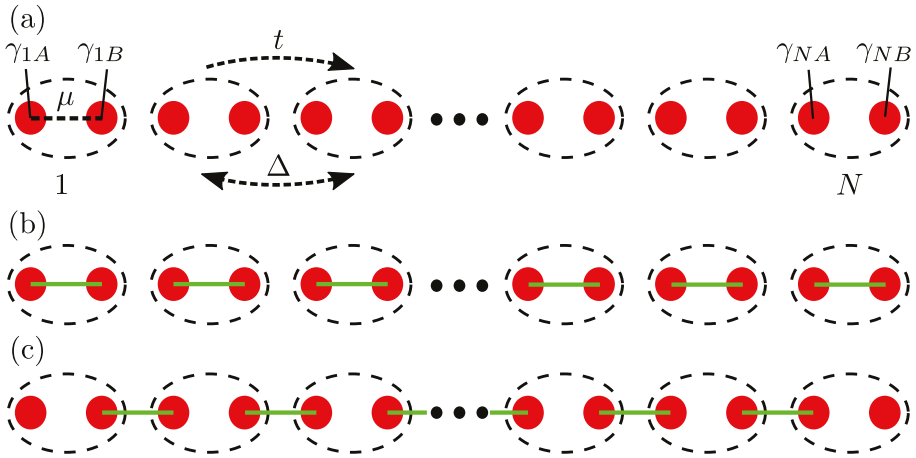

Figure 13: (a) The Kitaev chain. The black dashed ellipses denote fermionic sites and μ, t, and Δ quantify the onsite potential, nearest-neighbour hopping, and nearest-neighbour superconducting pairing respectively. The operators on fermionic site n can be decomposed in terms of MBSs $\gamma_{n,A}$ and $\gamma_{n,B}$ (red dots). (b) In the trivial case, only MBSs from the same fermionic site couple. (c) In the topological case, only MBSs from neighbouring sites couple.

and only MBSs within the same fermionic site are coupled. This case describes one fermionic mode localized on each site, see Figure 13(b).

For $\Delta = t \neq 0$ and $\mu = 0$, Eq. (35) reduces to

$$H_{\text{Kitaev}} = \sum_{n=1}^{N-1} it\gamma_{n,B}\gamma_{n+1,A} = t\sum_{n=1}^{N}\left(2d_n^\dagger d_n - 1\right), \tag{37}$$

where only MBSs on neighbouring sites are coupled [see Figure 13(c)] and $d_n = \frac{1}{2}(\gamma_{n,B} + i\gamma_{n+1,A})$ are fermionic modes composed of the coupled MBSs. Since MBSs $\gamma_{1,A}$ and $\gamma_{N,B}$ do not appear in Eq. (37), they commute with the Hamiltonian, and they can be used to define a delocalized fermionic mode

$$f = \frac{1}{2}(\gamma_{1,A} + i\gamma_{N,B}), \tag{38}$$

that also commutes with the Hamiltonian. With this choice of parameters, the ground state of H_{Kitaev} is two-fold degenerate, since the state $|0\rangle$ characterised by the absence of fermionic modes ($d_n|0\rangle = 0$) and the state $|1\rangle = f^\dagger|0\rangle$ have the same energy E_{GS}, as

$$H_{\text{Kitaev}}|1\rangle = H_{\text{Kitaev}}f^\dagger|0\rangle = f^\dagger H_{\text{Kitaev}}|0\rangle = f^\dagger E_{\text{GS}}|0\rangle = E_{\text{GS}}|1\rangle. \tag{39}$$

These states have even and odd fermion number parities respectively, as $f^\dagger f|0\rangle = 0$ and $f^\dagger f|1\rangle = |1\rangle$. Note also that one gets the one state from the other acting

with the MBS operators $\gamma_{1,A}$ and $\gamma_{N,B}$, e.g., $\gamma_{1,A}|0\rangle = |1\rangle$. In addition, there is always a finite gap $2t$ to the lowest excited state. Since f is delocalized between sites 1 and N, operators acting only on site 1 or N cannot read out the parity of the ground state. Quantum information stored in the parity of the ground state is thus protected against local perturbations, as long as the energy gap to the excited states remains finite. This robustness is one of the cornerstones of topologically-protected quantum computation with MBSs [38–41]. This case is clearly very different from the previously discussed one. We refer to the phase of the system depicted in Figure 13(b) ($\Delta = t = 0$, $\mu \neq 0$) as trivial and to the one depicted in Figure 13(c) ($\Delta = t \neq 0$, $\mu = 0$) as topologically nontrivial or topological.

Away from the fine-tuned situation $\Delta = t \neq 0$, $\mu = 0$, the lowest energy fermionic mode f can only be decomposed in terms of linear combinations of $\gamma_{n,A(B)}$ including also MBSs from the interior of the chain and the ground state degeneracy is lifted [41]. However, as long as $\mu < |2t|$, the ground state energy splitting decreases exponentially as the system size increases and vanishes in the limit $N \to \infty$ [153–155]. This scaling of the ground state splitting is a characteristic of the topological phase and in the following we will see how the phases $\mu < |2t|$ and $\mu > |2t|$ are topologically distinct.

Gapped Hamiltonians that can be continuously transformed to each other without a gap closing are topologically equivalent [156–161]. The passing from a trivial to a topological regime is signified by a bulk gap closing and re-opening. In order to study the bulk properties of the Kitaev chain, we enforce periodic boundary conditions by including the terms $-tc_N^\dagger c_1 + \Delta c_N c_1 + \text{H.c.}$ in Eq. (34) and perform the Fourier transformation $c_n = (1/\sqrt{N})\sum_k e^{ikna} c_k$. Next, we write the Fourier-transformed Hamiltonian in Bogoliubov-de Gennes (BdG) form. This involves doubling the degrees of freedom of the system by viewing the electron annihilation operators as creation operators for holes. In practice, this is achieved by making substitutions of the form

$$c_k^\dagger c_k = \frac{1}{2}(1 + c_k^\dagger c_k - c_k c_k^\dagger), \tag{40}$$

see Refs. [162, 163] for details. In BdG form, the Fourier-transformed Hamiltonian reads (up to a constant term) [41]

$$H_{\text{Kitaev}}^{\text{BdG}}(k) = \frac{1}{2}\sum_k \begin{pmatrix} c_k^\dagger, & c_{-k} \end{pmatrix} \begin{pmatrix} -\mu - 2t\cos(ka) & 2i\Delta\sin(ka) \\ 2i\Delta\sin(ka) & \mu + 2t\cos(ka) \end{pmatrix} \begin{pmatrix} c_k \\ c_{-k}^\dagger \end{pmatrix}, \tag{41}$$

where $k = 2\pi m/N$ with $m \in \mathbb{N}$, and a is the distance between neighbouring sites. The energy dispersion is

$$E_{\text{Kitaev}}^{\text{BdG}}(k) = \pm\sqrt{[\mu + 2t\cos(ka)]^2 + 4\Delta^2\sin^2(ka)}. \tag{42}$$

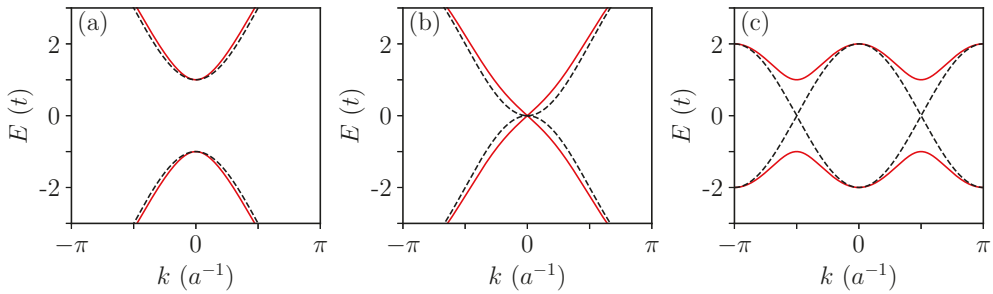

Figure 14: QP ($\Delta = t/2$, red lines) and bare electron ($\Delta = 0$, black dashed lines) energy dispersion as a function of the momentum k for the bulk Kitaev chain. (a) Trivial regime ($\mu = -3t$). (b) Topological transition ($\mu = -2t$). (c) Topological regime ($\mu = 0$).

Figure 14(a) shows the energy dispersion $E^{\mathrm{BdG}}_{\mathrm{Kitaev}}(k)$ as a function of k for $\mu = -3t$, $\Delta = t/2$ (QPs, red lines), and $\Delta = 0$ (bare electrons, black dashed lines). We see that the energy spectrum is gapped both in the superconducting and in the non-superconducting case. For $\mu = -2t$ the gap closes at $k = 0$ [Figure 14(b)]. For $2t > \mu > -2t$ the QP dispersion becomes gapped, while the bare electron dispersion remains gapless, as can be seen in Figure 14(c) where they are plotted for $\mu = 0$. The point $\mu = -2t$ is associated with a transition between topologically distinct phases. Similar considerations apply to the transition point at $\mu = 2t$.

7 The Majorana nanowire

Finding materials with the properties of the Kitaev chain is not an easy task. Electrons are spinful and the existence of p-wave superconductivity in materials is an issue of active research [164]. An alternative route is to artificially engineer a system that exhibits properties similar to the ones of the Kitaev chain, using more conventional ingredients. One of the early and subsequently intensely studied proposals is the MNW, a semiconductor NW with Rashba SO coupling [165–167] proximitized by an s-wave superconductor in a magnetic field [30, 31]. We note that the origin of Rashba SO coupling is different from the origin of the SO coupling presented in Section 1. The Rashba SO coupling originates from the structural asymmetry of the combined NW-substrate system, which gives rise to a finite electric field $\mathbf{E}$ inside the NW [168]. These effects are taken into account by including a Rashba term in the Hamiltonian:

$$H^{\mathrm{R}}_{\mathrm{SO}} = \frac{\alpha_{\mathrm{SO}}}{\hbar}(\mathbf{e} \times \mathbf{p}) \cdot \boldsymbol{\sigma}, \tag{43}$$

where $\mathbf{e}$ is the unit vector along the direction of $\mathbf{E}$, $\mathbf{p}$ is the momentum operator, $\boldsymbol{\sigma}$ is the Pauli vector and $\alpha_{\rm SO}$ quantifies the Rashba SO strength. We refer to the vector $\alpha_{\rm SO}(\mathbf{e}\times\mathbf{p})/\hbar$ as the Rashba SO field.

The Hamiltonian for the MNW is $H_{\rm MNW} = H_{\rm NW} + H_\Delta$. The bare NW Hamiltonian is

$$H_{\rm NW} = \int dx \Psi^\dagger(x) \left(\frac{p_x^2}{2m} - \mu + \frac{\alpha_{\rm SO}}{\hbar}\sigma_y p_x + \frac{E_{\rm Z}}{2}\sigma_z \right) \Psi(x), \tag{44}$$

where $\Psi(x) = [\Psi_\uparrow(x),\, \Psi_\downarrow(x)]^T$ is the field operator in real space, m is the effective electron mass (we drop the * superscript here), μ the chemical potential of the NW, and $E_{\rm Z}$ is the Zeeman energy resulting from a magnetic field along $\hat{z}$ perpendicular to the SO field $(\alpha_{\rm SO}p_x/\hbar)\hat{y}$. The induced superconductivity is modelled by

$$H_\Delta = \int dx \left[\Psi^T(x) \frac{1}{2} \Delta i\sigma_y \Psi(x) + \text{H.c.} \right], \tag{45}$$

where Δ is the induced superconducting pairing.

We first study the energy dispersion of $H_{\rm NW}$ for an infinitely long NW. Fourier transforming Eq. (44) using $\Psi(x) = (1/2\pi)\int dk e^{ikx}\Psi(k)$ we obtain [41]

$$H_{\rm NW}(k) = \int dk \Psi^\dagger(k) \left(\frac{\hbar^2 k^2}{2m} - \mu + \alpha_{\rm SO} k\sigma_y + \frac{E_{\rm Z}}{2}\sigma_z \right) \Psi(k), \tag{46}$$

where $\Psi(k) = [\Psi_\uparrow(k),\, \Psi_\downarrow(k)]^T$. The energy dispersion is

$$E_{\rm NW}(k) = \varepsilon_k \pm r_k, \quad \varepsilon_k = \frac{\hbar^2 k^2}{2m} - \mu, \quad r_k = \sqrt{\frac{E_{\rm Z}^2}{4} + \alpha_{\rm SO}^2 k^2}. \tag{47}$$

Figure 15(a) shows $E_{\rm NW}(k)$ as a function of k for $E_{\rm Z} \neq 0$ and $\alpha_{\rm SO} = 0$. The finite Zeeman energy splits the spin-degenerate parabolic band into two bands with spins polarized parallel and anti-parallel to the z-axis at every value of k. Note that states with opposite momenta have the same spin polarization. The s-wave superconducting pairing in Eq. (45) on the other hand, only couples electrons of opposite momenta and spins. Thus, even if H_Δ is included, the particle-hole gap remains closed in this case. The dispersion for $E_{\rm Z} = 0$ and $\alpha_{\rm SO} \neq 0$ is shown in Figure 15(b). The spin-degenerate bands split at finite momenta but remain degenerate at $k = 0$. Electrons with the same energy have opposite spin polarizations (parallel and anti-parallel to the y-axis) and opposite momenta in this case. If H_Δ is included a particle-hole gap opens. But since time-reversal symmetry is not broken this gapped phase is topologically trivial. The dispersion for $E_{\rm Z} \neq 0$ and $\alpha_{\rm SO} \neq 0$ is shown in Figure 15(c). The finite

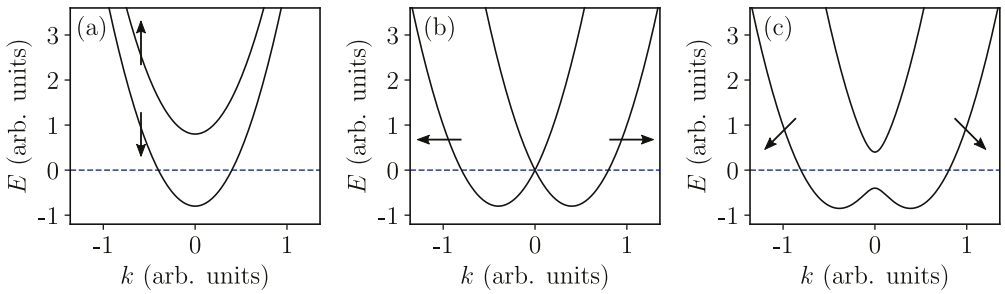

Figure 15: Dispersion relation of the bare NW for (a) $E_{\rm Z} \neq 0$, $\alpha_{\rm SO} = 0$, (b) $E_{\rm Z} = 0$, $\alpha_{\rm SO} \neq 0$, and (c) $E_{\rm Z} \neq 0$, $\alpha_{\rm SO} \neq 0$. The chemical potential is set to zero (dashed blue lines).

magnetic field opens a gap at $k = 0$ and Kramers degeneracy is lifted. Electron spins at the same energy and opposite momenta align along different directions. The pairing H_Δ can induce a particle-hole gap in this case and time-reversal symmetry is broken. Thus, $H_{\rm MNW}$ can in principle have a topological phase.

In order to study the topological properties of $H_{\rm MNW}$, we Fourier transform it and write it in BdG form [41]:

$$H^{\rm BdG}_{\rm MNW}(k) = \frac{1}{2}\int dk \mathbf{\Psi}^\dagger(k) \begin{pmatrix} h(k) & -\Delta i\sigma_y \\ \Delta i\sigma_y & -h(-k)^* \end{pmatrix} \mathbf{\Psi}(k) \tag{48}$$

where $\mathbf{\Psi}(k) = \left[\Psi_\uparrow(k),\, \Psi_\downarrow(k),\, \Psi^\dagger_\uparrow(-k)\, \Psi^\dagger_\downarrow(-k)\right]^T$ and $h(k) = \varepsilon_k + \alpha_{\rm SO} k\sigma_y + \frac{E_{\rm Z}}{2}\sigma_z$. The energy dispersion is

$$E^{\rm BdG}_{\rm MNW}(k) = \pm\sqrt{\varepsilon_k^2 + r_k^2 + \Delta^2 \pm 2\sqrt{\varepsilon_k^2 r_k^2 + \Delta^2 \frac{E_{\rm Z}^2}{4}}}. \tag{49}$$

The lowest energy branches $(+-)$ and $(-+)$ of the dispersion relation are plotted in Figure 16 as functions of k for $\Delta \neq 0$ (red solid lines, QPs) and $\Delta = 0$ (black dashed lines, bare dispersion). In Figure 16(a) $E_{\rm Z} < 2\sqrt{\mu^2 + \Delta^2}$ and the QP spectrum is gapped. The gap closes for $E_{\rm Z} = 2\sqrt{\mu^2 + \Delta^2}$ [Figure 16(b)] and reopens for $E_{\rm Z} > 2\sqrt{\mu^2 + \Delta^2}$ [Figure 16(c)]. Similarly to the Kitaev chain, this gap closing and reopening signifies a topological phase transition. One can in fact show that, for $E_{\rm Z} < 2\sqrt{\mu^2 + \Delta^2}$ and $E_{\rm Z} > 2\sqrt{\mu^2 + \Delta^2}$, $H^{\rm BdG}_{\rm MNW}(k)$ can be deformed into $H^{\rm BdG}_{\rm Kitaev}(k)$ in the trivial and the topological regime respectively, without closing the gap [41, 114]. Thus, in the regime $E_{\rm Z} > 2\sqrt{\mu^2 + \Delta^2}$ the MNW is topologically equivalent to the Kitaev chain in the topological regime and MBSs are expected to appear at the two ends of the MNW.

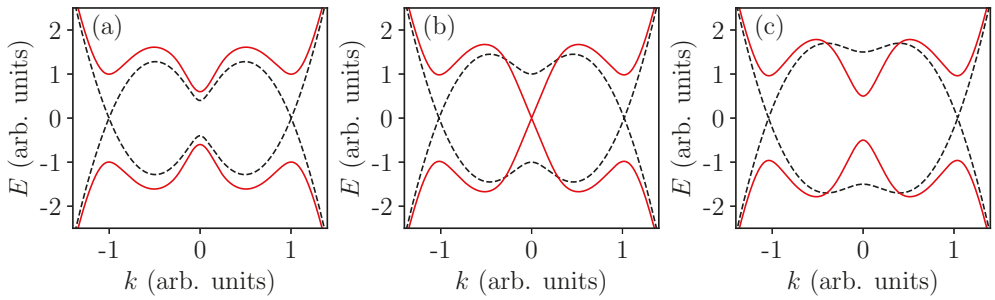

Figure 16: QP ($\Delta \neq 0$, red lines) and bare electron ($\Delta = 0$, black dashed lines) energy dispersion as a function of the momentum k for the MNW. (a) Trivial regime ($E_Z < 2\sqrt{\mu^2 + \Delta^2}$). (b) Topological transition ($E_Z = 2\sqrt{\mu^2 + \Delta^2}$). (c) Topological regime ($E_Z > 2\sqrt{\mu^2 + \Delta^2}$).

8 Conductance signatures and quality assessment of MBSs

As in the Kitaev chain, the appearance of unpaired MBSs at the two ends of a MNW in the topological regime implies a degeneracy between ground states with different parity corresponding to the zero-energy fermionic mode composed of the unpaired MBSs being occupied or unoccupied. This feature can be probed with a transport setup like the one in Figure 17(a), where a MNW in the topological regime is tunnel-coupled to a normal lead L and the zero-energy fermionic mode is composed of γ_1 and γ_2. If the chemical potentials in L and in the MNW are aligned, electrons in L do not require extra energy to occupy the fermionic mode in the MNW. This translates to a zero-bias peak in the local differential conductance $G_{LL} = dI_L/dV_L$. The zero-bias peak is, in fact, predicted to be quantized to the conductance quantum $G_0 = 2e^2/h$ [123–132]. Early transport experiments in similar setups indeed exhibited zero-bias peaks [115, 117], but it gradually became clear that topologically trivial ABSs emerging due to disorder in long MNWs can mimic the conductance characteristics of MBSs [83, 128, 169–178]. Since the normal lead is only coupled to one end of the MNW, it is impossible to distinguish between tunneling into a delocalized fermionic mode composed of γ_1 and γ_2 [see Figure 17(a)] and tunneling into a trivial ABS at zero energy localized at the coupled end. Therefore, a zero-bias peak in the local differential conductance of a MNW is a necessary but not a sufficient condition for the MNW to be in the topological regime.

Significantly more convincing evidence can be obtained with nonlocal conductance measurements [88, 121, 133–138] in a setup similar to the one sketched in Figure 17(b). Normal leads, L and R, are coupled to opposite MNW ends which allows measurement of the nonlocal conductances $G_{LR} = dI_L/dV_R$ and

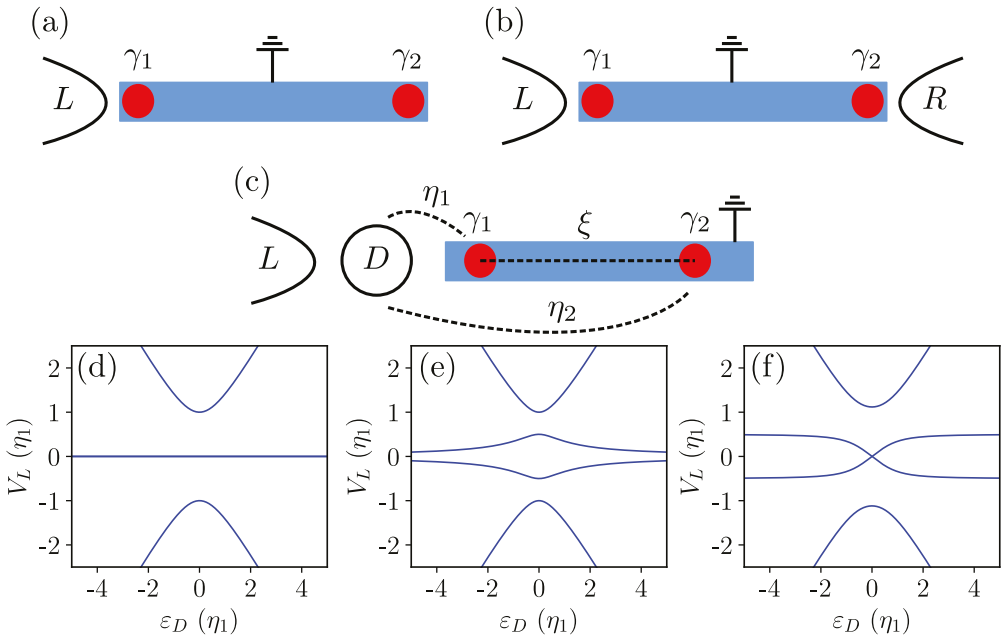

Figure 17: (a) Transport setup for measuring local conductance of a MNW with MBSs γ_1 and γ_2 with a normal metal lead L. (b) With an additional normal lead R coupled to the other end of the MNW, nonlocal transport spectroscopy can be performed. (c) Coupling the MNW to a QD D, information on MBS localization and on the topological properties of the MNW can be obtained with local spectroscopy alone. (d, e, f) Expected positions of local conductance peaks for the combined QD-MNW system shown in (c) as functions of the energy ε_D of the level of QD D for (d) $\xi = 0$, $\eta_2 = 0$ (no splitting of the zero-bias peak), (e) $\xi = 0$, $\eta_2 = \eta_1/2$ (diamond pattern), and (f) $\xi = \eta_1/2$, $\eta_2 = 0$ (bowtie pattern).

$G_{RL} = dI_R/dV_L$. While a local conductance peak provides evidence of a fermionic state with local support, nonlocal conductance is only finite for states with finite support along the length of the MNW [134]. Since such states can only be found in the continuum above the induced gap in the MNW, nonlocal conductance can monitor the closing and re-opening of the particle-hole gap. Nonlocal conductance steers the attention to the detection of the passing to the topological regime rather than the detection of MBSs. A protocol to determine whether a MNW is in the topological regime was proposed in Ref. [138]. According to the protocol, the existence of simultaneous zero-bias peaks in G_{LL} and G_{RR} in parameter regimes beyond the topological phase transition as monitored by G_{LR} and G_{RL} would imply the emergence of unpaired MBSs at the ends of the MNW with a very high probability. In Ref. [121] it was reported that several devices passed the protocol.

Coupling a MNW to a QD, local conductance can provide information on the degree of localization of MBSs and on their topological nature by probing the spectrum of the combined QD-MNW system [118, 139–141]. The setup is sketched

in Figure 17(c). QD D is coupled to the left end of a MNW and to the normal lead L. The splitting of the ground state degeneracy of the bare MNW, ξ, quantifies the overlap of the MBSs γ_1 and γ_2 ($\xi = 0$ for an infinitely long MNW with γ_1 and γ_2 localized at the left and right end respectively). The coupling of the QD to MBS γ_1 is η_1, while η_2 accounts for a possible coupling to MBS γ_2. For topological MBSs $|\eta_2/\eta_1| = 0$ and the QD couples only to γ_1. If a finite component of γ_2 also exists at the left end of the MNW one has $|\eta_2/\eta_1| > 0$. For $|\eta_2/\eta_1| \simeq 1$, the QD couples equally to γ_1 and γ_2 which corresponds to having a local trivial ABS at the left end of the MNW. The local conductance peaks of the combined QD-MNW system appear at the voltages [140]

$$V_L = \pm\frac{1}{2}\sqrt{(\xi - \varepsilon_D)^2 + (\eta_1 + \eta_2)^2} \pm \frac{1}{2}\sqrt{(\xi + \varepsilon_D)^2 + (\eta_1 - \eta_2)^2}, \qquad (50)$$

where ε_D is the energy of the single QD level which is considered to be spin-polarized. Figure 17(d) shows the expected positions of the conductance peaks as functions of ε_D and for $\xi = 0$, $\eta_2 = 0$. In the case of perfectly localized MBSs and when the QD only couples to γ_1, a zero-bias conductance peak is observed for any value of ε_D, as coupling to only one of the MBSs cannot lift the ground state degeneracy of the QD-MNW system. Figure 17(e) shows the corresponding plot for $\xi = 0$, $\eta_2 = \eta_1/2$. Coupling to both MBSs leads to a splitting of the zero-bias peak which still vanishes for large $|\varepsilon_D|$ but obtains its maximum value at the resonance ($\varepsilon_D = 0$), giving rise to a characteristic "diamond" shape. Finally, for $\xi = \eta_1/2$, $\eta_2 = 0$, the zero-bias conductance peak splits away from the resonance and the MBS overlap gives rise to a characteristic "bowtie" pattern [Figure 17(f)]. Paper II showed that a similar setup can be used to assess the quality of PMMs.

9 Nonabelian operations

The successful execution of a braiding experiment would provide the most compelling evidence of the realization of spatially separated MBSs. A few proposals on how braiding might be realized can be found in Refs. [37, 142–150, 179–185]. All braiding schemes are based on the fact that isolated MBSs are nonabelian anyons [38–40]. Generalising the results of Section 6, a system with $2N$ unpaired MBSs will have 2^N degenerate ground states. If a finite gap to the excited states exists, operations adiabatic with respect to the gap can drive the system from one ground state to another. Ground state changes within the degenerate subspace can be achieved, for example, with exchanges of the MBS positions. Such operations constitute the basis of topological quantum computation [38–41].

In this section, we first show that position exchanges of MBSs have nontrivial effects on their state and how these effects can be harnessed to create a qubit and perform quantum computation. Next we focus on how such exchanges can be achieved in a setup with three MNWs [142–150]. We note that in this section we follow closely the reviews [35, 41].

9.1 Braiding MBSs

Exchanging the positions of two MBSs, γ_1 and γ_2, can be described with the action of the unitary braid operator B_{12}:

$$B_{12}\gamma_1 B_{12}^\dagger = \chi_2\gamma_2, \quad B_{12}\gamma_2 B_{12}^\dagger = \chi_1\gamma_1, \tag{51}$$

where χ_1, χ_2 are factors to be determined. From $B_{12}B_{12}^\dagger = 1$ and $\gamma_n^2 = 1$ it follows that $(B_{12}\gamma_n B_{12}^\dagger)^2 = 1$. From Eqs. (51) we additionally have $(B_{12}\gamma_1 B_{12}^\dagger)^2 = \chi_2^2$ and $(B_{12}\gamma_2 B_{12}^\dagger)^2 = \chi_1^2$, which implies that $\chi_1 = \pm 1$, $\chi_2 = \pm 1$. The action of the braid operator on the number operator $f_{12}^\dagger f_{12} = \frac{1}{2}(1 + i\gamma_1\gamma_2)$ [with $f_{12} = \frac{1}{2}(\gamma_1 + i\gamma_2)$] is

$$B_{12}f_{12}^\dagger f_{12}B_{12}^\dagger = \frac{1}{2}(1 - i\chi_1\chi_2\gamma_1\gamma_2). \tag{52}$$

Fermion number parity conservation enforces $B_{12}f_{12}^\dagger f_{12}B_{12}^\dagger = f_{12}^\dagger f_{12}$ which leads to $\chi_1\chi_2 = -1$. Whether $\chi_1 = 1$, $\chi_2 = -1$ or $\chi_1 = -1$, $\chi_2 = 1$ depends on the Hamiltonian that drives the unitary evolution for the exchange [41, 142]. For $\chi_1 = 1$, $\chi_2 = -1$, the effect of exchanging the two MBSs is

$$\gamma_1 \to -\gamma_2, \quad \gamma_2 \to \gamma_1. \tag{53}$$

The specific choice of $\chi_1 = 1$, $\chi_2 = -1$ allows us to write the braid operator that exchanges the MBSs γ_1 and γ_2 as

$$B_{12} = \frac{1}{\sqrt{2}}(1 + \gamma_1\gamma_2). \tag{54}$$

The effect of the braid operator on the number states of the fermion f_{12} ($f_{12}\left|0_{12}\right\rangle = 0$, $f_{12}\left|1_{12}\right\rangle = \left|0_{12}\right\rangle$) amounts only to multiplication with a phase factor:

$$B_{12}\left|0_{12}\right\rangle = \frac{1}{\sqrt{2}}(1+i)\left|0_{12}\right\rangle, \quad B_{12}\left|1_{12}\right\rangle = \frac{1}{\sqrt{2}}(1-i)\left|1_{12}\right\rangle. \tag{55}$$

Acting with the braid operators on the MBSs two times brings the MBSs to their original positions, but both operators acquire a minus sign:

$$\gamma_1 \to -\gamma_1, \quad \gamma_2 \to -\gamma_2. \tag{56}$$

An experiment aiming at exhibiting the nonabelian nature of MBSs, would begin with initializing the system of γ_1 and γ_2 at a given parity state $|0_{12}\rangle$ or $|1_{12}\rangle$. After performing the exchange, the parity of the MBSs pair is read out. A prerequisite for this to happen is to fuse the MBSs into the fermion f_{12} by bringing them close to each other or by coupling them. According to our analysis above and depending on the initial state, the outcome of the measurement after the fusion can either be even parity (corresponding to the vacuum $|0_{12}\rangle$) or odd parity (corresponding to the fermion $|1_{12}\rangle$). Thus, fusing two MBSs one can get either the vacuum or a fermion. This is a consequence of the fusion rules for a broad group of anyons – whose most famous representatives are the MBSs – called Ising anyons [38–40].

Even though braiding and double-braiding MBSs has nontrivial effects on the MBS operators [see Eqs. (53) and (56)], these effects cannot be detected because exchanges of two MBSs do not alter the occupation of the fermionic state f_{12}. In the following section we describe how this is altered if two additional MBSs are considered.

9.2 MBS qubits

We consider a system of four MBSs γ_1, γ_2, γ_3, γ_4 and the basis $|n_{12}, n_{34}\rangle$, where $n_{12} = 0_{12}, 1_{12}$ and $n_{34} = 0_{34}, 1_{34}$, corresponding to the occupation numbers of the fermions $f_{12} = \frac{1}{2}(\gamma_1 + i\gamma_2)$ and $f_{34} = \frac{1}{2}(\gamma_3 + i\gamma_4)$. Suppose that the system is initialized in the even parity state $|0_{12}, 0_{34}\rangle$. Exchanging MBSs belonging to the same fermion ($\gamma_1 \leftrightarrow \gamma_2$ or $\gamma_3 \leftrightarrow \gamma_4$) has the trivial effect of multiplying the state with a phase factor. The exchange of MBSs belonging to different fermions has a nontrivial effect though:

$$B_{23}\,|0_{12}, 0_{34}\rangle = \frac{1}{\sqrt{2}}(|0_{12}, 0_{34}\rangle + i\,|1_{12}, 1_{34}\rangle), \tag{57}$$

where $B_{23} = (1+\gamma_2\gamma_3)/\sqrt{2}$. We see that starting from a state with zero fermion occupation, braiding MBSs we obtain a superposition of the fermionic states being empty or occupied. For a double braid the state changes as $B_{23}^2\,|0_{12}, 0_{34}\rangle \propto |1_{12}, 1_{34}\rangle$. This is a remarkable result. Exchanging the positions of two MBSs twice, the system does not return to its original state, as the fermion occupations which are measurable quantities have changed. MBS exchanges can only induce changes within the same parity subspace and starting from an odd parity state one would in an equivalent way get $B_{23}^2\,|0_{12}, 1_{34}\rangle \propto |1_{12}, 0_{34}\rangle$.

Four MBSs can be used to define a qubit. Focusing on the even parity subspace, and considering $|0_{12}, 0_{34}\rangle \equiv |\mathbf{0}\rangle$ and $|1_{12}, 1_{34}\rangle \equiv |\mathbf{1}\rangle$ to be the north and south

pole of the Bloch sphere respectively, an equivalence can be found between the action of the Pauli matrices on $|\mathbf{0}\rangle$, $|\mathbf{1}\rangle$ and the action of products of MBSs on $|0_{12}, 0_{34}\rangle$, $|1_{12}, 1_{34}\rangle$:

$$-i\gamma_1\gamma_2 = \sigma_z = -i\gamma_3\gamma_4, \quad -i\gamma_2\gamma_3 = \sigma_x, \quad -i\gamma_1\gamma_3 = \sigma_y = -i\gamma_2\gamma_4. \tag{58}$$

Qubit operations with MBSs are topologically protected as quantum information is encoded nonlocally in the MBSs and is thus robust against local perturbations. However, MBS qubits are susceptible to tunneling of QPs which can change the computational space from even to odd and vice versa. Such tunneling events are referred to as QP poisoning [186–188]. QP poisoning sets an upper limit to the duration of braiding operations. On the other hand, MBS exchanges have to be performed adiabatically with respect to the gap to the excited states. As long as the MBS exchanges are performed sufficiently slowly to be adiabatic and sufficiently fast to avoid QP poisoning, the results of braiding are not dependent on how the exchanges are performed.

A drawback of quantum computation with MBS qubits is that braid operations are not sufficient for universal quantum computation; braiding can only implement qubit rotations by $\pi/2$:

$$B_{12} = e^{-i\frac{\pi}{4}\sigma_z} = B_{34}, \quad B_{23} = e^{-i\frac{\pi}{4}\sigma_x}. \tag{59}$$

In order to perform universal quantum computation with MBSs, schemes including more involved operations have been suggested, see for example Refs. [38, 189, 190]. Alternatively, one could consider combining MBS qubits with other qubit architectures [191–195].

9.3 Braiding in trijunctions

Since we focus on MBSs in 1D systems, one might wonder how braiding can be possible, since it requires moving the MBSs around one another. The solution is to create networks of 1D MNWs, which effectively are 2D. The minimal setup to physically exchange two MBSs is the trijunction [142, 143, 150] shown in the panels of Figure 18. The trijunction consists of three connected MNWs A, B, and C which can fully or partially be in the topological regime hosting MBSs at the ends of the topological region. This can be achieved with locally varying parameters such as the chemical potentials in the MNWs. In step 1, none of the legs of the trijunction is in the topological regime, which is denoted with the light blue color. In step 2, MNW A becomes topological (darker blue) with two MBSs γ_1 (red) and γ_2 (green) at its ends. Adiabatically moving the edges of the topological region (step 3) the MBS pair can initially be moved to MNW B

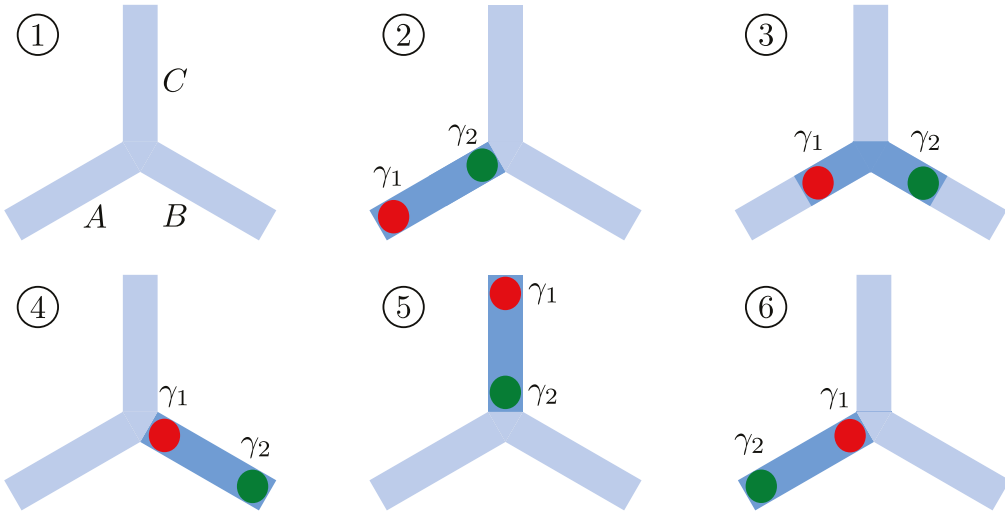

Figure 18: Protocol for physical exchange of the positions of two MBSs in a trijunction consisting of MNWs A, B, and C. The light (dark) blue color denotes the parts of the trijunction that are in the trivial (topological) regime. At the end of the protocol the positions of MBSs γ_1 (red) and γ_2 (green) are exchanged.

(step 4), where now it is γ_1 that is closest to the center of the trijunction. In step 5, the MBSs are transferred to MNW C and in a similar manner back to A in step 6, where now their positions are exchanged.

The protocol described in the previous paragraph can be very hard to implement in practice and alternative schemes have been considered to braid MBSs in trijunctions without physically moving them [144–149]. Such a scheme is outlined in the panels of Figure 19. Three MNWs A, B, C are placed in a trijunction arrangement but the couplings between them and between the MBSs at their ends can be turned on and off. The aim of the protocol is to exchange MBSs γ_1 (red) and γ_2 (green), while MBSs γ_3 (yellow) and γ_4 (magenta) remain unaffected during the protocol. The protocol begins with the MBSs in C fused (step 1), which is denoted by the gray dots, a finite coupling energy ξ_C (solid black line) and a lighter blue color of MNW C. In step 2, ξ_C is gradually decreased while the coupling between MNWs A and C, λ_A, is gradually increased (black dashed lines). In step 3, λ_A attains its maximum value and $\xi_C = 0$. The MBSs in A and C closest to the center of the trijunction are now fused, while the MBS in C away from the junction is decoupled. In Ref. [144] it was shown that this operation is equivalent to the transfer of MBS γ_1 to the end of MNW C away from the junction. In step 4, λ_A is gradually decreased while the coupling between MNWs B and C, λ_B, is gradually increased. In step 5, $\lambda_A = 0$, λ_B attains its maximum value, and γ_2 is transferred to the end of MNW A closest to the junction. Similar tunings of ξ_C and λ_B in steps 6 and 7 transfer γ_1 to

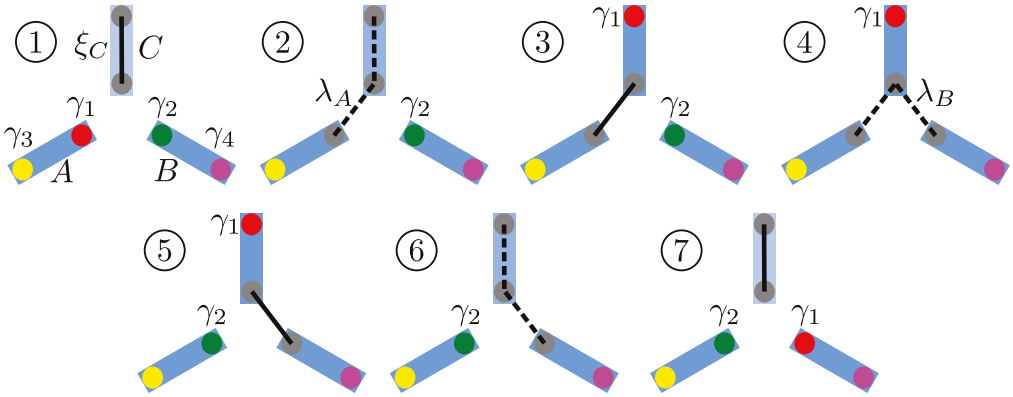

Figure 19: Protocol for braiding MBSs γ_1 (red) and γ_2 (green) with MNWs A, B, and C in a trijunction arrangement. Colorful MBSs are uncoupled while gray ones are fused. The couplings between the MNW C and the MNWs A and B (λ_A, λ_B) and the coupling between the MBSs in C (ξ_C) can be turned on and off. Solid black lines denote maximum couplings while dashed ones increasing/decreasing couplings.

MNW B. An adapted version of the protocol described above was one of the nonabelian operations considered in Paper II.

10 Minimal Kitaev chains and PMMs

As mentioned in Section 8, the disorder in long MNWs can lead to the emergence of trivial ABSs that mimic the conductance characteristics of the MBSs [83, 128, 169–178]. An alternative proposal to avoid complications due to disorder is to engineer an artificial Kitaev chain consisting of QDs coupled via s-wave superconducting segments [196]. It was shown in Ref. [151] that a system with only two QDs coupled via an s-wave superconductor can also host MBSs. In this section some of the main findings of Ref. [151] are summarized, as they constitute the basis for the work presented in Papers I and II. We also briefly discuss the connection between the theoretical model suggested in [151] and a similar model suggested quite recently [152].

The system considered in Ref. [151] is sketched in Figure 20(a). Two QDs, L and R, spin-polarized by the noncollinear magnetic fields $\mathbf{B}_L$ and $\mathbf{B}_R$, are coupled via a superconductor S. The geometry is similar to the one considered for CP splitters [22–29]. Figure 20(b) shows the corresponding energy level diagram, where two possible couplings between the QDs, χ and Ω, are also depicted. The coupling χ quantifies ECT from one QD to the other via states in the QP continuum of S, while Ω quantifies the strength of CAR, which involves breaking of CPs in S and subsequent tunneling of the constituent electrons into the QDs

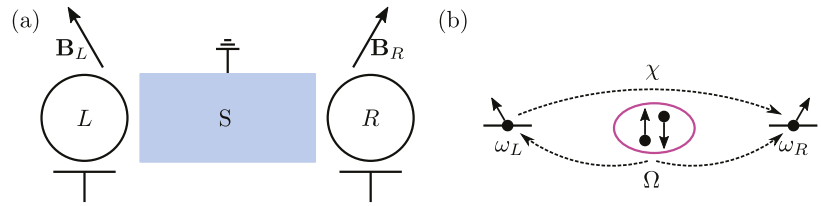

Figure 20: (a) Setup to realize PMMs. QDs L and R are coupled through a superconductor S and are subject to noncollinear magnetic fields $\mathbf{B}_L$ and $\mathbf{B}_R$. Adapted from Ref. [151]. (b) Energy level diagram where the processes of ECT and CAR are shown with strengths χ and Ω respectively. Adapted from paper II.

L and R. Such tunneling processes are studied in detail in Ref. [197]. Note that local AR is suppressed as the QDs are spin-polarized. The magnitudes of χ and Ω depend on the angle φ between $\mathbf{B}_L$ and $\mathbf{B}_R$ as

$$\chi = \chi_{\max} \cos(\varphi/2), \quad \Omega = \Omega_{\max} \sin(\varphi/2), \tag{60}$$

where $\chi_{\max}$, $\Omega_{\max}$ correspond to the maximum strength of ECT and CAR respectively. Since ECT is spin-preserving, χ is suppressed for $\varphi = \pi$. On the other hand, since the electrons of the CPs have opposite spins in S, Ω is suppressed for $\varphi = 0$. Varying the angle φ, the relative magnitudes of χ and Ω can be tuned, which is crucial for the formation of MBSs in this system. The Hamiltonian is

$$H^{\text{spinless}} = \omega_L d_L^\dagger d_L + \omega_R d_R^\dagger d_R + (\chi d_L^\dagger d_R + \Omega d_L^\dagger d_R^\dagger + \text{H.c.}), \tag{61}$$

where d_L (d_R) annihilates an electron in QD L (R) and ω_L, ω_R are the on-site energies. The Hamiltonian H^{spinless} is a minimal version of H_{Kitaev} [cf. Eq. (34)] with only two fermionic sites, with the difference that H^{spinless} allows for different on-site energies ω_L, ω_R. Tuning the on-site energies to $\omega_L = \omega_R = 0$ and the angle φ so that $\chi = \Omega$ or $\chi = -\Omega$, unpaired MBSs appear in the QDs L and R and the system has two degenerate ground states with even and odd fermion number parity (see the analysis in Section 6). In order to study deviations from this fine-tuned situation, we write H^{spinless} in the many-body basis $\{|00\rangle, |11\rangle, |10\rangle, |01\rangle\}$, where $|n_L n_R\rangle$ are number states and $|11\rangle = d_L^\dagger d_R^\dagger |00\rangle$:

$$H^{\text{spinless}} = \begin{pmatrix} 0 & \Omega & 0 & 0 \\ \Omega & \omega_L + \omega_R & 0 & 0 \\ 0 & 0 & \omega_L & \chi \\ 0 & 0 & \chi & \omega_R \end{pmatrix}. \tag{62}$$

The lowest-energy eigenvalues in the even and the odd sector are

$$E^e = \frac{\omega_+}{2} - \frac{1}{2}\sqrt{(\omega_+)^2 + 4\Omega^2}, \quad E^o = \frac{\omega_+}{2} - \frac{1}{2}\sqrt{(\omega_-)^2 + 4\chi^2}, \tag{63}$$

where $\omega_+ = \omega_L + \omega_R$ and $\omega_- = \omega_L - \omega_R$. For $\omega_L = \omega_R = 0$ and $|\Omega| = |\chi|$, $E^o - E^e = 0$. Note that the degeneracy is not lifted for $\omega_L = 0$, $\omega_R \neq 0$ or $\omega_L \neq 0$, $\omega_R = 0$. For $\omega_L = \omega_R = 0$ and $|\Omega| \neq |\chi|$, $E^o - E^e = -|\chi| + |\Omega|$, while for $\omega_L \neq \omega_R \neq 0$ and $|\Omega| = |\chi|$, expanding up to second order in $\omega_{L,R}$, we find $E^o - E^e = \omega_L \omega_R / 2|\Omega|$. Thus, the ground state degeneracy splits to linear order in Ω and χ and to second order in $\omega_{L,R}$. This is in contrast to the exponentially small ground state energy splitting for a Kitaev chain in the topological regime (see Section 6). The MBSs presented in this section have the same properties as the MBSs discussed in the previous sections but they can only be found at fine-tuned sweet spots of the parameter space. They are not associated with a topological phase and they are not topologically protected. For this reason they were named PMMs.

Reference [152] proposed an alternative way to tune the relative amplitudes of ECT and CAR in a system with two QDs coupled via an ABS with energy $\varepsilon_{\mathrm{ABS}}$ in a NW with Rashba SO coupling proximitized by an s-wave superconductor. The model in Ref. [152] does not require a finite angle between the spin polarizations in the two QDs. Instead, it relies on the spin-flipping mechanism provided by the Rashba SO coupling under a global magnetic field. Without SO coupling only ECT processes would be possible, while the finite SO coupling allows for CAR processes as well. It was shown in Ref. [152] that the amplitudes of ECT and CAR depend differently on $\varepsilon_{\mathrm{ABS}}$. For $\varepsilon_{\mathrm{ABS}} = 0$, an interference effect causes the ECT amplitude to vanish, while the amplitude of CAR is maximal. For large $|\varepsilon_{\mathrm{ABS}}|$ it was found that the amplitude of ECT is finite while the amplitude of CAR is suppressed. One can thus navigate to a sweet spot with equal amplitudes of ECT and CAR (and thus PMMs) by controlling $\varepsilon_{\mathrm{ABS}}$.

Both models described above consider fully spin-polarized QDs. This is not the case in experiments aiming to realize minimal Kitaev chains [27–29, 88, 89], as a high magnetic field would destroy superconductivity. With a finite splitting to the higher spin states, the QD charging energies will also play a role. It is thus fair to wonder whether a sweet spot with PMMs can even be reached under realistic experimental conditions and, if so, how the properties of the PMMs will be affected. These issues, along with the effects of strong coupling between the QDs and the ABS, are the main focus of papers I and II.

2D topological insulators

Topological insulators are materials that exhibit an insulating bulk and metallic states at their boundaries. Conductance via the boundary states is dissipationless as they are protected by time-reversal symmetry which excludes backscattering. Among topological materials, topological insulators are classified in the symmetry class AII according to the Altland and Zirnbauer classification scheme [156], as they do not have particle-hole symmetry like the topological superconductors presented in the previous chapter. Apart from the theoretical interest in topological insulators, several applications that can harness the robustness of the boundary states have been suggested, see for example Ref. [198]. References [199, 200] provide excellent reviews on topological insulators, while Ref. [201] provides a self-contained introduction.

In this chapter, we focus on 2D topological insulators. For 2D topological insulators the boundary states are 1D edge states that come in Kramers-degenerate pairs. This is similar to having two copies of the quantum Hall effect [202, 203], which is why 2D topological insulators are also called quantum spin Hall insulators, the difference being that the quantum spin Hall effect requires no magnetic field. Moreover, the states are spin-momentum locked so the spin current is finite even though the charge current is zero.

11 CdTe/HgTe quantum wells

The quantum spin Hall effect was first observed in CdTe/HgTe QWs [10], where a HgTe layer is sandwiched between two CdTe layers. The discovery followed the prediction by Bernevig, Hughes, and Zhang who modelled the system deriving the BHZ Hamiltonian [9]. The QW is shown in Figure 21(a). In bulk, for both materials the same bands as for III-V semiconductors are formed close to the Γ

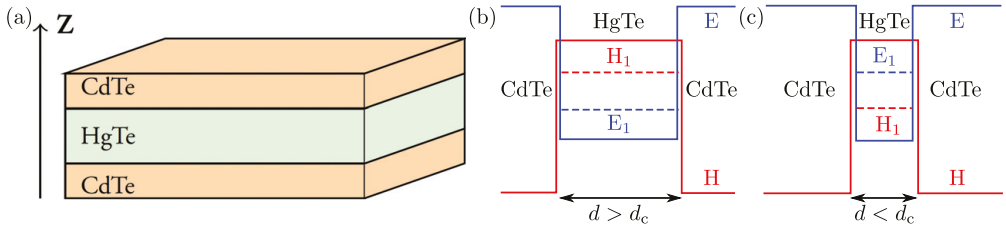

Figure 21: (a) Geometry of the CdTe/HgTe QW, Z is the growth direction. Adapted from Ref. [204]. (b, c) Band diagram for the QW at the Γ point for (b) the topological ($d > d_c$) and (c) the trivial ($d < d_c$) regime. Adapted from Ref. [9].

point, namely E, LH, and HH[4], see Section 1. In CdTe the E band lies above the LH and HH bands, but in HgTe the band structure is inverted and the LH and HH bands lie above E. The band diagram for the QW at the Γ point is depicted in Figure 21(b) (blue continuous line for the E band edge and red continuous line for the common LH and HH band edge, H). The inverted band structure in HgTe results in the formation of the subbands E_1 from a linear combination of the E and LH bands and H_1 from the HH band, shown with blue and red dashed lines in Figure 21(b). Thus, in the inverted regime H_1 lies above E_1. In a QW heterostructure confinement effects also play a role. If the thickness d of the HgTe layer is smaller than a critical value d_c the CdTe band ordering dominates and E_1 lies above H_1 [see Figure 21(c)]. At $d = d_c$ the gap closes, signifying a topological phase transition between the gapped regimes $d < d_c$ and $d > d_c$. The inverted regime with $d > d_c$ is topological while the $d < d_c$ regime is trivial.

The physics of the relevant subbands of the system is captured by the BHZ Hamiltonian [9] which reads

$$H_{\mathrm{BHZ}} = \begin{pmatrix} h(k) & 0 \\ 0 & h^*(-k) \end{pmatrix}, \tag{64}$$

where

$$h(k) = \begin{pmatrix} \epsilon(k) + M(k) & Ak_+ \\ Ak_- & \epsilon(k) - M(k) \end{pmatrix}, \tag{65}$$

and $\epsilon(k) = C - D(k_x^2 + k_y^2)$, $M(k) = M - B(k_x^2 + k_y^2)$, $k_\pm = k_x \pm i k_y$. H_{BHZ} is written in the basis $(|\mathrm{E}_1, +\rangle, |\mathrm{H}_1, +\rangle, |\mathrm{E}_1, -\rangle, |\mathrm{H}_1, -\rangle)^T$. Within the same subband, $|\mathrm{E}_1, \pm\rangle$ or $|\mathrm{H}_1, \pm\rangle$, $\pm$ denotes Kramers partners. The parameters A, B, C, D, M are adjusted for specific heterostructures. Importantly, M is the parameter that controls the transition from the trivial to the topological regime. The bands of the BHZ model in the k_x direction and for $k_y = 0$ are plotted schematically in Figures 22(a, b). In Figure 22(a) the system is in the trivial regime ($M > 0$)

[4]The split-off band lies far below in energy and we neglect it in the present discussion.

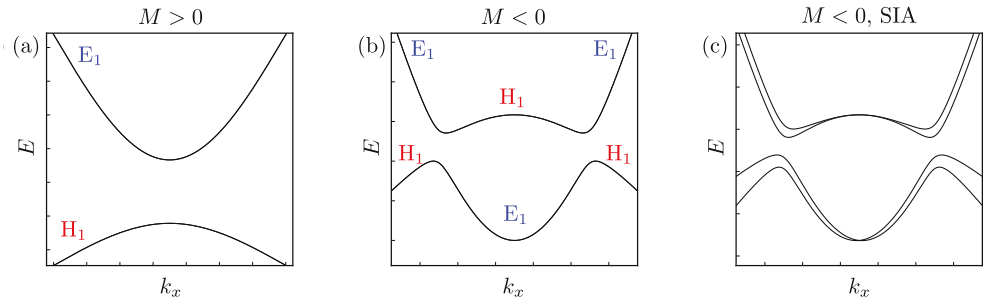

Figure 22: Band structure of the BHZ Hamiltonian along k_x and for $k_y = 0$. (a) For $M > 0$ the system is in the trivial regime and the subbands E_1, H_1 do not hybridize. (b) For $M < 0$ the system is in the topological regime and a hybridization gap is present. (c) SIA induces spin splitting between Kramers pairs for $|k_x| \neq 0$.

and the subbands E_1, H_1 do not hybridize. For $M = 0$ the gap closes and for $M < 0$ it re-opens and the system is in the topological regime, see Figure 22(b). Starting from large $|k_x|$, the lower band is H_1-like and the higher band is E_1-like. Moving towards smaller $|k_x|$ the bands hybridize and in the vicinity of $|k_x| = 0$ the situation is reversed as the higher band is H_1-like and the lower band is E_1-like.

One drawback of the CdTe/HgTe QW system is that the topological phase transition cannot be observed because the parameter controlling the transition is the thickness of the HgTe layer, which is fixed for each sample and cannot be changed continuously. Moreover, the fabrication and control of CdTe/HgTe QWs are quite demanding [11]. Shortly after the observation of the quantum spin Hall effect in CdTe/HgTe QWs the investigations for additional 2D topological insulator candidate platforms began.

12 InAs/GaSb quantum wells

The InAs/GaSb QW [11] consists of one GaSb layer and one InAs layer between two layers of AlSb that act as barriers, see Figure 23(a). The system is a type-II QW and the VB of GaSb is higher in energy than the CB of InAs. The band diagram is shown in Figure 23(b), with blue (red) continuous lines denoting the CB (VB) edges in the different layers. E_1 (H_1) here corresponds to the lowest-energy subband in the CB (VB) of InAs (GaSb) and is depicted with a blue (red) dashed line. For small material thicknesses, E_1 in InAs is higher in energy than H_1 in GaSb, and the system is in a trivial insulator regime exhibiting a confinement gap. For larger material thickness, E_1 lies lower than H_1, and the system is predicted to be a 2D topological insulator exhibiting a hybridization

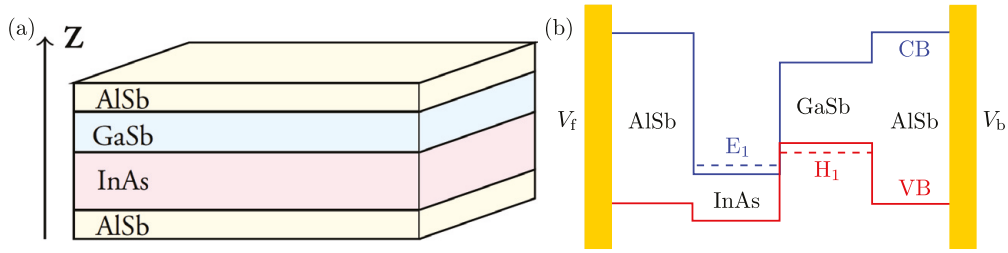

Figure 23: (a) Geometry of the InAs/GaSb QW with AlSb layers, Z is the growth direction. Adapted from paper VI. (b) Band diagram for the QW depicted in (a). E_1 (H_1) is the lowest-energy subband in the CB (VB) of InAs (GaSb) and is depicted with a blue (red) dashed line. Adapted from Ref. [11].

gap [11]. Note that the electrons are provided by the InAs layer while the holes by the GaSb one, which leads to relatively weak electron-hole hybridization and thus a small hybridization gap. Moreover, accumulation of electrons and holes in InAs and GaSb creates a built-in electric field. This asymmetry is taken into account by adding a structural inversion asymmetry (SIA) term to the BHZ Hamiltonian [11, 205]:

$$H_{\mathrm{SIA}} = \begin{pmatrix} 0 & 0 & -iR_0k_- & -S_0k_-^2 \\ 0 & 0 & S_0k_-^2 & iT_0k_-^3 \\ iR_0k_+ & S_0k_+^2 & 0 & 0 \\ -S_0k_+^2 & -iT_0k_+^3 & 0 & 0 \end{pmatrix}, \tag{66}$$

where the first order terms ($\propto k_\pm$) couple the Kramers pair $|\mathrm{E}_1, \pm\rangle$, the third order terms ($\propto k_\pm^3$) couple the Kramers pair $|\mathrm{H}_1, \pm\rangle$, the second order terms ($\propto k_\pm^2$) mix the E_1 and H_1 bands, and R_0, T_0, S_0 are the corresponding parameters quantifying the coupling strength. The effect of SIA on the BHZ band structure is shown in Figure 22(c). Turning on the SIA terms adiabatically the hybridization gap does not close and the system is still in the topological regime. SIA splits the Kramers pairs only for $|k_x| \neq 0$, while the degeneracy is not lifted at $k_x = 0$ since time-reversal symmetry is not broken.

An advantage of InAs/GaSb QWs comparing to CdTe/HgTe QWs is that tuning of the relative position of the bands E_1, H_1 in the heterostructure can be achieved with front and back gate voltages V_f and V_b [see Figure 23(b)]. One can thus drive the system continuously in and out of the topological regime. Experimental results confirm such a control over the topological phase [12].

Theoretical tools

13 Tight-binding discretization

The modelling of mesoscopic systems employs a variety of theoretical tools and computational techniques. TB discretization is a widely used method for calculating the eigenvalues and eigenvectors of a given closed system and for performing transport calculations. Its popularity stems from its intuitive formalism and from the fact that there exist readily available open-source numerical packages [206–208] that can be used to simulate a wide variety of systems. We have, in fact, already encountered a TB model in this thesis, the Kitaev chain [32] in Section 6.

The idea behind TB discretization is to represent real space with a grid of sites that electrons can occupy. A characteristic length scale is set by the distance between neighboring sites, the lattice constant d. We note here that d is usually much larger than inter-atomic distances in real materials and sites do not correspond to actual atoms, rather to areas in real space representing a number of atoms. TB discretization techniques that are described here are thus not to be confused with atomistic TB calculations that account for atomic orbitals. The discretized system is considered to be a good approximation of the continuous one if $d \ll \lambda_{\mathrm{dB}}$, where λ_{dB} is the de Broglie wavelength of the electrons in the system. For the calculations in papers III, IV and VI – which involve semiconductors – d was taken to be on the order of 1 nm.

13.1 General form

Any non-interacting TB Hamiltonian can be written in the form

$$H = \sum_{\mu,\nu} H_{\mu\nu} \left|\mu\right\rangle \left\langle\nu\right|, \tag{67}$$

where μ, ν are collective indices corresponding to sites in real space ($\mathbf{r}$) and any additional orbitals (a). The coupling between two sites $\mathbf{r}$ and $\mathbf{r}'$ is given by summing over the orbital degrees of freedom

$$H_{\mathbf{r}\mathbf{r}'} = \sum_{a,a'} H_{\mathbf{r}a,\mathbf{r}'a'} \left|\mathbf{r}a\right\rangle \left\langle \mathbf{r}'a'\right| . \tag{68}$$

The total Hamiltonian H can thus be written as a sum over all $H_{\mathbf{r}\mathbf{r}'}$. Typically, the Hamiltonian is written in matrix form and exact diagonalization is performed to find the corresponding eigenvalues and eigenvectors.

13.2 Alternative notations and second quantization form

In the literature the elements of Eq. (68) are often given in the mixed notation

$$H_{\mathbf{r}\mathbf{r}'} = H^{\mathrm{M}}_{\mathbf{r}\mathbf{r}'} \left|\mathbf{r}\right\rangle \left\langle \mathbf{r}'\right| \equiv \left|\mathbf{r}\right\rangle \left\langle \mathbf{r}'\right| \otimes H^{\mathrm{M}}_{\mathbf{r},\mathbf{r}'}, \tag{69}$$

where $H^{\mathrm{M}}_{\mathbf{r}\mathbf{r}'}$ is explicitly written in matrix form, characterizing the internal degrees of freedom. The elements of $H^{\mathrm{M}}_{\mathbf{r}\mathbf{r}'}$ are $H_{\mathbf{r}a,\mathbf{r}'a'}$ and their dimensions are $N_a \times N_a$, where N_a is the number of the internal degrees of freedom. $H^{\mathrm{M}}_{\mathbf{r}\mathbf{r}'}$ can, for example, be just a scalar for a system with no internal degrees of freedom or a 2×2 matrix for a system with spin 1/2. This notation is used in Section 13.4.

Moreover, it is quite natural to rewrite Eq. (68) within the framework of second quantization. The action of the operator $\left|\mathbf{r}a\right\rangle \left\langle \mathbf{r}'a'\right|$ on the basis states is defined by

$$\left|\mathbf{r}a\right\rangle \left\langle \mathbf{r}'a'\right| \left|\mathbf{r}''a''\right\rangle = \delta_{\mathbf{r}'\mathbf{r}''}\delta_{a'a''} \left|\mathbf{r}a\right\rangle . \tag{70}$$

These properties can be reproduced by the action of creation and annihilation operators on number states:

$$c^\dagger_{\mathbf{r}a} c_{\mathbf{r}'a'} \left|\mathbf{r}''a''\right\rangle = \delta_{\mathbf{r}'\mathbf{r}''}\delta_{a'a''} c^\dagger_{\mathbf{r}a} \left|0\right\rangle = \delta_{\mathbf{r}'\mathbf{r}''}\delta_{a'a''} \left|\mathbf{r}a\right\rangle , \tag{71}$$

where $c^\dagger_{\mathbf{r}a}$ creates an electron on site $\mathbf{r}$ in orbital a. Equation (68) can thus be written in a second-quantized form:

$$H_{\mathbf{r}\mathbf{r}'} = \sum_{a,a'} H_{\mathbf{r}a,\mathbf{r}'a'} c^\dagger_{\mathbf{r}a} c_{\mathbf{r}'a'} . \tag{72}$$

13.3 Discretization of continuous Hamiltonians

The first step towards discretizing a continuous Hamiltonian is to replace the positional basis states of the system and any scalar quantities [collectively gathered

in the function $V = V(x, y, z)$] appearing in the Hamiltonian with their discretized counterparts. For a square lattice this is achieved with the replacements

$$|x, y, z\rangle \to |x_n, y_n, z_n\rangle = |n_x d, n_y d, n_z d\rangle \equiv |n_x, n_y, n_z\rangle\,, \tag{73}$$

$$V(x, y, z) \to V(x_n, y_n, z_n) = V(n_x d, n_y d, n_z d), \equiv V(n_x, n_y, n_z), \tag{74}$$

where $n_x, n_y, n_z = 0, 1, 2, ...$ number the sites along the directions x, y, z.

Next, the Hamiltonian matrix elements $\langle n_x, n_y, n_z|\, H\, |n'_x, n'_y, n'_z\rangle$ have to be calculated in the new basis. This step involves expressing the spatial derivatives acting on the basis states with finite differences, see for example Ref. [209]. The partial derivatives with respect to x of a function $f(x, y, z)$ at (x_n, y_n, z_n) are expressed as

$$\partial_x f(x_n, y_n, z_n) \approx \frac{f(x_n + d) - f(x_n - d)}{2d}, \tag{75}$$

$$\partial_x^2 f(x_n, y_n, z_n) \approx \frac{f(x_n + d) + f(x_n - d) - 2f(x_n)}{d^2}, \tag{76}$$

$$\partial_x^3 f(x_n, y_n, z_n) \approx \frac{f(x_n + 2d) - 2f(x_n + d) + 2f(x_n - d) - f(x_n - 2d)}{2d^3}. \tag{77}$$

In the right-hand sides of the above equations, the arguments that remain constant have been suppressed, and expressions of the form $f(x_n + d)$ actually stand for $f(x_n + d, y_n, z_n)$. The partial derivatives with respect to y and z are given by expressions similar to Eqs. (75–77). The above expressions can be combined to obtain mixed derivatives. For instance, the mixed derivative ∂_{xy} is given by

$$\begin{aligned}\partial_{xy} f(x_n, y_n, z_n) = &\frac{f(x_n + d, y_n + d) + f(x_n - d, y_n - d)}{4d^2} \\ &- \frac{f(x_n + d, y_n - d) + f(x_n - d, y_n + d)}{4d^2}.\end{aligned} \tag{78}$$

Given the expressions (75–78) which provide the derivatives at a specific point, one can express the corresponding operators in the discretized positional basis. For example, from Eq. (75) it is straightforward to find the expression for ∂_x:

$$\partial_x \equiv \frac{1}{2d} \sum_{n_x, n_y, n_z} \Big[\, |n_x + 1, n_y, n_z\rangle \langle n_x, n_y, n_z| - |n_x - 1, n_y, n_z\rangle \langle n_x, n_y, n_z| \,\Big]. \tag{79}$$

13.4 Applications

Rashba nanowire in a magnetic field

In this section, the first-quantization form of H_{NW} given in Eq. (44) is discretized. A similar Hamiltonian is the starting point for one of the theoretical models employed in paper III. The Hamiltonian reads

$$H_{\mathrm{NW}} = -\frac{\hbar^2}{2m}\partial_x^2 - \mu - i\alpha_{\mathrm{SO}}\sigma_y\partial_x + \frac{E_{\mathrm{Z}}}{2}\sigma_z, \tag{80}$$

where $\hbar$ is the reduced Planck's constant, m, μ, and α_{SO} are the effective electron mass, chemical potential, and Rashba SO strength in the NW respectively, and $\sigma_{y,z}$ are Pauli matrices acting in spin space. The system is shown in Figure 24(a).

The NW is discretized in an 1D grid of N points, see Figure 24(b). The discretized positional states are $|n_x\rangle$ for $n_x = 0, ..., N-1$ and correspond to having one electron on site n_x. According to the previous section, the discretized version of Eq. (80) is

$$\begin{aligned} H_{\mathrm{NW}}^{\mathrm{TB}} = &\left[\sigma_0\,(2t-\mu) + \sigma_z\,\frac{E_{\mathrm{Z}}}{2}\right]\sum_{n_x=0}^{N-1}|n_x\rangle\langle n_x| \\ &- (\sigma_0 t + \sigma_y i t_{\mathrm{SO}})\sum_{n_x=0}^{N-2}\left(|n_x\rangle\langle n_x+1| + \mathrm{H.c.}\right), \end{aligned} \tag{81}$$

where $t = \hbar/(2md)$, $t_{\mathrm{SO}} = \alpha_{\mathrm{SO}}/(2d)$, and $\sigma_0 = \mathrm{diag}(1,1)$ is the 2×2 identity matrix, written explicitly here. The Hamiltonian matrix elements fall under two categories:

- Diagonal terms $\langle n_x|\, H_{\mathrm{NW}}^{\mathrm{TB}}\,|n_x\rangle = \sigma_0\,(2t-\mu) + \sigma_z\,\frac{E_{\mathrm{Z}}}{2}$, which describe the degrees of freedom of a specific site. These terms are referred to as onsite terms.
- Off-diagonal terms $\langle n_x|\, H_{\mathrm{NW}}^{\mathrm{TB}}\,|n_x+1\rangle = -(\sigma_0\, t + \sigma_y\, i t_{\mathrm{SO}})$ and their Hermitian conjugates, which describe the hopping from site n_x+1 to site n_x and from site n_x to site n_x+1 respectively. These terms are referred to as hopping terms.

Having calculated the matrix elements, one can write the Hamiltonian in matrix form. The resulting matrix has dimensions $2N \times 2N$ as the diagonal and off-diagonal terms described above are 2×2 matrices in spin space.

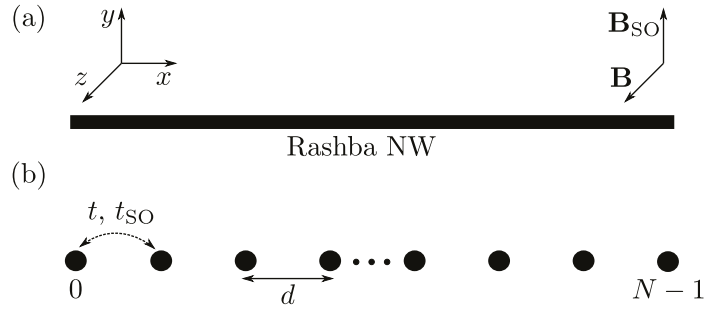

Figure 24: (a) Sketch of a Rashba NW subject to perpendicular magnetic and SO fields $\mathbf{B}$ and $\mathbf{B}_{\mathrm{SO}}$. (b) The discretized system consists of N sites and d is the lattice constant. The hopping amplitudes t and t_{SO} are also shown.

BHZ Hamiltonian

The BHZ Hamiltonian was introduced in Section 11 and is repeated here in a more compact form:

$$H_{\mathrm{BHZ}} = \sigma_0 \otimes s_0\, \epsilon(k) + \sigma_0 \otimes s_z\, M(k) + \sigma_z \otimes s_x\, A k_x - \sigma_0 \otimes s_y\, A k_y, \tag{82}$$

where $\epsilon(k) = C - D(k_x^2 + k_y^2)$, $M(k) = M - B(k_x^2 + k_y^2)$. The parameters A, B, C, D, and M are material-specific and the Pauli matrices σ_j, s_j act in the spin and band spaces respectively. The primary goal here is to obtain a discretized real space Hamiltonian in order to study systems finite in both the x and y directions. Letting one dimension be infinite, the Hamiltonian for a semi-infinite TB-regularized stripe can be obtained. Finally, letting the remaining finite dimension be infinite one arrives at a TB-regularized version of Eq. (82). Initially, the replacements $k_j \to -i\partial_j$ are needed to express H_{BHZ} in real space. Next, the procedure described in Section 13.3 is followed.

For a system finite in both the x and y directions, the total discretized Hamiltonian is a sum of the following terms:

- Onsite terms:

$$\sum_{n_x,n_y} \left[\sigma_0 \otimes s_0 \left(C - \frac{4D}{d^2}\right) + \sigma_0 \otimes s_z \left(M - \frac{4B}{d^2}\right)\right] |n_x, n_y\rangle \langle n_x, n_y| \,. \tag{83}$$

- Hopping x direction:

$$\sum_{n_x,n_y} \left[\sigma_0 \otimes s_0 \frac{D}{d^2} + \sigma_0 \otimes s_z \frac{B}{d^2} - i\sigma_z \otimes s_x \frac{A}{2D}\right] |n_x + 1, n_y\rangle \langle n_x, n_y| + \mathrm{H.c.} \tag{84}$$

- Hopping y direction:

$$\sum_{n_x,n_y}\left[\sigma_0\otimes s_0\,\frac{D}{d^2}+\sigma_0\otimes s_z\,\frac{B}{d^2}+i\sigma_0\otimes s_y\,\frac{A}{2D}\right]|n_x,n_y+1\rangle\langle n_x,n_y|+\text{H.c.}\quad(85)$$

Considering the system to be infinite along the x direction, k_x is a good quantum number, and the discretized positional states along x can be Fourier transformed as

$$|n_x\rangle=\frac{1}{\sqrt{N_x}}\sum_{k_x}e^{in_x dk_x}\,|k_x\rangle\,,\quad(86)$$

where N_x is the number of sites along the x direction and $|k_x\rangle$ are momentum eigenstates. Using the discrete δ function

$$\delta_{k_x,k_x'}=\frac{1}{N_x}\sum_{n_x}e^{in_x d(k_x-k_x')},\quad(87)$$

Eqs. (83–85) become:

- Onsite terms:

$$\sum_{k_x,n_y}\left\{\sigma_0\otimes s_0\left[C-\frac{4D}{d^2}+\frac{2D}{d^2}\cos(dk_x)\right]+\sigma_0\otimes s_z\left[M-\frac{4B}{d^2}+\frac{2B}{d^2}\cos(dk_x)\right]\right.$$
$$\left.+\sigma_z\otimes s_x\,\frac{A}{d}\sin(dk_x)\right\}|k_x,n_y\rangle\langle k_x,n_y|\,.\quad(88)$$

- Hopping y direction:

$$\sum_{k_x,n_y}\left[\sigma_0\otimes s_0\,\frac{D}{d^2}+\sigma_0\otimes s_z\,\frac{B}{d^2}+i\sigma_0\otimes s_y\,\frac{A}{2D}\right]|k_x,n_y+1\rangle\langle k_x,n_y|+\text{H.c.}\quad(89)$$

Considering the system to be infinite in the y direction as well and Fourier transforming, a TB regularization of Eq. (82) is obtained. Dropping the sums over k_x, k_y and the operators $|k_x,k_y\rangle\langle k_x,k_y|$:

$$H^{\text{TB}}_{\text{BHZ}}=\sigma_0\otimes s_0\left[C-\frac{4D}{d^2}+\frac{2D}{d^2}\cos(dk_x)+\frac{2D}{d^2}\cos(dk_y)\right]+\sigma_z\otimes s_x\,\frac{A}{d}\sin(dk_x)$$
$$+\sigma_0\otimes s_z\left[M-\frac{4B}{d^2}+\frac{2B}{d^2}\cos(dk_x)+\frac{2B}{d^2}\cos(dk_y)\right]-\sigma_0\otimes s_y\,\frac{A}{d}\sin(dk_y).\quad(90)$$

The TB Hamiltonians derived in this section form the basis for the TB calculations performed for paper VI.

14 Transport calculations with rate equations

The plethora of transport experiments involving mesoscale quantum systems has led to a blooming of the theoretical field of modelling quantum transport. When electron-electron interactions can be neglected, one-electron transport theory is sufficient and the Landauer-Buttiker formalism [210, 211] can be employed in combination with, e.g., TB models [206]. Neglecting electron-electron interactions is a good approximation for systems in which the coupling to the leads is the dominant energy scale and when confinement effects are negligible. In transport setups involving QDs these conditions typically do not hold. As discussed in Section 2, the Coulomb interaction often plays an important role in QD systems and gives rise to interesting transport features. Common theoretical tools used in transport calculations involving QDs are, for example, the non-equilibrium Green's functions [212] and the numerical renormalization group [213] formalisms, both of which can handle the case of strong couplings to the leads. The former comes in many different versions, but typically has problems with very strong electron-electron interactions, while the latter typically cannot handle large systems or systems that are far from equilibrium. When the coupling to the leads is weak, a good option is to use the rate equations (or Pauli) approach, which falls under the category of the generalized master equations approaches [214]. Considering the standard transport scenario with one or more QDs being coupled to a number of reservoirs, the starting point of these approaches is to trace out the reservoir degrees of freedom from the total density matrix in order to obtain the reduced density matrix of the QDs. Next, an equation for the stationary state (reached after sufficiently long time) of the reduced density matrix of the QDs can be set-up and solved. Once the reduced density matrix elements have been calculated, they can be used to calculate particle currents.

Rate equations can be formally derived in the real-time diagrammatics framework [215–217] and from the second order von Neumann approach [218, 219] by ignoring processes of second and higher order in the tunnel couplings to the reservoirs and off-diagonal density matrix elements. A derivation for the second order von Neumann case can be found in Ref. [220]. Here, intuitive arguments for their validity are given instead, and a form of the equations not relying on charge being a good quantum number in the system is presented. This form is useful when superconducting pairing is present in the QDs.

The full system is described by the Hamiltonian

$$H = H_{\mathrm{QD}} + H_{\mathrm{R}} + H_{\mathrm{T}}, \tag{91}$$

where $H_{\mathrm{QD}} = \sum_a E_a \left|a\right\rangle \left\langle a\right|$ is the diagonalized QD Hamiltonian with eigenvalues

E_a and eigenvectors $|a\rangle$, $H_{\mathrm{R}} = \sum_r H_r$ is the sum of the reservoir Hamiltonians H_r, and H_{T} contains the couplings between the reservoirs and the QD. Explicitly:

$$H_r = \sum_{k\sigma} \varepsilon_{rk\sigma} c^\dagger_{rk\sigma} c_{rk\sigma}, \tag{92}$$

$$H_{\mathrm{T}} = \sum_{rk\sigma a} \left[T^{aa'}_{r\sigma+} \left|a\right\rangle \left\langle a'\right| c_{rk\sigma} - T^{aa'}_{r\sigma-} \left|a\right\rangle \left\langle a'\right| c^\dagger_{rk\sigma} \right]. \tag{93}$$

Even though arbitrary interactions are allowed on the QD, we assume that the reservoirs are noninteracting. The QD eigenstates $|a\rangle$ are many-body states of definite parity (parity here refers to the number of electrons in the QD being even or odd). The operator $c_{rk\sigma}$ annihilates an electron of spin σ in momentum state k in reservoir r and $\varepsilon_{rk\sigma}$ is the corresponding electron energy. The transition matrix elements $T^{aa'}_{r\sigma+(-)}$ are given by the expressions:

$$T^{aa'}_{r\sigma+} = \sum_l t_{rl\sigma} \left\langle a\right| d^\dagger_{l\sigma} \left|a'\right\rangle, \quad T^{aa'}_{r\sigma-} = \sum_l t^*_{rl\sigma} \left\langle a\right| d_{l\sigma} \left|a'\right\rangle = (T^{a'a}_{r\sigma+})^*. \tag{94}$$

The quantities $T^{aa'}_{r\sigma+}$ describe transitions from QD state $|a'\rangle$ to $|a\rangle$ caused by an electron with spin σ jumping from reservoir r into the QD and $T^{aa'}_{r\sigma-}$ describe the same transitions caused by electrons escaping from the QD to the reservoir, while $t_{lr\sigma}$ parametrize the coupling between the QD and the reservoir. The orbitals l can belong to the same or different QDs. From the transition matrix elements the tunneling couplings can be calculated using Fermi's golden rule [82]:

$$\Gamma^{aa'}_{r\sigma+(-)} = \sum_k \frac{2\pi}{\hbar} |T^{aa'}_{r\sigma+(-)}|^2 \delta(E_a - E_{a'} - \varepsilon_{rk\sigma}), \tag{95}$$

where the δ function is included, as the process is only allowed when the energy difference between the final and the initial state matches the energy of a mode in the reservoir. The right-hand side of the above expression is summed over k and turning the sum into an integral using the reservoir- and spin-specific DOS $\rho_{r\sigma}$ we finally obtain

$$\Gamma^{aa'}_{r\sigma+(-)} = \frac{2\pi}{\hbar} \rho_{r\sigma} |T^{aa'}_{r\sigma+(-)}|^2, \tag{96}$$

where $\rho_{r\sigma}$ was taken to be energy-independent. In order to write down the tunneling rates, one has to also factor in the occupation probabilities of the states in the reservoirs. Assuming that the reservoirs remain at thermal equilibrium at all times, the occupation probabilities follow the Fermi-Dirac distribution:

$$f_r(\varepsilon) = \frac{1}{1 + [\exp(\varepsilon - \mu_r)/(k_{\mathrm{B}} T_r)]}, \tag{97}$$

where μ_r, T_r are the chemical potential and temperature of reservoir r and k_B is the Boltzmann constant. For an electron to jump from the reservoirs into the QD, the difference between the final and the initial QD energies must correspond to an energy state with a finite occupation probability in the reservoirs. Here, we employ a weak coupling approximation and only take into account coherent tunneling of single electrons between the QD and the reservoirs. This is a good approximation for sufficiently small tunnel couplings (considerably smaller than the temperature) [220]. The rate with which electrons of spin σ are added to the QD in order to change the QD state from $|a'\rangle$ to $|a\rangle$ is

$$W_{\sigma+}^{aa'} = \sum_r \Gamma_{r\sigma+}^{aa'} f(E_a - E_{a'}) = \sum_r W_{r\sigma+}^{aa'}. \tag{98}$$

Similarly, for an electron to jump from the QD to the reservoir, there must be an available reservoir state and this process has a rate proportional to the state being unoccupied:

$$W_{\sigma-}^{aa'} = \sum_r \Gamma_{r\sigma-}^{aa'} \big[1 - f(E_{a'} - E_a)\big] = \sum_r W_{r\sigma-}^{aa'}. \tag{99}$$

The diagonal elements of the reduced QD density matrix are given by the occupation probabilities of the QD states. In our approximation, we neglect the off-diagonal entries of the density matrix (coherences). This is a good approximation as long as any (quasi-)degenerate QD eigenstates differ by a quantum number that is conserved in the total system [58, 66, 220, 221]. If there exist degenerate QD eigenstates that correspond to the same quantum numbers, coherences must be taken into account. For each state $|a\rangle$, the occupation probability P_a increases with transitions from the rest of the states $|a'\rangle$ to $|a\rangle$, weighted by the probability $P_{a'}$ of $|a'\rangle$ to be occupied. Conversely, P_a decreases with transitions having $|a\rangle$ as the initial state and any other $|a'\rangle$ as the final state, weighted by the probability that $|a\rangle$ is occupied (P_a). Therefore, we can write down the rate equation

$$\dot{P}_a = \sum_{a',\sigma} \big[W_{\sigma+}^{aa'} + W_{\sigma-}^{aa'}\big] P_{a'} - \sum_{a',\sigma} \big[W_{\sigma+}^{a'a} + W_{\sigma-}^{a'a}\big] P_a. \tag{100}$$

Note that one can get from state $|a'\rangle$ to state $|a\rangle$ both by adding (+) and removing (−) an electron to/from the QD when charge is not a good quantum number and both processes have to be taken into account. The set of Eqs. (100) is solved for the steady state $\dot{P}_a = 0$ and typically is written in the form

$$\mathbf{W}\mathbf{P} = 0, \tag{101}$$

where $\mathbf{W}$ is the rate matrix and $\mathbf{P}$ is a vector containing the probabilities P_a. The system is under-determined and the normalization condition for the probabilities

$\sum_a P_a = 1$ provides the missing equation. Once the probabilities have been calculated, the particle current flowing out of reservoir r per spin σ can be expressed by counting particles tunneling into the QD minus particles tunneling out of the QD weighted by the probabilities of the initial states:

$$I^p_{r\sigma} = \sum_{aa'} (W^{aa'}_{r\sigma+} - W^{aa'}_{r\sigma-}) P_{a'}. \tag{102}$$

The total electric current for reservoir r can be obtained summing over spin and multiplying with $-e$.

Rate equations were used for differential conductance calculations in papers I and II.

Results

15 Summary and discussion for papers I and II

Paper I focuses on the setup shown in Figure 25(a). The studied system consists of two QDs, L and R, coupled via an ABS in a central segment S, which can be a short semiconductor NW segment proximitized by a superconductor [27–29, 88, 89, 152] or a third QD strongly coupled to a superconductor. The QDs L and R are additionally coupled to two normal leads N with applied voltages V_L and V_R, included for tunnel spectroscopy. An applied global magnetic field $\mathbf{B}$ is perpendicular to a SO field $\mathbf{B}^{\mathrm{SO}}$, while the QD levels and the energy of the ABS can be controlled by gates. Figure 25(b) shows the corresponding energy level diagram with the relevant tunnel processes for the bare system (without the leads). The Hamiltonian (excluding the leads) is $H^{\mathrm{PMM}} = H_{\mathrm{QDs}} + H_{\mathrm{ABS}} + H_{\mathrm{T}}$. Here, the QDs are described by

$$H_{\mathrm{QDs}} = \sum_{\sigma,j} \varepsilon_j n_{j\sigma} + \sum_j U_j n_{j\uparrow} n_{j\downarrow} + \sum_j E_{Zj} n_{j\downarrow}, \tag{103}$$

where $n_{j\sigma} = d_{j\sigma}^\dagger d_{j\sigma}$, $d_{j\sigma}^\dagger$ creates an electron in the single-particle orbital with energy ε_j in QD $j = L, R$ with spin $\sigma = \uparrow, \downarrow$, and U_j, E_{Zj} are the charging energy and Zeeman splitting in QD j. The ABS is described by

$$H_{\mathrm{ABS}} = \sum_\sigma \varepsilon^{\mathrm{ABS}} n_\sigma^{\mathrm{ABS}} + U^{\mathrm{ABS}} n_\uparrow^{\mathrm{ABS}} n_\downarrow^{\mathrm{ABS}} + E_Z^{\mathrm{ABS}} n_\downarrow^{\mathrm{ABS}} + \Delta c_\uparrow^\dagger c_\downarrow^\dagger + \Delta^* c_\downarrow c_\uparrow, \tag{104}$$

where $n_\sigma^{\mathrm{ABS}} = c_\sigma^\dagger c_\sigma$, $c_\sigma^\dagger$ creates an electron in the single-particle orbital of the central part with energy $\varepsilon^{\mathrm{ABS}}$ and spin σ, and Δ, U^{ABS}, and E_Z^{ABS} are the induced superconducting pairing, charging energy and Zeeman splitting in the central part. The tunneling between the QDs and the ABS is given by

$$H_{\mathrm{T}} = \sum_{\sigma,j} t_j d_{j\sigma}^\dagger c_\sigma + \sum_\sigma s_\sigma \left[t_L^{\mathrm{SO}} d_{L\sigma}^\dagger c_{\bar{\sigma}} + t_R^{\mathrm{SO}} c_\sigma^\dagger d_{R\bar{\sigma}} \right] + \mathrm{H.c.}, \tag{105}$$

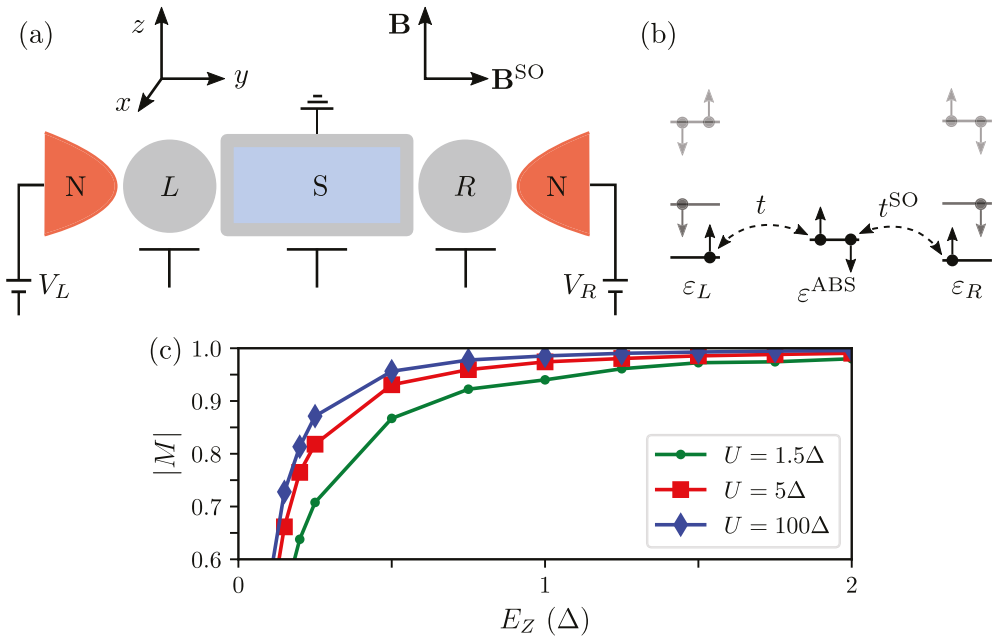

Figure 25: (a) The PMM system. Two QDs, L and R, are coupled via a proximitized by an s-wave superconductor central part S that hosts an ABS. The QDs are additionally coupled to normal leads N. The system is subject to a magnetic field $\mathbf{B}$ and a SO field $\mathbf{B}^{\mathrm{SO}}$. (b) Corresponding energy level diagram, where t and t^{SO} are the amplitudes for spin-preserving and spin-flipping tunneling processes. (c) Maximum calculated MP at even-odd ground-state degeneracies as a function of E_Z for different values of U. The figure is adapted from paper I.

where t_j, t_j^{SO} are the amplitudes for spin-preserving and spin-flipping hopping between QD j and the ABS, $s_{\uparrow,\downarrow} = \pm 1$, and $\bar{\sigma}$ denotes the opposite spin compared to σ.

In paper I, we showed that controlling the energies of the QD orbitals and the energy of the ABS, the system can be tuned to sweet spots with two degenerate ground states of even and odd fermion number parity. The sweet spots host PMMs similar to the ones described in Ref. [151] and in Section 10. The physical mechanism that enables this control is explained in detail in paper I and is closely related to the one described in Ref. [152] and in Section 10. The novelty here is that the PMMs emerge in the presence of interactions, with a finite Zeeman field, and for large couplings between the QDs and the ABS. Due to the finite Zeeman field, the PMMs are not perfectly localized in QDs L and R, and introducing a measure that quantifies the PMM localization is necessary. The Majorana polarization (MP) is such a measure [222–224], as it quantifies the degree to which a Hermitian operator localized on one QD can switch between the even

and the odd parity ground states. The MP is given by

$$M_j = \frac{\sum_\sigma \left(w_\sigma^2 - z_\sigma^2\right)}{\sum_\sigma \left(w_\sigma^2 + z_\sigma^2\right)}, \tag{106}$$

with $w_\sigma = \langle o|(d_{j\sigma} + d_{j\sigma}^\dagger)|e\rangle$ and $z_\sigma = \langle o|(d_{j\sigma} - d_{j\sigma}^\dagger)|e\rangle$, where $|e\rangle$, $|o\rangle$ are the even and the odd parity ground states. The values of $|M_j|$ lie in the interval $[0, 1]$. If only one PMM is present in QD j we have $|M_j| = 1$, while $|M_j| < 1$ implies the presence of additional PMMs. The sweet spots are thus characterized by: *(i)* a doubly-degenerate ground state with even-odd fermion number parity, *(ii)* a finite gap between the ground state and the excited states, and *(iii)* a high value of the MP.

In paper II, we additionally considered a low-energy model and a corresponding low-energy MP:

$$H^{\text{lowE}} = \xi\gamma\tilde{\gamma}, \quad M_L^{\text{lowE}} \approx \frac{1-\zeta^2}{1+\zeta^2}, \quad M_R^{\text{lowE}} \approx -\frac{1-\tilde{\zeta}^2}{1+\tilde{\zeta}^2}, \tag{107}$$

where ξ is the energy of the lowest-energy fermionic mode in the system composed of the PMMs γ and $\tilde{\gamma}$. At the sweet spot $\xi = 0$. For a high MP, γ ($\tilde{\gamma}$) is mainly localized in QD L (R). The parameter ζ ($\tilde{\zeta}$) corresponds to the part of $\tilde{\gamma}$ (γ) that is present in QD L (R). The magnitude of ζ lies in the interval $[0, 1]$, with $\zeta = 0$ implying perfectly localized PMMs. The low-energy model was used in order to gain intuitive understanding and to study the effect of having imperfect PMMs on nonabelian operations.

Turning back to the spinful model and H^{PMM}, Figure 25(c) shows the maximum values of the MP ($|M| = |M_L| = |M_R|$) calculated for sweet spots as a function of E_Z and for different charging energies U on the QDs. For a large E_Z, the MP is very close to 1 with almost perfectly localized PMMs, as the system is in a regime that is captured by the spinless model of Ref. [151] (see also Section 10). For lower E_Z, the maximum MP for the sweet spots decreases but a high U contributes to retaining high MP values. Experimentally relevant parameters $U \approx 5\Delta$, $E_Z \approx 1.5\Delta$ [27–29, 88, 89] correspond to $|M| \approx 0.986$. For very low E_Z, even-odd degeneracies still exist, but they correspond to low MP values. For these "low-MP sweet spots" the PMMs are not well-localized in the QDs.

15.1 Navigating to the sweet spot

In Section 8 we saw that local and nonlocal conductance measurements can be used to detect MBSs in MNWs. The corresponding setup for the PMM system

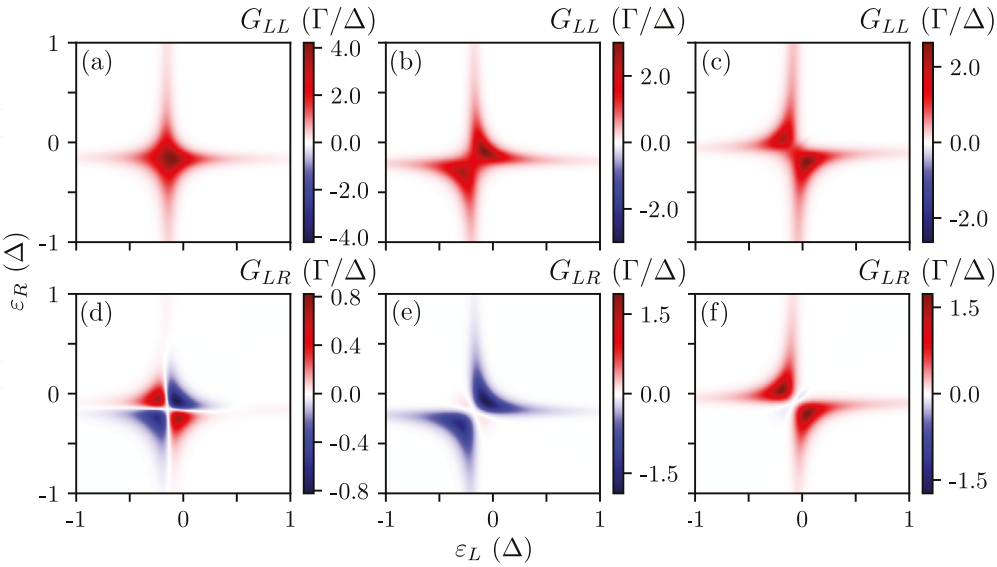

Figure 26: (a, b, c) Zero-bias local conductance G_{LL} as a function of the QD energies ε_L, ε_R for (a) $\varepsilon^{\mathrm{ABS}}$ tuned to the sweet spot value, (b) $|\varepsilon^{\mathrm{ABS}}|$ larger than the sweet spot value, and (c) $|\varepsilon^{\mathrm{ABS}}|$ smaller than the sweet spot value. (d, e, f) As in (a, b, c) but the nonlocal conductance G_{LR} is plotted instead. Γ is the tunnel coupling between the QDs and the N leads. The figure is adapted from paper I.

is shown in Figure 25(a). Figure 26(a) shows the calculated local differential conductance $G_{LL} = dI_L/dV_L$ at zero bias voltage as a function of the QD energies $\varepsilon_L, \varepsilon_R$ for $\varepsilon^{\mathrm{ABS}}$ tuned to the sweet spot value. The peaks of G_{LL} coincide with the even-odd degeneracy lines and the sweet spot is located at the point where the degeneracy lines cross. This is not the case for a detuned $\varepsilon^{\mathrm{ABS}}$ as can be seen in Figures 25(b, c), where the degeneracy lines anti-cross. One can thus navigate to the sweet spot with local conductance measurements. Depending on the temperature, however, the features of Figures 25(a, b, c) can be hard to discern. Nonlocal conductance, on the other hand, gives rise to more distinct features. In Figure 26(d), $G_{LR} = dI_L/dV_R$ is plotted for the same parameters and in the same range as in Figure 25(a). We notice that G_{LR} vanishes along the degeneracy lines and that the negative and positive components of G_{LR} close to the sweet spot have comparable magnitudes. The picture is qualitatively very different for the detuned situations in Figures 25(e) and (f), where the parameters are the same as in Figures 25(b) and (c) respectively. The peaks of G_{LR} coincide with the degeneracy lines and G_{LR} is dominated by either negative [Figure 25(e)] or positive [Figure 25(f)] components. An additional way to identify sweet spots in the same setup by comparing local conductance peaks with quantum capacitance measurements is described in paper II.

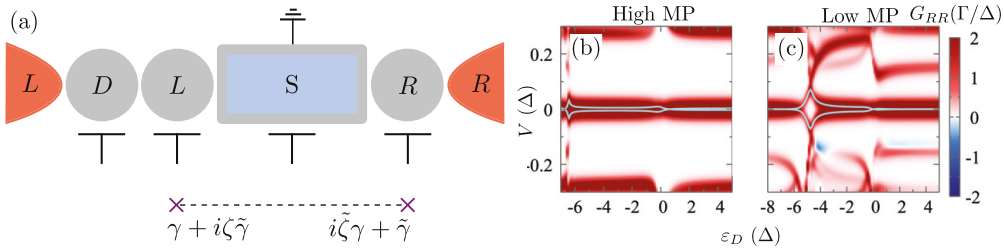

Figure 27: (a) The PMM system coupled to an additional QD D in order to assess the PMM quality with local conductance (upper panel) and sketch of PMMs in the low-energy model (lower panel). (b, c) Local differential conductance G_{RR} of the combined system as a function of ε_D and bias voltage $V/2 = V_L = -V_R$. The light-blue lines denote the splitting between the lowest-energy even and odd parity states. In (b) $|M| \approx 0.986$ in the bare PMM system while in (c) $|M| \approx 0.661$. The figure is adapted from paper II.

15.2 Quality assessment of PMMs

The MP is a useful quantity to theoretically assess the quality of PMMs, but it is important to find experimental signatures that would indicate whether a PMM system has a high or low MP. For this purpose, the setup shown in Figure 27(a) was proposed in paper II. The difference between this setup and the setup in Figure 25(a) is that an additional, spinful, QD D with single-particle orbital energy ε_D is placed between the QD L and the lead L. A similar setup was proposed in Refs. [118, 139–141] and was described in Section 8 as an experimentally accessible way to assess the quality of MBSs in MNWs. The local conductance G_{RR} of the combined system (PMM system + QD D) was calculated after expanding H^{PMM} to include the QD D and the corresponding couplings. It is plotted in Figures 27(b, c) as a function of ε_D and a symmetric bias voltage $V/2 = V_L = -V_R$ for PMM systems tuned to the sweet spot. In Figure 27(b), $|M| \approx 0.986$ in the bare PMM system, and the imperfect localization of PMMs manifests as a splitting in the ground state energy indicated by the light-blue lines close to zero bias. The splitting is small and because of finite temperature effects it is not apparent as a splitting in the zero-bias conductance peak. In Figure 27(c) $|M| \approx 0.661$, the energy splitting is considerably larger, and this translates to a clearly visible splitting of the zero-bias conductance peak. Thus, the splitting of the zero-bias peak of G_{RR} can be considered as a PMM quality measure. In terms of the low-energy model, a MP smaller than 1 implies a finite presence $i\zeta\tilde{\gamma}$ of $\tilde{\gamma}$ in QD L [see lower panel in Figure 27(a)]. As a result, QD D couples to both PMMs and the ground state degeneracy of the combined system is lifted since there is no uncoupled PMM left.

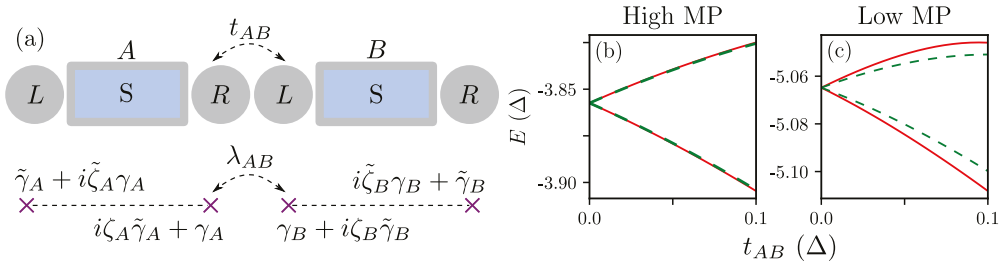

Figure 28: (a) Upper panel: Two coupled PMM systems, A and B, with tunneling amplitude t_{AB} between QDs AR and BL. Lower panel: Sketch of PMMs in the low-energy model. λ_{AB} couples the PMM components in QDs AR and BL. (b, c) The four lowest-energy eigenvalues in the even and the odd parity sector as a function of t_{AB}. In (b) $|M| \approx 0.986$ in the uncoupled PMM systems while in (c) $|M| \approx 0.661$. The figure is adapted from paper II.

15.3 Coupled PMM systems and PMM qubits

In Section 9.2 we established that in order to define a MBS qubit at least four MBSs are required. Moreover, to realize the type of trijunction used for braiding in Section 9.3, three coupled MNWs are needed. It is thus important to study coupled PMM systems to proceed with PMM qubits and braiding. In paper II, two coupled PMM systems, A and B, were initially considered as shown in Figure 28(a). The Hamiltonian of the system is a straightforward generalization of H^{PMM} for two PMM systems, with additional coupling terms. The amplitude for tunneling between QD R in system A (AR) and QD L in system B (BL) is t_{AB}. The four lowest-energy eigenevalues in the even and the odd parity sector as a function of t_{AB} for PMM systems with $|M| = 0.986$ tuned to their sweet spots are plotted in Figure 28(b). At the sweet spot, each isolated system has two degenerate ground states corresponding to even ($|e\rangle$) and odd ($|o\rangle$) parity. For $t_{AB} = 0$, the total system has four degenerate ground states, two with total even parity ($|e_A\rangle\,|e_B\rangle \equiv |ee\rangle$, $|oo\rangle$) and two with total odd parity ($|oe\rangle$, $|eo\rangle$). For $t_{AB} \neq 0$ the degenerate states split (almost) equally in the even (red continuous lines) and the odd (green dashed lines) parity sector. As a result, the ground state remains (almost) two-fold degenerate even for finite t_{AB}. The effect of lower MP is seen in Figure 28(c), where $|M| = 0.661$. The finite coupling splits the states in each parity sector differently, and as a result, the even-odd splitting of the ground state is larger compared to the case with high MP.

These results can be explained in terms of the low-energy model and the finite components of PMMs mainly localized in AL ($\tilde{\gamma}_A$) and BR ($\tilde{\gamma}_B$) in the coupled QDs AR and BL [see the lower panel of Figure 28(a)]. The generalization of

$H^{\rm lowE}$ for two coupled systems is

$$H_{AB}^{\rm lowE} = \frac{i}{2}\sum_{s=A,B}\xi_s\gamma_s\tilde{\gamma}_s + \frac{i}{4}\left[\lambda_{AB}(\gamma_A - i\zeta_A\tilde{\gamma}_A)(\gamma_B + i\zeta_B\tilde{\gamma}_B) - \text{H.c.}\right]. \quad (108)$$

According to the discussion in Section 9, the four PMMs can be used to define a qubit in the even or the odd parity sector. For the fermions $f_s = \frac{1}{2}(\gamma_s + i\tilde{\gamma}_s)$, where $s = A, B$, in the even parity sector we find $\sigma_z = -i\gamma_A\tilde{\gamma}_A = -i\gamma_B\tilde{\gamma}_B$, $\sigma_y = i\gamma_A\gamma_B = -i\tilde{\gamma}_A\tilde{\gamma}_B$, $\sigma_x = -i\gamma_A\tilde{\gamma}_B = -i\tilde{\gamma}_A\gamma_B$, while in the odd parity sector $\sigma_z = -i\gamma_A\tilde{\gamma}_A = i\gamma_B\tilde{\gamma}_B$, $\sigma_y = i\gamma_A\gamma_B = i\tilde{\gamma}_A\tilde{\gamma}_B$, $\sigma_x = i\gamma_A\tilde{\gamma}_B = -i\tilde{\gamma}_A\gamma_B$. The coupling λ_{AB} is complex in general, but its phase can be controlled if we couple the superconductors that proximitize the central parts in a loop. With a real and positive λ_{AB}, $H_{AB}^{\rm lowE}$ in the even and the odd parity sector can be written as

$$\begin{aligned} H_{AB,e}^{\rm lowE} &= -\frac{\xi_+}{2}\sigma_z + \frac{\lambda_{AB}}{2}(1 - \zeta_A\zeta_B)\sigma_y, \\ H_{AB,o}^{\rm lowE} &= -\frac{\xi_-}{2}\sigma_z + \frac{\lambda_{AB}}{2}(1 + \zeta_A\zeta_B)\sigma_y, \end{aligned} \quad (109)$$

where $\xi_\pm = \xi_A \pm \xi_B$. At the sweet spot $\xi_{A(B)} = 0$. For an MP close to 1, $\zeta_{A(B)} \approx 0$, the weights of $\tilde{\gamma}_A$ and $\tilde{\gamma}_B$ in the coupled QDs are not significant, and the states in the even and the odd subspace split almost equally. As a result, the even-odd ground state degeneracy remains almost intact. This is what is seen as an almost zero ground state splitting for $t_{AB} \neq 0$ in Figure 28(b). For a low MP and significant $\zeta_{A(B)}$, the difference in the splittings between the even and the odd states becomes important. This explains the significant splitting between the even and the odd states in Figure 28(c). Additionally, the difference between the frequency of the qubit rotation about the y axis in the even and the odd computational space provides a PMM quality measure in the time domain.

15.4 Nonabelian operations with PMMs

In paper II, braiding with PMMs was considered, and the effect of the imperfect MP on charge transfer-based [180, 184, 185], measurement-based [179, 182, 183], and hybridization-induced [142–150] braiding was investigated. The protocols were simulated using generalizations of Eq. (108) for more than two PMM systems and additional QDs. The charge transfer-based braiding protocol requires a simple setup with two PMM systems and an additional QD but poses very stringent requirements on the PMM quality ($|\zeta| \leq 0.01$) in order to reproduce the topological MBS results. The measurement-based braiding protocol involves a setup with three PMM systems coupled to two additional QDs. The protocol

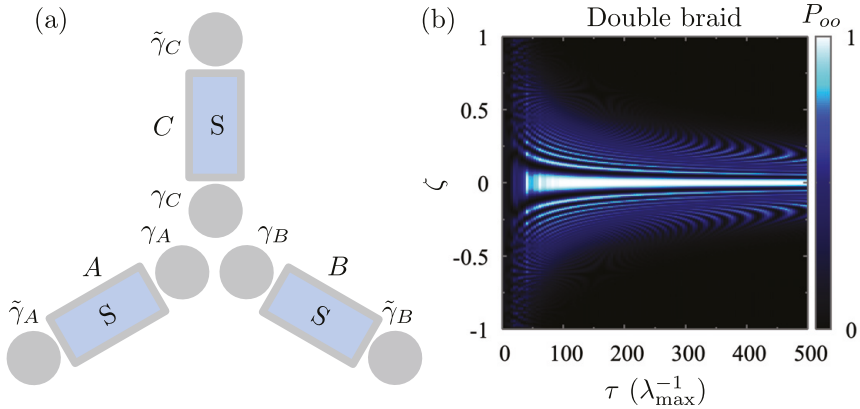

Figure 29: (a) Three PMM systems A, B, and C coupled in a trijunction geometry. The PMMs with the highest contribution per QD for $\zeta = \zeta_A = \zeta_B = \zeta_C \approx 0$ are also depicted. (b) Probability to measure the state $|o_A o_B\rangle \equiv |oo\rangle$ after a double braid as a function of ζ and protocol duration τ. The maximum value of the couplings between systems A, B, and C is $\lambda_{\max}$. The figure is adapted from paper II.

reproduces the topological MBS results for an MP equal to 1 ($\zeta = 0$). However, it was found that these results can be mimicked by QPs in the fermionic limit $|\zeta| = 1$. This requires some extra care in order to identify false positives.

For hybridization-induced braiding, we considered a setup and protocol similar to the ones presented in Section 9.3 and Figure 19. The setup is shown in Figure 29(a) and involves three PMM systems A, B, and C. For $\zeta = \zeta_A = \zeta_B = \zeta_C = 0$, the PMMs are fully localized as indicated in Figure 29(a) and the protocol exchanges γ_A and γ_B. Starting from an even parity in PMM systems A and B ($|e_A e_B\rangle \equiv |ee\rangle$), after a double braid the state becomes $|oo\rangle$ with 100% probability ($P_{oo} = 1$). Figure 29(b) shows the calculated probability P_{oo} as a function of ζ and the duration of the protocol τ. The protocol gives a result very close to the ideal one for $|\zeta| \lesssim 0.1$ and for a wide range of protocol durations. $|\zeta| = 0.1$ corresponds to an MP around 0.98 which is within experimental reach [27–29, 88, 89], as an MP of 0.986 corresponds to a $E_Z = 1.5\Delta$ [see Figure 25(c)].

16 Summary and discussion for papers III and IV

16.1 Paper III

Paper III studies a QW epitaxially defined in an InAs NW as sketched in Figure 30(a). The QW is created by two thick WZ barriers surrounding a narrow

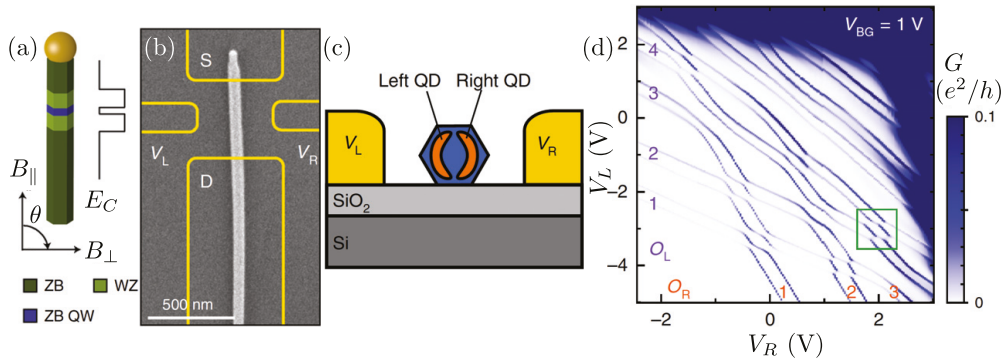

Figure 30: (a) ZB InAs QW formed by two WZ barriers in an otherwise ZB NW. The directions of the magnetic fields with respect to the NW axis are also shown. (b) Scanning electron microscope (SEM) image of the studied NW. The positions of contacts and gates are sketched with yellow lines. (c) Schematic side view of the setup where the QDs L and R are depicted. (d) Charge stability diagram of the DQD with the orbital numbers noted. The figure is adapted from paper III.

ZB area. The NW is tunnel-coupled to metallic leads S and D for transport spectroscopy, while the QW levels can be electrostatically tuned with the side-gate voltages V_L and V_R, see Figure 30(b). For low electron numbers in the QW, two QDs, left (L) and right (R), are formed and they are schematically depicted in Figure 30(c). Figure 30(d) shows the zero-bias conductance G for varying V_L and V_R. The conductance peaks indeed follow the characteristic for DQDs honeycomb pattern (see Section 2.3). The system has been studied in previous works [68–70] in a regime where the first orbital in QD L ($O_L = 1$) is close to degeneracy with the first orbital in QD R ($O_R = 1$), which is referred to as the $(1, 1)$ crossing. Observing higher orbital crossings an additional pattern emerges. Crossings that involve an even (odd) orbital in QD L (R) and an odd (even) orbital in QD R (L) are sharper than crossings involving only even or odd orbitals. The reason behind this "even-odd rule" will become clear in the following.

Each orbital crossing involves four orbitals which can be unoccupied or occupied by one to four electrons. Disregarding the rest of the electrons in the DQD, we refer to the situation of occupying one, two, three, or four orbitals involved in the crossing, as being in the 1e, 2e, 3e, or 4e regime respectively. Paper III mainly focused on the 1e regime in crossing $(2, 3)$ [green rectangle in Figure 30(d)]. In the 1e regime only the ground state is occupied and information on the three excited states can be extracted with cotunneling spectroscopy. We stress here that this terminology is relevant for one-electron physics and does not refer to the many-body ground state and excited states which would involve all the electrons in the DQD. Figure 31(a) shows the differential conductance dI/dV_DS as a function of the bias voltage V_DS between the leads and an applied magnetic

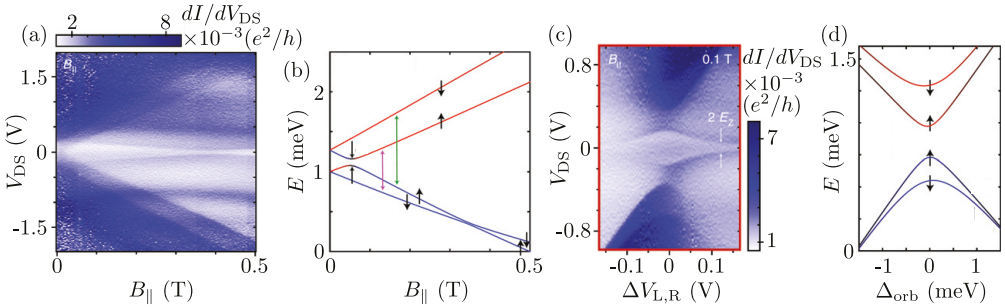

Figure 31: (a) Measured dI/dV_{DS} as a function of V_{DS} and $B_\parallel$ in the 1e regime of the (2,3) crossing. (b) Calculated energies of the states involved in the 1e regime of the (2,3) crossing as a function of $B_\parallel$. The green and purple arrows denote the energies used to extract g-factors. (c) Measured dI/dV_{DS} as a function of V_{DS} and $\Delta V_{L,R}$ in the 1e regime of the (2,3) crossing for $B_\parallel = 0.1$ T. (d) Calculated energies of the states involved in the 1e regime of the (2,3) crossing as a function of Δ_{orb} for $B_\parallel = 0.1$ T. The figure is adapted from paper III.

field $B_\parallel$ parallel to the NW axis in the 1e regime of the (2,3) crossing. Effective g-factors g^* can be extracted at a finite magnetic field from the energy splitting between states that are degenarate for zero magnetic field. Giant g-factors ($|g^*| \approx 59, 83$) in comparison to the bulk InAs value ($g^*_{InAs} = -14.9$ [225, 226]) were estimated from Figure 31(a). Additionally, the g-factor enhancement was only observed for a magnetic field parallel to the NW axis while it was quenched for a perpendicular magnetic field ($|g^*| \approx 3$). Another important feature is that the g-factors decay rapidly when moving away from orbital degeneracy. This is apparent in Figure 31(c) which shows dI/dV_{DS} as a function of V_{DS} and the DQD detuning from the (2,3) crossing $\Delta V_{L,R}$ in the 1e regime (at the crossing $\Delta V_{L,R} = 0$). The splitting between the excited state and the ground state is maximal for $\Delta V_{L,R} = 0$ and decreases for $\Delta V_{L,R} \neq 0$.

The g-factor enhancement was attributed to orbital contributions [227] due to the formation of ring-like states. This explains the highly anisotropic g-factor, as orbital contributions are absent for a magnetic field perpendicular to the formed rings. SO interaction and the alignment of an even (odd) orbital from QD L with an odd (even) orbital from QD R were found to be the necessary ingredients for the formation of such states. Significantly enhanced g-factors have also been observed in carbon nanotubes [228] and semiconductor NWs [229, 230] without the formation of DQDs. The novelty in this system is that the g-factor enhancement can be controlled by electrical means, since, detuning the DQD from orbital degeneracy destroys the ring-like states and leads to a fast decay of the g-factor.

The experimental findings were supported by three theoretical models. The first one relied on 3D modelling of the electrostatic environment of the segment of

the NW containing the DQD and the WZ barriers. Once the electrostatic potential on the DQD was determined, it was used as input to a single-electron Hamiltonian in the effective mass approximation. The software COMSOL was used to obtain the potential and solve the Schrödinger equation. Several parameters were adjusted to match the experimentally extracted g-factors and the energy spectrum in the $(2,3)$ crossing. For example, Figure 31(b) shows the magnetic field dependence of the four states involved in the (2,3) crossing in the 1e regime. The g-factors can be extracted from energy differences in a similar manner as in Figure 31(a). Figure 31(d) shows the energies of the four states involved in the (2,3) crossing as a function of detuning Δ_{orb}. We observe that the splitting between the ground state and the first excited state is maximal at orbital degeneracy and decreases with detuning, similarly to Figure 31(c).

The second model was more minimalistic, yet it succeeded in capturing the important physics of the device. The DQD system was modelled as a 1D TB ring split in two half rings (L and R) by a potential barrier. The starting point for this model was similar to the 1D TB Hamiltonian of the Rashba NW presented in Section 13.4 with periodic boundary conditions. With this model, it was possible to show that the states involved in (even, odd) and (odd, even) crossings correspond to ring-like states as they carry a finite angular momentum [$\langle L_z \rangle \approx 1\hbar$ for the $(2,3)$ crossing]. In contrast, the states of (odd, odd) and (even, even) crossings do not form ring-like states [$\langle L_z \rangle \approx 0$ for the $(2,2)$ crossing]. Using this model we also showed that the g-factor can be much more effectively tuned for the ring-like states of the $(2,3)$ crossing in comparison to the states of an actual ring. For the former, the g-factor can be quenched to 30% of its maximum value with a detuning of approximately 1 meV from orbital degeneracy. At this detuning range the g-factor for a perfect ring was found to practically not be affected at all.

The third model employed a perturbation theory analysis in the degenerate subspaces of the $(2,2)$ and the $(2,3)$ crossings. The unperturbed system consists of the two separated QDs L and R and the perturbation couples the QDs at two points to form a ring. The first-order correction to the energy and thus the splitting of the degenerate states was found to be proportional to the SO interaction strength for the $(2,3)$ crossing and to the spin-preserving tunneling strength for the $(2,2)$ crossing. This explains the experimentally observed sharp features and the anti-crossings shown in Figure 30(d), as the SO coupling is significantly smaller than the spin-preserving tunneling. Inspecting the perturbed wavefunctions it was also found that their absolute values are more uniform across the two QDs in the $(2,3)$ case. This justifies the ring-like picture, as for a perfect ring the absolute values of the wavefunctions are constant. Since it is straightforward to

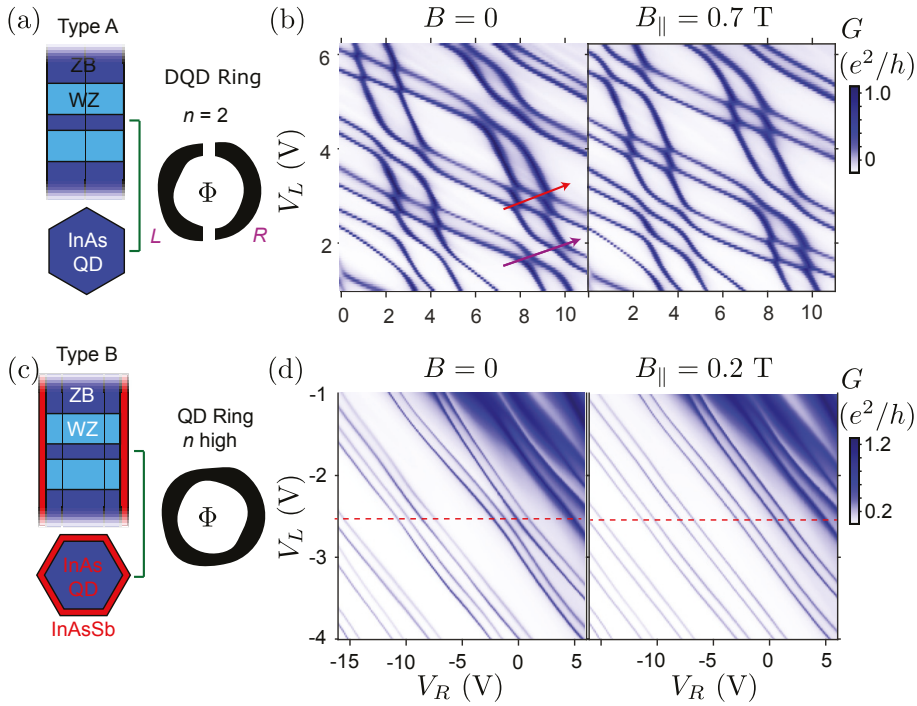

Figure 32: (a) The DQD Type A system, which can be viewed as a ring with two barriers. The system has a two-fold rotational symmetry ($n = 2$). (b) Characteristic honeycomb pattern for the conductance of a DQD. Crossings with sharp features for $B = 0$ turn to anti-crossings for $B_{\parallel} = 0.7$ T and vice versa. The red and purple vectors mark the $(6, 3)$ and $(5, 3)$ crossings respectively. (c) The ring QD Type B system is created with an extra InAsSb layer. The system is considered to be a coherent quantum ring with a symmetry axis of high order (n high), with small local deformations. (d) Conductance measurements for the Type B ring QD system. The grouping of states (four states per group) is characteristic for a quantum ring. At $B_{\parallel} = 0.2$ T the grouping is lost and only pairs of states appear. The states within each pair are separated by the Zeeman splitting which is much smaller than the splitting between states of different angular momenta (different pairs). This shows large orbital contributions to the effective g-factor. The figure is adapted from paper IV.

generalize these results to other crossings, this model explains why the even-odd rule works.

Details on modeling and experimental data on more crossings can be found in the Supplementary Information of paper III.

16.2 Paper IV

Two types of systems were investigated in this paper. The Type A system is similar to the DQD system in paper III and is shown in Figure 32(a). The main difference here is that crossings of higher orbitals were studied and the evolution of these crossings under a higher magnetic field was recorded. It was found that

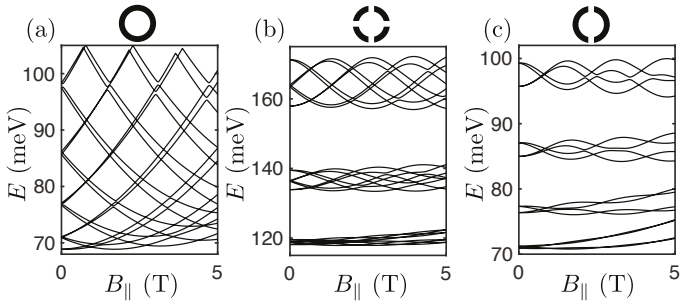

Figure 33: $B_\parallel$ evolution for the states of (a) a perfect ring (C_∞ symmetry), (b) a ring with four barriers (C_4 symmetry), and (c) a ring with two barriers (C_2 symmetry). The figure is adapted from paper IV.

the crossings that correspond to ring-like states for $B = 0$ (with an odd and an even orbital aligned) are not ring-like for $B_\parallel = 0.7$ T, whereas the opposite is true for the crossings not corresponding to ring-like states at $B = 0$ (with two odd or two even orbitals aligned). These features can be seen in Figure 32(b), where crossings that are sharp and are only split by the SO interaction for $B = 0$ turn to anti-crossings for $B_\parallel = 0.7$ T and vice versa. An explanation is provided by an extension of the degenerate perturbation theory analysis employed in paper III. For a flux through the DQD system equal to half a flux quantum ($\phi = 0.5h/e$) corresponding to $B_\parallel = 0.7$ T, the overlap integrals between the QDs L and R change sign [gaining a phase $\exp(i\pi/2)$] so that the (odd,odd) and (even,even) crossings are now the ones only split by the SO interaction. Threading another half a flux quantum through the DQD, one period is completed and the system returns to the $B = 0$ behavior.

The Type B system is similar to the Type A system with an additional InAsSb layer covering the NW (and thus the DQD), forming a ring QD as depicted in Figure 32(c). The formation of a single QD is apparent from the conductance measurements shown in Figure 32(d) and the absence of the honeycomb pattern. Moreover, the grouping of four states that split only by the charging energy is characteristic for the energy spectrum of a quantum ring with orbital and spin degeneracy.

A perfect quantum ring threaded by a magnetic flux exhibits the Aharonov-Bohm effect [231] and the different angular momentum states cross for an increasing $B_\parallel$. A TB model was used to calculate the energy spectrum of such a ring, shown in Figure 33(a). The energy spectra of rings with various types of barriers under a magnetic field have been studied both theoretically [232, 233] and experimentally [234]. A perfect ring has an infinite rotational symmetry C_∞ and rings with lower symmetry can be studied by including appropriate

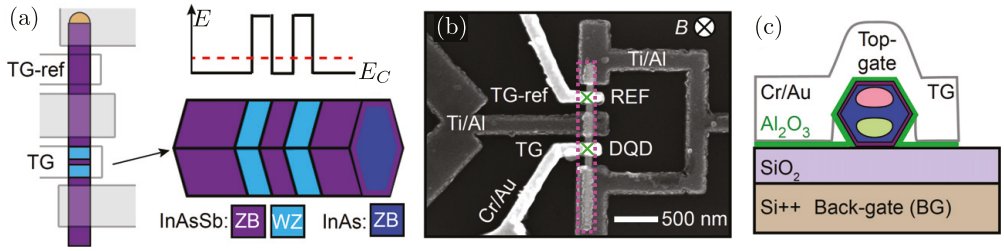

Figure 34: (a) Sketch of the NW and close-up from the part with the WZ barriers along with the corresponding band diagram. (b) SEM image of the setup. The NW is outlined with drawn purple dots and the Josephson junctions are depicted with green crosses. Cr/Au top-gates (TG) are used to tune the orbitals of the DQD and the transmission of REF. The SQUID loop is made of Ti/Ai. (c) Sketched cross-section of the NW. For low electron occupancies the QD breaks into a parallel DQD configuration. The DQD orbitals are also controlled by a Si++ back-gate (BG). The figure is adapted from paper V.

barriers. Anti-crossings between different angular momentum states of these imperfect rings lead to gaps in their energy spectra and the grouping of states according to the rings' symmetries. Figure 33(b) shows the calculated spectrum for a ring with four barriers as a function of $B_{\parallel}$. The system has a C_4 rotational symmetry which leads to the grouping of states in groups of four (not counting spin). Aharonov-Bohm oscillations also appear, with a period completed for a flux through the ring equal to one flux quantum. Similarly, the Type A DQD system can be viewed as a ring with two barriers corresponding to a C_2 rotational symmetry and the calculated spectrum can be seen in Figure 33(c). This system does not exhibit ring-like states for $B = 0$ but for half a flux quantum threading the ring instead, where an approximate four-fold degeneracy is observed. Details on the TB model can be found in the Supporting Information of paper IV.

17 Summary and discussion for paper V

In paper V, an InAs/InAsSb core/shell NW was studied in a SQUID geometry. The NW is mainly in the ZB crystal phase and closely separated WZ barriers epitaxially define a QD. Figure 34(a) shows a sketch of the NW and a close-up of the QD segment with the corresponding band diagram. The structure of the NW is similar to the Type B system of paper IV. Figure 34(b) shows an SEM image of the SQUID and the position of the NW is outlined with drawn purple dots. A superconducting Ti/Al loop connects the ends of the NW, while the central part of the NW is also covered by a Ti/Al arm. This creates two Josephson junctions marked with green crosses. We focus on the Josephson junction containing the WZ segments, while the other, ZB junction serves as a reference (REF). For low electron occupancies the QD breaks into a

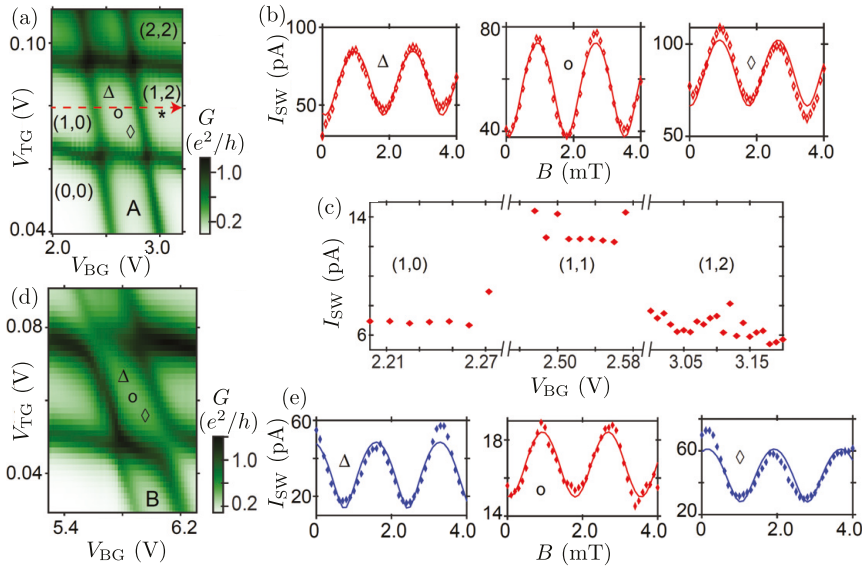

Figure 35: (a) Charge stability diagram for the weak-coupling crossing I. (b) I_{SW} as a function of B for the points in the (1,1) regime marked in (a). (c) I_{SW} for a varying V_{BG} along the red arrow shown in (a). (d) Charge stability diagram for the intermediate-coupling crossing II. (e) I_{SW} as a function of B for the points in the (1,1) regime marked in (d). In the panels corresponding to a π phase lines and points are plotted in red, while in the ones corresponding to a 0 phase they are plotted in blue. The figure is adapted from paper V.

parallel-coupled DQD configuration, see Figure 34(c). The formation of a DQD is attributed to local potential variations, reinforced by a top-gate (TG) and a back-gate (BG) which control the DQD orbitals.

The magnetic flux through the SQUID is controlled by a perpendicular magnetic field B. The current-phase relation is extracted by applying an increasing current bias at different B values and measuring the differential resistance dV/dI through the SQUID. The switching current I_{SW} for each B value is estimated as the maximum current for which $dV/dI \approx 0$. For a larger current superconductivity is destroyed and dV/dI becomes finite abruptly.

Current-phase relations for three orbital crossings with different tunnel couplings were extracted. In analogous experiments with a single QD, a π shift was observed in the SQUID current-phase relation for an odd QD occupation, which implies a π shift in the QD current-phase relation [93, 235]. Thus, for spin-1/2 states, a single QD behaves as a π-junction. In paper V, it was found that the DQD can, for certain configurations, exhibit a π phase for spin-1/2 states such as (0,1) and (1,0), where (n_T, n_B) denote the occupations of the orbitals controlled by the TG and the BG at a specific crossing. This is non-trivial, as seen as isolated tunneling channels, $n_{T(B)} = 0$ contributions lead to a 0 phase, while

$n_{\mathrm{T(B)}} = 1$ contributions to a π phase. Whether the DQD exhibits a π phase or not depends on the competition between these two contributions [236–238].

Figure 35(a) shows zero-bias conductance measurements as a function of the BG and TG voltages V_{BG} and V_{TG} for crossing I, which is the crossing with the weakest coupling between the QDs. Crossing I involves the first orbital in the TG-controlled QD (orbital-1) and the first orbital in the BG-controlled QD (orbital-A). It exhibits a π phase for almost all the regimes with an odd total occupation in the DQD. The only exception is the (2,1) regime that shows a 0 phase. This was attributed to an increased coupling between the DQD and the superconducting lead once orbital-1 is filled, which makes it the main transport channel for CPs [239, 240]. The current-phase relations for the mentioned regimes can be found in the Supplemental Material of paper V.

Here, we focus on the (1,1) regime. The panels of Figure 35(b) show the current-phase relation for three points in the (1,1) regime that are marked in Figure 35(a). Interestingly, a π phase was observed, regardless of the detuning from the center of the (1,1) regime. This can be understood from the weak coupling between the two QDs at crossing I, where transport basically takes place via two independent spin-1/2 channels, each contributing to a π phase. Figure 35(c) shows measurements of I_{SW} along π-phase regimes as depicted by the red arrow in Figure 35(a). The picture of independent channels is supported by the fact that I_{SW} is approximately doubled in the (1,1) regime.

Figure 35(d) shows the corresponding charge stability diagram for crossing II. It involves orbital-1 and the second orbital in the BG-controlled QD, orbital-B. A much larger coupling between the QDs is observed in this crossing. The panels of Figure 35(e) show the current-phase relation for three points in the (1,1) regime that are marked in Figure 35(d). We see that the π phase survives only close to the center of the (1,1) regime (second panel, red line and points), while detuning away from the center a 0 phase is observed (first and third panel, blue lines and points). Thus, control of the orbitals and the hybridization in the DQD can induce a $\pi - 0$ transition. This transition can be attributed to the increasing double occupation of the individual QDs for an increasing coupling strength, which favors the 0 phase. For crossing III, the hybridization was even stronger, and as a result, no π phase was observed in the (1,1) regime.

The interpretation of the experimental findings was supported by theoretical calculations. We modelled the DQD Josephson junction in the ZBW approximation and calculated the Josephson current using

$$I_{\mathrm{J}} = \frac{2e}{\hbar}\frac{dE_{\mathrm{GS}}}{d\varphi}, \tag{110}$$

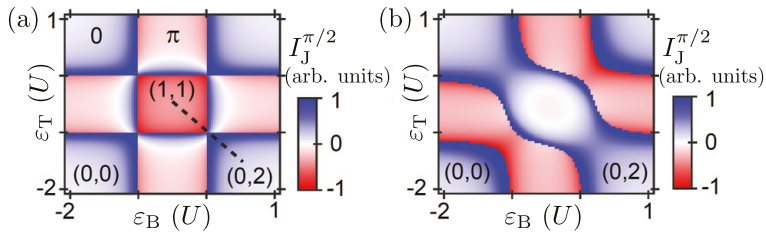

Figure 36: (a) Calculated $I_J^{\pi/2}$ for the DQD Josephson junction as a function of the orbital energies ε_T and ε_B for a coupling $t \approx 0$ between the QDs. (b) As in (a) but for $t = 0.2U$. The figure is adapted from paper V.

where E_{GS} is the ground state energy and φ is the phase difference between the two superconductors forming the junction. If $I_J = I_c \sin(\varphi+\alpha)$ (where $\alpha = 0, \pi$), for a 0-junction $I_J(\pi/2) \equiv I_J^{\pi/2} = I_c$, while for a π-junction $I_J^{\pi/2} = -I_c$. We thus calculate the supercurrent from Eq. (110) at $\varphi = \pi/2$ to compare with experimental data, as the values of I_{SW} correspond to maximal current values in the DQD Josephson junction. Details on the model can be found in the Supplementary Material of paper V.

Figure 36(a) shows the calculated $I_J^{\pi/2}$ in the DQD Josephson junction for a coupling $t \approx 0$ between the QDs as a function of the orbital energies ε_T and ε_B that correspond to the QD controlled by the TG and the BG respectively. In the regimes with odd total electron numbers $I_J^{\pi/2} < 0$, therefore the π phase dominates. For the regimes with even total electron numbers $I_J^{\pi/2} > 0$, indicating a 0 phase. Similarly to the experiment, the only exception is the (1,1) regime, which supports a π phase with significantly larger negative supercurrent. The same plot for $t = 0.2U$ (where U is the charging energy for each QD) is shown in Figure 36(b). The π phase survives only close to the center of the (1,1) regime and slight detunings lead to zero and subsequently positive $I_J^{\pi/2}$. This is also in good agreement with the experimental findings.

18 Summary and discussion for paper VI

In Section 12, we saw that the InAs/GaSb QW system can be driven to a 2D topological insulator regime hosting edge states [11, 12]. The edge states are robust against disorder that preserves time-reversal symmetry. In paper VI, the electronic band structure and the topological nature of a core-shell-shell InAs/GaSb NW were theoretically explored. Topological insulators are in the symmetry class AII [156] and are not predicted to have a topological phase in 1D. Never-

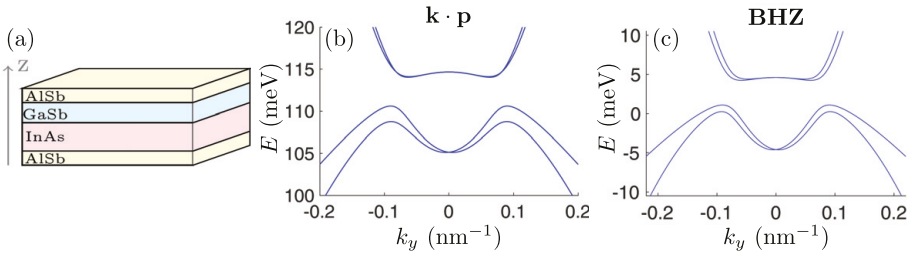

Figure 37: (a) Sketch of the InAs/GaSb QW with AlSb layers. Z is the growth direction. (b) Band structure of the InAs/GaSb QW calculated with the **k·p** theory for layer thicknesses $t_{\mathrm{AlSb}} = 10$ nm, $t_{\mathrm{InAs}} = 11$ nm, and $t_{\mathrm{GaSb}} = 5$ nm. (c) Band structure of the InAs/GaSb QW calculated with the BHZ model. The parameters were chosen to match the band structure in (b). The figure is adapted from paper VI.

theless, the studied NW is quasi-1D since it has a radial extent and it is worth revisiting its topological properties. The calculations were performed within the **k·p** theory framework using the Kane Hamiltonian [241] in the envelope function approximation. Details on this model can be found in Ref. [204]. The BHZ Hamiltonian [9] presented in Sections 11 and 12 was used to model a finite-length NW. In order to arrive at a NW geometry from the BHZ Hamiltonian, we used the discretized Hamiltonians presented in Section 13.4, and imposed periodic boundary conditions along one dimension. It was found that the NW hosts end states that do not enjoy general topological protection, yet they are robust against angular disorder.

Initially, the QW geometry sketched in Figure 37(a) was studied. Figure 37(b) shows the band structure calculated using $\mathbf{k} \cdot \mathbf{p}$ theory. With appropriate choices for the layer thicknesses, a large hybridization gap ($E_g^{\mathbf{k}\cdot\mathbf{p}} \approx 3.4$ meV) can be obtained. We adjusted the values of the BHZ parameters in order to match the band structure from the **k·p** calculations and Figure 37(c) shows the corresponding band structure. With this choice of parameters the system is in the topological regime.

Next, we studied a NW that is infinite along the z direction, see Figure 38(a). The NW has an AlSb core and InAs, GaSb shells[5]. For material thicknesses equal to the QW case, a much smaller hybridization gap was calculated for the NW from the **k·p** theory ($E_g^{\mathbf{k}\cdot\mathbf{p}} \approx 1$ meV). Such discrepancies are attributed to the fact that the same material thickness corresponds to a smaller volume for a shell closer to the core. Curvature effects could also play a role. Fine-

[5]For computational reasons the AlSb core was taken to be hollow, as shown in Figure 38(a). In an experiment, the hollow part would actually be filled with AlSb or some other insulating material. Our choice does not affect the results qualitatively, as we found that the wavefunctions around the gap decay fast in the central AlSb part.

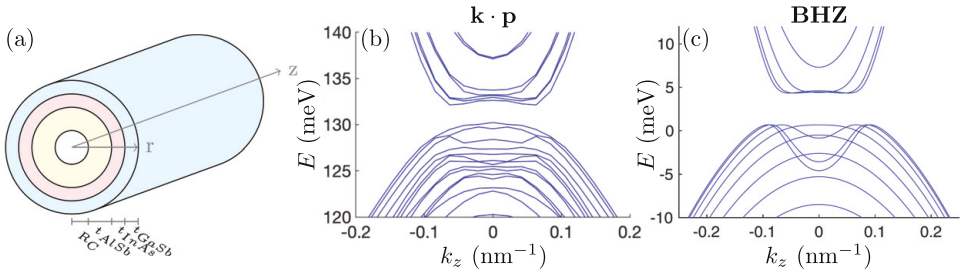

Figure 38: (a) Sketch of the InAs/GaSb NW with an AlSb hollow core. The radius of the hollow segment is R_C. (b) Band structure of the InAs/GaSb NW calculated with the $\mathbf{k}\cdot\mathbf{p}$ theory for $R_C = 10$ nm, $t_{AlSb} = 14$ nm, $t_{InAs} = 9.5$ nm, and $t_{GaSb} = 6.5$ nm. (c) Band structure of the InAs/GaSb NW calculated with the BHZ model. For the BHZ calculations the parameters are the same for the NW and the QW band structures. The figure is adapted from paper VI.

tuning the core and shell thicknesses a larger hybridization gap can be obtained ($E_g^{\mathbf{k}\cdot\mathbf{p}} \approx 1.9$ meV) and the corresponding NW band structure is shown in Figure 38(b). Figure 38(c) shows the NW band structure calculated with the BHZ Hamiltonian with the same parameters as for the QW. The hybridization gap persists in the BHZ case ($E_g^{\mathrm{BHZ}} \approx 3.7$ meV). Confinement effects do not play a role for the BHZ band structure, as the NW is modelled as a 2D system with periodic boundary conditions along one dimension, and the NW is a "rolled-up" 2D sheet without radial extent. For the same reason, curvature effects are also absent.

Finally, a finite-length NW was studied within the BHZ model. It was found that the NW hosts end states, well-separated in energy from the bulk states. The states are four-fold degenerate, two-fold degenerate in each Kramers sector. This is in contrast to the finite QW system where the states are only Kramers-degenerate. All end states were found to be highly localized at the NW ends.

In order to investigate whether the extra degeneracy is of topological nature, we introduce disorder to the NW. An energy splitting was observed with increasing disorder strength, but as long as time-reversal symmetry is not broken the states remain Kramers degenerate. A typical disorder realization is shown in Figure 39(a), where disorder is applied along the axial NW direction ($V_{\mathrm{dis}}^{\mathrm{ax}}$). Eigenvalues corresponding to bulk states are shown in black, while the ones corresponding to end states are shown in blue (finite angular momentum) and red (zero angular momentum). The green and purple dots mark Kramers-degenerate eigenvalues at finite disorder strength. Figure 39(b) shows the probability densities of the states corresponding to these eigenvalues along the NW. We see that the states corresponding to each pair are very well-localized at one of the NW ends. We conclude that the splitting due to disorder cannot be attributed to an overlap of the states and thus the states are not topologically protected. Inter-

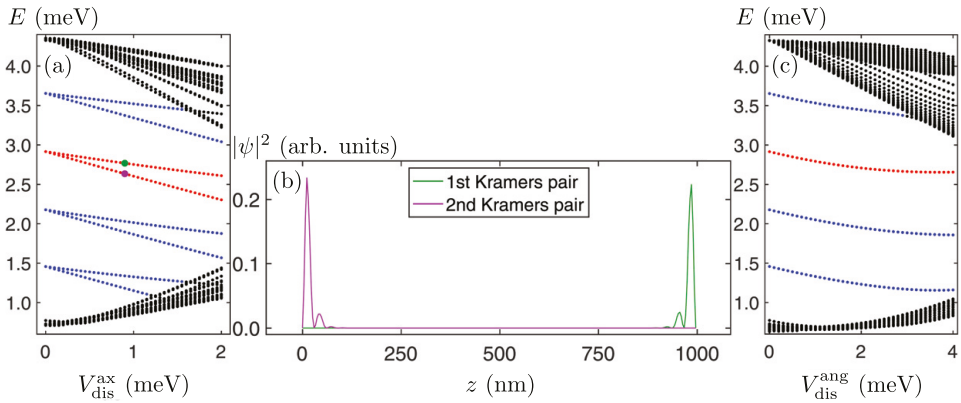

Figure 39: (a) Spectrum of the finite NW as a function of axial disorder strength. Eigenvalues corresponding to bulk states are shown in black while eigenvalues corresponding to end states in blue (finite angular momentum) and red (zero angular momentum). The green and purple dots denote Kramers-degenerate eigenvalues at finite disorder. (b) Probability density along the NW for the states corresponding to the eigenvalues marked with green and purple dots in (a). (c) Spectrum of the finite NW as a function of radial disorder strength. The color code is the same as in (a). The figure is adapted from paper VI.

estingly, the states are robust against disorder in the angular direction ($V_{\mathrm{dis}}^{\mathrm{ang}}$), as one can see in Figure 39(c), since the eigenvalues remain four-fold degenerate even for finite disorder.

References

[1] T. Ando, Y. Arakawa, K. Furuya, S. Komiyama, and H. Nakashima, editors. *Mesoscopic physics and electronics*. Springer Berlin Heidelberg, Berlin, 2011.

[2] B. Raj, editor. *Innovative applications of nanowires for circuit design*. IGI Global, 2021.

[3] Z. Li, H. H. Tan, C. Jagadish, and L. Fu. III-V semiconductor single nanowire solar cells: A review. *Advanced Materials Technologies*, 3(9): 1800005, 2018.

[4] A. J. Shields. Semiconductor quantum light sources. *Nature Photonics*, 1 (4):215–223, 2007.

[5] T.-H. Kim *et al.* Full-colour quantum dot displays fabricated by transfer printing. *Nature Photonics*, 5(3):176–182, 2011.

[6] D. Loss and D. P. DiVincenzo. Quantum computation with quantum dots. *Physical Review A*, 57(1):120–126, 1998.

[7] H.-A. Engel, L. P. Kouwenhoven, D. Loss, and C. M. Marcus. Controlling spin qubits in quantum dots. *Quantum Information Processing*, 3(1-5): 115–132, 2004.

[8] C. Kloeffel and D. Loss. Prospects for spin-based quantum computing in quantum dots. *Annual Review of Condensed Matter Physics*, 4(1):51–81, 2013.

[9] B. A. Bernevig, T. L. Hughes, and S.-C. Zhang. Quantum spin Hall effect and topological phase transition in HgTe quantum wells. *Science*, 314 (5806):1757–1761, 2006.

[10] M. König, S. Wiedmann, C. Brune, A. Roth, H. Buhmann, L. W. Molenkamp, X.-L. Qi, and S.-C. Zhang. Quantum spin Hall insulator state in HgTe quantum wells. *Science*, 318(5851):766–770, 2007.

[11] C. Liu, T. L. Hughes, X.-L. Qi, K. Wang, and S.-C. Zhang. Quantum spin Hall effect in inverted type-II semiconductors. *Physical Review Letters*, 100(23):236601, 2008.

[12] H. Irie, T. Akiho, F. Couëdo, K. Suzuki, K. Onomitsu, and K. Muraki. Energy gap tuning and gate-controlled topological phase transition in InAs/$In_xGa_{1-x}Sb$ composite quantum wells. *Physical Review Materials*, 4:104201, 2020.

[13] K. L. Wang, M. Lang, and X. Kou. Spintronics of topological insulators. In *Handbook of spintronics*, pages 431–462. Springer Netherlands, 2016.

[14] M. A. Kastner. Artificial atoms. *Physics Today*, 46(1):24–31, 1993.

[15] B. D. Josephson. Possible new effects in superconductive tunnelling. *Physics Letters*, 1(7):251–253, 1962.

[16] B. D. Josephson. The discovery of tunnelling supercurrents. *Reviews of Modern Physics*, 46(2):251–254, 1974.

[17] P. W. Anderson and J. M. Rowell. Probable observation of the Josephson superconducting tunneling effect. *Physical Review Letters*, 10(6):230–232, 1963.

[18] J. Clarke and A. I. Braginski, editors. *The SQUID handbook*. Wiley, 2004.

[19] P. Krantz, M. Kjaergaard, F. Yan, T. P. Orlando, S. Gustavsson, and W. D. Oliver. A quantum engineer's guide to superconducting qubits. *Applied Physics Reviews*, 6(2), 2019.

[20] M. Kjaergaard, M. E. Schwartz, J. Braumüller, P. Krantz, J. I.-J. Wang, S. Gustavsson, and W. D. Oliver. Superconducting qubits: Current state of play. *Annual Review of Condensed Matter Physics*, 11(1):369–395, 2020.

[21] H.-L. Huang, D. Wu, D. Fan, and X. Zhu. Superconducting quantum computing: A review. *Science China Information Sciences*, 63(8), 2020.

[22] P. Recher, E. V. Sukhorukov, and D. Loss. Andreev tunneling, Coulomb blockade, and resonant transport of nonlocal spin-entangled electrons. *Physical Review B*, 63:165314, 2001.

[23] L. Hofstetter, S. Csonka, J. Nygård, and C. Schönenberger. Cooper pair splitter realized in a two-quantum-dot Y-junction. *Nature*, 461(7266):960–963, 2009.

[24] L. G. Herrmann, F. Portier, P. Roche, A. Levy Yeyati, T. Kontos, and C. Strunk. Carbon nanotubes as Cooper-pair beam splitters. *Physical Review Letters*, 104:026801, 2010.

[25] Z. Scherübl, A. Pályi, and S. Csonka. Probing individual split Cooper pairs using the spin qubit toolkit. *Physical Review B*, 89:205439, 2014.

[26] G. Fülöp *et al.* Magnetic field tuning and quantum interference in a Cooper pair splitter. *Physical Review Letters*, 115:227003, 2015.

[27] G. Wang *et al.* Singlet and triplet Cooper pair splitting in hybrid superconducting nanowires. *Nature*, 612(7940):448–453, 2022.

[28] Q. Wang, S. L. D. ten Haaf, I. Kulesh, D. Xiao, C. Thomas, M. J. Manfra, and S. Goswami. Triplet Cooper pair splitting in a two-dimensional electron gas. *arXiv:2211.05763*, 2022.

[29] A. Bordin *et al.* Controlled crossed Andreev reflection and elastic cotunneling mediated by Andreev bound states. *arXiv:2212.02274*, 2022.

[30] Y. Oreg, G. Refael, and F. von Oppen. Helical liquids and Majorana bound states in quantum wires. *Physical Review Letters*, 105(17):177002, 2010.

[31] R. M. Lutchyn, J. D. Sau, and S. Das Sarma. Majorana fermions and a topological phase transition in semiconductor-superconductor heterostructures. *Physical Review Letters*, 105(7):077001, 2010.

[32] A. Y. Kitaev. Unpaired Majorana fermions in quantum wires. *Physics-Uspekhi*, 44(10S):131–136, 2001.

[33] F. Wilczek. Majorana returns. *Nature Physics*, 5(9):614–618, 2009.

[34] J. Alicea. New directions in the pursuit of Majorana fermions in solid state systems. *Reports on Progress in Physics*, 75(7):076501, 2012.

[35] M. Leijnse and K. Flensberg. Introduction to topological superconductivity and Majorana fermions. *Semiconductor Science and Technology*, 27(12): 124003, 2012.

[36] R. Aguado. Majorana quasiparticles in condensed matter. *La Rivista del Nuovo Cimento*, 40:523, 2017.

[37] C. W. J. Beenakker. Search for non-Abelian Majorana braiding statistics in superconductors. *SciPost Physics Lecture Notes*, 15, 2020.

[38] C. Nayak, S. H. Simon, A. Stern, M. Freedman, and S. Das Sarma. Non-Abelian anyons and topological quantum computation. *Reviews of Modern Physics*, 80(3):1083, 2008.

[39] S. Das Sarma, M. Freedman, and C. Nayak. Majorana zero modes and topological quantum computation. *npj Quantum Information*, 1(1):15001, 2015.

[40] V. Lahtinen and J. K. Pachos. A short introduction to topological quantum computation. *SciPost Physics*, 3:021, 2017.

[41] Pasquale Marra. Majorana nanowires for topological quantum computation. *Journal of Applied Physics*, 132(23):231101, 2022.

[42] R. M. Martin. *Electronic structure*. Cambridge University Press, 2020.

[43] F. Bloch. Über die Quantenmechanik der Elektronen in Kristallgittern. *Zeitschrift für Physik*, 52(7-8):555–600, 1929.

[44] C. Kittel. *Introduction to solid state physics*. Wiley, 2004.

[45] H. Ibach and H. Lüth. *Solid-state physics*. Springer Berlin Heidelberg, 2009.

[46] L. Wu, K. Gu, and Q. Li. New families of large band gap 2D topological insulators in ethynyl-derivative functionalized compounds. *Applied Surface Science*, 484:1208–1213, 2019.

[47] M. Dresselhaus, G. Dresselhaus, S. Cronin, and A. Gomes Souza Filho. *Solid state properties*. Springer Berlin Heidelberg, 2018.

[48] A.F. J. Levi. *Essential semiconductor laser device physics*. IOP Publishing, 2018.

[49] P. Y. Yu and M. Cardona. *Fundamentals of semiconductors*. Springer Berlin Heidelberg, 2010.

[50] M. I. Dyakonov, editor. *Spin physics in semiconductors*. Springer Berlin Heidelberg, 2008.

[51] J. H. Davies. *The physics of low-dimensional semiconductors*. Cambridge University Press, 1997.

[52] C. Thelander, T. Mårtensson, M. T. Björk, B. J. Ohlsson, M. W. Larsson, L. R. Wallenberg, and L. Samuelson. Single-electron transistors in heterostructure nanowires. *Applied Physics Letters*, 83(10):2052–2054, 2003.

[53] M. Hjort *et al.* Electronic and structural differences between wurtzite and zinc blende InAs nanowire surfaces: Experiment and theory. *ACS Nano*, 8(12):12346–12355, 2014.

[54] K. A. Dick, C. Thelander, L. Samuelson, and P. Caroff. Crystal phase engineering in single InAs nanowires. *Nano Letters*, 10(9):3494–3499, 2010.

[55] C. W. J. Beenakker. Theory of Coulomb-blockade oscillations in the conductance of a quantum dot. *Physical Review B*, 44(4):1646–1656, 1991.

[56] S. Tarucha, K. Ono, T. Fujisawa, W. G. van DerWiel, and L. P. Kouwenhoven. Interactions, spins and the Kondo effect in quantum-dot systems. In *Electron Transport in Quantum Dots*, pages 1–42. Springer US, 2003.

[57] A. Fuhrer. *Phase coherence, orbital and spin states in quantum rings.* PhD thesis, ETH Zurich, 2003.

[58] M. Leijnse. *Transport spectroscopy and control of molecular quantum dots.* PhD thesis, Faculty of Mathematics, Computer Science and Natural Sciences, RWTH Aachen University, 2009.

[59] M. Nilsson. *Charge and spin transport in parallel-coupled quantum dots in nanowires.* PhD thesis, Division of Solid State Physics, Department of Physics, Lund University, 2018.

[60] H. Grabert and M. H. Devoret. *Single charge tunneling : Coulomb blockade phenomena in nanostructures.* Springer Science+Business Media, New York, 1992.

[61] S. De Franceschi, S. Sasaki, J. M. Elzerman, W. G. van der Wiel, S. Tarucha, and L. P. Kouwenhoven. Electron cotunneling in a semiconductor quantum dot. *Physical Review Letters*, 86(5):878–881, 2001.

[62] E. A. Laird, F. Kuemmeth, G. A. Steele, K. Grove-Rasmussen, J. Nygård, K. Flensberg, and L. P. Kouwenhoven. Quantum transport in carbon nanotubes. *Reviews of Modern Physics*, 87(3):703–764, 2015.

[63] D. M. Zumbühl, C. M. Marcus, M. P. Hanson, and A. C. Gossard. Cotunneling spectroscopy in few-electron quantum dots. *Physical Review Letters*, 93(25):256801, 2004.

[64] W. G. van der Wiel, S. De Franceschi, J. M. Elzerman, T. Fujisawa, S. Tarucha, and L. P. Kouwenhoven. Electron transport through double quantum dots. *Reviews of Modern Physics*, 75:1–22, 2002.

[65] R. Hanson, L. P. Kouwenhoven, J. R. Petta, S. Tarucha, and L. M. K. Vandersypen. Spins in few-electron quantum dots. *Reviews of Modern Physics*, 79(4):1217–1265, 2007.

[66] B. Goldozian, F. A. Damtie, G. Kiršanskas, and A. Wacker. Transport in serial spinful multiple-dot systems: The role of electron-electron interactions and coherences. *Scientific Reports*, 6(1), 2016.

[67] M. Nilsson, L. Namazi, S. Lehmann, M. Leijnse, K. A. Dick, and C. Thelander. Single-electron transport in InAs nanowire quantum dots formed by crystal phase engineering. *Physical Review B*, 93(19):195422, 2016.

[68] M. Nilsson, I-J. Chen, S. Lehmann, V. Maulerova, K. A. Dick, and C. Thelander. Parallel-coupled quantum dots in InAs nanowires. *Nano Letters*, 17(12):7847–7852, 2017.

[69] M. Nilsson, F. Viñas Boström, S. Lehmann, K. A. Dick, M. Leijnse, and C. Thelander. Tuning the two-electron hybridization and spin states in parallel-coupled InAs quantum dots. *Physical Review Letters*, 121(15): 156802, 2018.

[70] C. Thelander, M. Nilsson, F. Viñas Boström, A. Burke, S. Lehmann, K. A. Dick, and M. Leijnse. Spectroscopy and level detuning of few-electron spin states in parallel InAs quantum dots. *Physical Review B*, 98(24):245305, 2018.

[71] S. Dorsch. *Transport in nanowire-based quantum dot systems: Heating electrons and confining holes*. PhD thesis, Department of Physics, Lund University, 2022.

[72] H. Kamerlingh Onnes. The superconductivity of mercury. *Communications Physics Laboratory University Leiden*, 122:122–124, 1911.

[73] D. van Delft and P. Kes. The discovery of superconductivity. *Physics Today*, 63(9):38–43, 2010.

[74] W. Meissner and R. Ochsenfeld. Ein neuer Effekt bei Eintritt der Supraleitfähigkeit. *Die Naturwissenschaften*, 21(44):787–788, 1933.

[75] F. London and H. London. The electromagnetic equations of the supraconductor. *Proceedings of the Royal Society of London. Series A - Mathematical and Physical Sciences*, 149(866):71–88, 1935.

[76] On the theory of superconductivity. In *Collected Papers of L.D. Landau*, pages 546–568. Elsevier, 1965.

[77] J. Bardeen, L. N. Cooper, and J. R. Schrieffer. Microscopic theory of superconductivity. *Physical Review*, 106(1):162–164, 1957.

[78] L. N. Cooper. Bound electron pairs in a degenerate Fermi gas. *Physical Review*, 104(4):1189–1190, 1956.

[79] H. Fröhlich. Theory of the superconducting state. I. The ground state at the absolute zero of temperature. *Physical Review*, 79(5):845–856, 1950.

[80] J. Bardeen and D. Pines. Electron-phonon interaction in metals. *Physical Review*, 99(4):1140–1150, 1955.

[81] M. Tinkham. *Introduction to superconductivity.* Dover Publication inc, 2004.

[82] H. Bruus and K. Flensberg. *Many-body quantum theory in condensed matter physics: An introduction.* Oxford University Press, 2004.

[83] E. Prada, P. San-Jose, M. W. A. de Moor, A. Geresdi, E. J. H. Lee, J. Klinovaja, D. Loss, J. Nygård, R. Aguado, and L. P. Kouwenhoven. From Andreev to Majorana bound states in hybrid superconductor–semiconductor nanowires. *Nature Reviews Physics*, 2020.

[84] A. F. Andreev. The thermal conductivity of the intermediate state in superconductors. *Soviet Physics-Journal of Experimental and Theoretical Physics*, 19:1228, 1964.

[85] A. F. Andreev. Electron spectrum of the intermediate state of superconductors. *Soviet Physics-Journal of Experimental and Theoretical Physics*, 22:455, 1966.

[86] G. E. Blonder, M. Tinkham, and T. M. Klapwijk. Transition from metallic to tunneling regimes in superconducting microconstrictions: Excess current, charge imbalance and supercurrent conversion. *Physical Review B*, 25(7):4515–4532, 1982.

[87] J. A. Sauls. Andreev bound states and their signatures. *Philosophical Transactions of the Royal Society A: Mathematical, Physical and Engineering Sciences*, 376(2125):20180140, 2018.

[88] T. Dvir *et al.* Realization of a minimal Kitaev chain in coupled quantum dots. *Nature*, 614(7948):445–450, 2023.

[89] A. Bordin, X. Li, D. van Driel, J. C. Wolff, Q. Wang, S. L. D. ten Haaf, G. Wang, N. van Loo, L. P. Kouwenhoven, and T. Dvir. Crossed Andreev reflection and elastic co-tunneling in a three-site Kitaev chain nanowire device. *arXiv:2306.07696*, 2023.

[90] R. P. Feynman, R. B. Leighton, and M. Sands. *The Feynman lectures on physics; New millennium ed.* Basic Books, New York, NY, 2010. Originally published 1963-1965.

[91] P. Mangin and R. Kahn. *Superconductivity.* Springer International Publishing, 2017.

[92] A. Zagoskin. *Quantum theory of many-body systems.* Springer International Publishing, 2014.

[93] J.-P. Cleuziou, W. Wernsdorfer, V. Bouchiat, T. Ondarçuhu, and M. Monthioux. Carbon nanotube superconducting quantum interference device. *Nature Nanotechnology*, 1(1):53–59, 2006.

[94] R. Maurand, T. Meng, E. Bonet, S. Florens, L. Marty, and W. Wernsdorfer. First-order $0-\pi$ quantum phase transition in the Kondo regime of a superconducting carbon-nanotube quantum dot. *Physical Review X*, 2: 011009, 2012.

[95] G. Kiršanskas, M. Goldstein, K. Flensberg, L. I. Glazman, and J. Paaske. Yu-Shiba-Rusinov states in phase-biased superconductor–quantum dot–superconductor junctions. *Physical Review B*, 92(23): 235422, 2015.

[96] A. V. Rozhkov and D. P. Arovas. Interacting-impurity Josephson junction: Variational wave functions and slave-boson mean-field theory. *Physical Review B*, 62:6687–6691, 2000.

[97] Y. Tanaka, A. Oguri, and A. C. Hewson. Kondo effect in asymmetric Josephson couplings through a quantum dot. *New Journal of Physics*, 9 (5):115–115, 2007.

[98] C. Karrasch, A. Oguri, and V. Meden. Josephson current through a single Anderson impurity coupled to BCS leads. *Physical Review B*, 77:024517, 2008.

[99] M. Governale, M. G. Pala, and J. König. Real-time diagrammatic approach to transport through interacting quantum dots with normal and superconducting leads. *Physical Review B*, 77:134513, 2008.

[100] T. Meng, S. Florens, and P. Simon. Self-consistent description of Andreev bound states in Josephson quantum dot devices. *Physical Review B*, 79 (22):224521, 2009.

[101] J. Eldridge, M. G. Pala, M. Governale, and J. König. Superconducting proximity effect in interacting double-dot systems. *Physical Review B*, 82: 184507, 2010.

[102] B. Sothmann, S. Weiss, M. Governale, and J. König. Unconventional superconductivity in double quantum dots. *Physical Review B*, 90(22): 220501(R), 2014.

[103] S. Weiss and J. König. Odd-triplet superconductivity in single-level quantum dots. *Physical Review B*, 96(6):064529, 2017.

[104] L. Yu. Bound state in superconductors with paramagnetic impurities. *Acta Physica Sinica*, 21(1):75–91, 1965.

[105] H. Shiba. Classical spins in superconductors. *Progress of Theoretical Physics*, 40(3):435–451, 1968.

[106] A. I. Rusinov. Superconcductivity near a paramagnetic impurity. *Journal of Experimental and Theoretical Physics Letters*, 9(2):85, 1969.

[107] A. Jellinggaard, K. Grove-Rasmussen, M. H. Madsen, and J. Nygård. Tuning Yu-Shiba-Rusinov states in a quantum dot. *Physical Review B*, 94(6): 064520, 2016.

[108] A. Jellinggaard. *Quantum dots coupled to a superconductor - Theory and experiments based on InAs nanowires.* PhD thesis, Center for Quantum Devices, Niels Bohr Institute, University of Copenhagen, 2016.

[109] I. Affleck, J.-S. Caux, and A. M. Zagoskin. Andreev scattering and Josephson current in a one-dimensional electron liquid. *Physical Review B*, 62: 1433–1445, 2000.

[110] B. Probst, F. Domínguez, A. Schroer, A. L. Yeyati, and P. Recher. Signatures of nonlocal Cooper-pair transport and of a singlet-triplet transition in the critical current of a double-quantum-dot Josephson junction. *Physical Review B*, 94(15):155445, 2016.

[111] K. Grove-Rasmussen, G. Steffensen, A. Jellinggaard, M. H. Madsen, R. Žitko, J. Paaske, and J. Nygård. Yu–Shiba–Rusinov screening of spins in double quantum dots. *Nature Communications*, 9:2376, 2018.

[112] O. Kürtössy, Z. Scherübl, G. Fülöp, I. E. Lukács, T. Kanne, J. Nygård, P. Makk, and S. Csonka. Andreev molecule in parallel InAs nanowires. *Nano Letters*, 21, 19:7929–7937, 2021.

[113] E. Majorana. Teoria simmetrica dell'elettrone e del positrone. *Il Nuovo Cimento*, 14(4):171–184, 1937.

[114] S.-Q. Shen. *Topological insulators - Dirac equation in condensed matter systems*. Springer Berlin Heidelberg, 2012.

[115] V. Mourik, K. Zuo, S. M. Frolov, S. R. Plissard, E. P. A. M. Bakkers, and L. P. Kouwenhoven. Signatures of Majorana fermions in hybrid superconductor-semiconductor nanowire devices. *Science*, 336(6084): 1003–1007, 2012.

[116] M. T. Deng, C. L. Yu, G. Y. Huang, M. Larsson, P. Caroff, and H. Q. Xu. Anomalous zero-bias conductance peak in a Nb–InSb nanowire–Nb hybrid device. *Nano Letters*, 12(12):6414–6419, 2012.

[117] A. D. K. Finck, D. J. Van Harlingen, P. K. Mohseni, K. Jung, and X. Li. Anomalous modulation of a zero-bias peak in a hybrid nanowire-superconductor device. *Physical Review Letters*, 110:126406, 2013.

[118] M. T. Deng, S. Vaitiekėnas, E. B. Hansen, J. Danon, M. Leijnse, K. Flensberg, J. Nygård, P. Krogstrup, and C. M. Marcus. Majorana bound state in a coupled quantum-dot hybrid-nanowire system. *Science*, 354(6319): 1557–1562, 2016.

[119] F. Nichele *et al.* Scaling of Majorana zero-bias conductance peaks. *Physical Review Letters*, 119:136803, 2017.

[120] R. M. Lutchyn, E. P. A. M. Bakkers, L. P. Kouwenhoven, P. Krogstrup, C. M. Marcus, and Y. Oreg. Majorana zero modes in superconductor–semiconductor heterostructures. *Nature Reviews Materials*, 3(5):52–68, 2018.

[121] M. Aghaee *et al.* (Microsoft Quantum). InAs-Al hybrid devices passing the topological gap protocol. *Physical Review B*, 107:245423, 2023.

[122] A. Yazdani, F. von Oppen, B. I. Halperin, and A. Yacoby. Hunting for Majoranas. *Science*, 380(6651):6651, 2023.

[123] K. Sengupta, I. Žutić, H.-J. Kwon, V. M. Yakovenko, and S. Das Sarma. Midgap edge states and pairing symmetry of quasi-one-dimensional organic superconductors. *Physical Review B*, 63:144531, 2001.

[124] K. T. Law, P. A. Lee, and T. K. Ng. Majorana fermion induced resonant Andreev reflection. *Physical Review Letters*, 103:237001, 2009.

[125] K. Flensberg. Tunneling characteristics of a chain of Majorana bound states. *Physical Review B*, 82:180516, 2010.

[126] D. E. Liu and H. U. Baranger. Detecting a Majorana-fermion zero mode using a quantum dot. *Physical Review B*, 84:201308(R), 2011.

[127] T. D. Stanescu, R. M. Lutchyn, and S. Das Sarma. Majorana fermions in semiconductor nanowires. *Physical Review B*, 84:144522, 2011.

[128] E. Prada, P. San-Jose, and R. Aguado. Transport spectroscopy of NS nanowire junctions with Majorana fermions. *Physical Review B*, 86:180503, 2012.

[129] S. Das Sarma, J. D. Sau, and T. D. Stanescu. Splitting of the zero-bias conductance peak as smoking gun evidence for the existence of the Majorana mode in a superconductor-semiconductor nanowire. *Physical Review B*, 86:220506(R), 2012.

[130] L. Fidkowski, J. Alicea, N. H. Lindner, R. M. Lutchyn, and M. P. A. Fisher. Universal transport signatures of Majorana fermions in superconductor-Luttinger liquid junctions. *Physical Review B*, 85:245121, 2012.

[131] P. A. Ioselevich and M. V. Feigel'man. Tunneling conductance due to a discrete spectrum of Andreev states. *New Journal of Physics*, 15(5): 055011, 2013.

[132] J. J. He, T. K. Ng, P. A. Lee, and K. T. Law. Selective equal-spin Andreev reflections induced by Majorana fermions. *Physical Review Letters*, 112: 037001, 2014.

[133] J. Gramich, A. Baumgartner, and C. Schönenberger. Andreev bound states probed in three-terminal quantum dots. *Physical Review B*, 96(19):195418, 2017.

[134] T. Ö. Rosdahl, A. Vuik, M. Kjaergaard, and A. R. Akhmerov. Andreev rectifier: A nonlocal conductance signature of topological phase transitions. *Physical Review B*, 97(4):045421, 2018.

[135] G. C. Ménard *et al.* Conductance-matrix symmetries of a three-terminal hybrid device. *Physical Review Letters*, 124(3):036802, 2020.

[136] J. Danon, A. B. Hellenes, E. B. Hansen, L. Casparis, A. P. Higginbotham, and K. Flensberg. Nonlocal conductance spectroscopy of Andreev Bound states: Symmetry relations and BCS charges. *Physical Review Letters*, 124:036801, 2020.

[137] H. Pan, J. D. Sau, and S. Das Sarma. Three-terminal nonlocal conductance in Majorana nanowires: Distinguishing topological and trivial in realistic systems with disorder and inhomogeneous potential. *Physical Review B*, 103(1):014513, 2021.

[138] D. I. Pikulin *et al.* Protocol to identify a topological superconducting phase in a three-terminal device. *arXiv:2103.12217*, 2021.

[139] E. Prada, R. Aguado, and P. San-Jose. Measuring Majorana nonlocality and spin structure with a quantum dot. *Physical Review B*, 96:085418, 2017.

[140] D. J. Clarke. Experimentally accessible topological quality factor for wires with zero energy modes. *Physical Review B*, 96:201109(R), 2017.

[141] M.-T. Deng, S. Vaitiekėnas, E. Prada, P. San-Jose, J. Nygård, P. Krogstrup, R. Aguado, and C. M. Marcus. Nonlocality of Majorana modes in hybrid nanowires. *Physical Review B*, 98:085125, 2018.

[142] D. J. Clarke, J. D. Sau, and S. Tewari. Majorana fermion exchange in quasi-one-dimensional networks. *Physical Review B*, 84:035120, 2011.

[143] J. Alicea, Y. Oreg, G. Refael, F. von Oppen, and M. P. A. Fisher. Non-Abelian statistics and topological quantum information processing in 1D wire networks. *Nature Physics*, 7(5):412–417, 2011.

[144] J. D. Sau, D. J. Clarke, and S. Tewari. Controlling non-Abelian statistics of Majorana fermions in semiconductor nanowires. *Physical Review B*, 84: 094505, 2011.

[145] B. van Heck, A. R. Akhmerov, F. Hassler, M. Burrello, and C. W. J. Beenakker. Coulomb-assisted braiding of Majorana fermions in a Josephson junction array. *New Journal of Physics*, 14(3):035019, 2012.

[146] T. Karzig, F. Pientka, G. Refael, and F. von Oppen. Shortcuts to non-Abelian braiding. *Physical Review B*, 91:201102(R), 2015.

[147] D. Aasen *et al.* Milestones toward Majorana-based quantum computing. *Physical Review X*, 6(3):031016, 2016.

[148] M. Hell, J. Danon, K. Flensberg, and M. Leijnse. Time scales for Majorana manipulation using Coulomb blockade in gate-controlled superconducting nanowires. *Physical Review B*, 94:035424, 2016.

[149] D. J. Clarke, J. D. Sau, and S. Das Sarma. Probability and braiding statistics in Majorana nanowires. *Physical Review B*, 95:155451, 2017.

[150] P. Boross and A. Pályi. Braiding-based quantum control of a Majorana qubit built from quantum dots. *arXiv:2305.08464*, 2023.

[151] M. Leijnse and K. Flensberg. Parity qubits and poor man's Majorana bound states in double quantum dots. *Physical Review B*, 86:134528, 2012.

[152] C.-X. Liu, G. Wang, T. Dvir, and M. Wimmer. Tunable superconducting coupling of quantum qots via Andreev bound states in semiconductor-superconductor nanowires. *Physical Review Letters.*, 129:267701, 2022.

[153] S. S. Hegde and S. Vishveshwara. Majorana wave-function oscillations, fermion parity switches, and disorder in Kitaev chains. *Physical Review B*, 94:115166, 2016.

[154] C. Zeng, C. Moore, A. M. Rao, T. D. Stanescu, and S. Tewari. Analytical solution of the finite-length Kitaev chain coupled to a quantum dot. *Physcal Review B*, 99:094523, 2019.

[155] N. Leumer, M. Marganska, B. Muralidharan, and M. Grifoni. Exact eigenvectors and eigenvalues of the finite Kitaev chain and its topological properties. *Journal of Physics: Condensed Matter*, 32(44):445502, 2020.

[156] A. Altland and M. R. Zirnbauer. Nonstandard symmetry classes in mesoscopic normal-superconducting hybrid structures. *Physical Review B*, 55 (2):1142–1161, 1997.

[157] A. Kitaev, V. Lebedev, and M. Feigel'man. Periodic table for topological insulators and superconductors. In *AIP Conference Proceedings*. AIP, 2009.

[158] A. P. Schnyder, S. Ryu, A. Furusaki, A. W. W. Ludwig, V. Lebedev, and M. Feigel'man. Classification of topological insulators and superconductors. In *AIP Conference Proceedings*. AIP, 2009.

[159] S. Ryu, A. P. Schnyder, A. Furusaki, and A. W. W. Ludwig. Topological insulators and superconductors: Tenfold way and dimensional hierarchy. *New Journal of Physics*, 12(6):065010, 2010.

[160] A. W. W. Ludwig. Topological phases: Classification of topological insulators and superconductors of non-interacting fermions, and beyond. *Physica Scripta*, T168:014001, 2015.

[161] C.-K. Chiu, J. C. Y. Teo, A. P. Schnyder, and S. Ryu. Classification of topological quantum matter with symmetries. *Reviews of Modern Physics*, 88:035005, 2016.

[162] J. Cayao Diaz. *Hybrid superconductor-semiconductor nanowire junctions as useful platforms to study Majorana bound states*. PhD thesis, Department of Condensed Matter Physics, UAM, 2016.

[163] A. Tsintzis. Odd-frequency superconducting pairing in Kitaev based junctions. Master's thesis, Department of Physics, Uppsala University, 2018.

[164] M. M. Sharma, P. Sharma, N. K. Karn, and V. P. S. Awana. Comprehensive review on topological superconducting materials and interfaces. *Superconductor Science and Technology*, 35(8):083003, 2022.

[165] E. I. Rashba. Symmetry of energy bands in crystals of wurtzite type: I. Symmetry of bands disregarding spin-orbit interaction. *Soviet Physics - Solid State*, 1(368):80, 1959.

[166] E. I. Rashba and V. I. Sheka. Symmetry of energy bands in crystals of wurtzite type: II. Symmetry of bands including spin-orbit interaction. *Fizika Tverdogo Tela: Collected Papers*, 2(162):76, 1959.

[167] G. Bihlmayer, O. Rader, and R. Winkler. Focus on the Rashba effect. *New Journal of Physics*, 17(5):050202, 2015.

[168] E. I. Rashba. Properties of semiconductors with an extremum loop. 1. Cyclotron and combinational resonance in a magnetic field perpendicular to the plane of the loop. *Soviet Physics - Solid State*, 2(1109), 1960.

[169] G. Kells, D. Meidan, and P. W. Brouwer. Near-zero-energy end states in topologically trivial spin-orbit coupled superconducting nanowires with a smooth confinement. *Physical Review B*, 86:100503, 2012.

[170] J. Liu, A. C. Potter, K. T. Law, and P. A. Lee. Zero-bias peaks in the tunneling conductance of spin-orbit-coupled superconducting wires with and without Majorana end-states. *Physical Review Letters*, 109:267002, 2012.

[171] J. Cayao, E. Prada, P. San-Jose, and R. Aguado. SNS junctions in nanowires with spin-orbit coupling: Role of confinement and helicity on the subgap spectrum. *Physical Review B*, 91:024514, 2015.

[172] C.-X. Liu, J. D. Sau, T. D. Stanescu, and S. Das Sarma. Andreev bound states versus Majorana bound states in quantum dot-nanowire-superconductor hybrid structures: Trivial versus topological zero-bias conductance peaks. *Physical Review B*, 96:075161, 2017.

[173] C. Moore, C. Zeng, T. D. Stanescu, and S. Tewari. Quantized zero-bias conductance plateau in semiconductor-superconductor heterostructures without topological Majorana zero modes. *Physical Review B*, 98: 155314, 2018.

[174] C. Reeg, O. Dmytruk, D. Chevallier, D. Loss, and J. Klinovaja. Zero-energy Andreev bound states from quantum dots in proximitized Rashba nanowires. *Physical Review B*, 98:245407, 2018.

[175] O. A. Awoga, J. Cayao, and A. M. Black-Schaffer. Supercurrent detection of topologically trivial zero-energy states in nanowire junctions. *Physical Review Letters*, 123:117001, 2019.

[176] A. Vuik, B. Nijholt, A. R. Akhmerov, and M. Wimmer. Reproducing topological properties with quasi-Majorana states. *SciPost Physics*, 7:061, 2019.

[177] H. Pan and S. Das Sarma. Physical mechanisms for zero-bias conductance peaks in Majorana nanowires. *Physical Review Research*, 2:013377, 2020.

[178] R. Hess, H. F. Legg, D. Loss, and J. Klinovaja. Local and nonlocal quantum transport due to Andreev bound states in finite Rashba nanowires with superconducting and normal sections. *Physical Review B*, 104:075405, 2021.

[179] P. Bonderson, M. Freedman, and C. Nayak. Measurement-only topological quantum computation. *Physical Review Letters*, 101:010501, 2008.

[180] K. Flensberg. Non-abelian operations on Majorana fermions via single-charge control. *Physical Review Letters*, 106:090503, 2011.

[181] M. Hell, M. Leijnse, and K. Flensberg. Two-dimensional platform for networks of Majorana bound states. *Physical Review Letters*, 118(10): 107701, 2017.

[182] S. Plugge, A. Rasmussen, R. Egger, and K. Flensberg. Majorana box qubits. *New Journal of Physics*, 19(1):012001, 2017.

[183] T. Karzig *et al.* Scalable designs for quasiparticle-poisoning-protected topological quantum computation with Majorana zero modes. *Physical Review B*, 95:235305, 2017.

[184] R. S. Souto, K. Flensberg, and M. Leijnse. Timescales for charge transfer based operations on Majorana systems. *Physical Review B*, 101(8):081407, 2020.

[185] S. Krøjer, R. S. Souto, and K. Flensberg. Demonstrating Majorana non-Abelian properties using fast adiabatic charge transfer. *Physical Review B*, 105:045425, 2022.

[186] M. Leijnse and K. Flensberg. Scheme to measure Majorana fermion lifetimes using a quantum dot. *Physical Review B*, 84:140501(R), 2011.

[187] D. Rainis and D. Loss. Majorana qubit decoherence by quasiparticle poisoning. *Physical Review B*, 85:174533, 2012.

[188] J. C. Budich, S. Walter, and B. Trauzettel. Failure of protection of Majorana based qubits against decoherence. *Physical Review B*, 85:121405(R), 2012.

[189] A. Y. Kitaev. Fault-tolerant quantum computation by anyons. *Annals of Physics*, 303(1):2–30, 2003.

[190] T. Karzig, Y. Oreg, G. Refael, and M. H. Freedman. Universal geometric path to a robust Majorana Magic Gate. *Physical Review X*, 6:031019, 2016.

[191] F. Hassler, A. R. Akhmerov, C.-Y. Hou, and C. W. J. Beenakker. Anyonic interferometry without anyons: How a flux qubit can read out a topological qubit. *New Journal of Physics*, 12(12):125002, 2010.

[192] J. D. Sau, S. Tewari, and S. Das Sarma. Universal quantum computation in a semiconductor quantum wire network. *Physical Review A*, 82:052322, 2010.

[193] L. Jiang, C. L. Kane, and J. Preskill. Interface between topological and superconducting qubits. *Physical Review Letters*, 106:130504, 2011.

[194] P. Bonderson and R. M. Lutchyn. Topological quantum buses: Coherent quantum information transfer between topological and conventional qubits. *Physical Review Letters*, 106:130505, 2011.

[195] M. Leijnse and K. Flensberg. Quantum information transfer between topological and spin qubit systems. *Physical Review Letters*, 107:210502, 2011.

[196] J. D. Sau and S. Das Sarma. Realizing a robust practical Majorana chain in a quantum-dot-superconductor linear array. *Nature Communications*, 3 (964), 2012.

[197] Z. Scherübl, A. Pályi, and S. Csonka. Transport signatures of an Andreev molecule in a quantum dot–superconductor–quantum dot setup. *Beilstein Journal of Nanotechnology*, 10:363–378, 2019.

[198] M. He, H. Sun, and Q. L. He. Topological insulator: Spintronics and quantum computations. *Frontiers of Physics*, 14(4), 2019.

[199] M. Z. Hasan and C. L. Kane. Colloquium: Topological insulators. *Reviews of Modern Physics*, 82(4):3045–3067, 2010.

[200] X.-L. Qi and S.-C. Zhang. Topological insulators and superconductors. *Reviews of Modern Physics*, 83(4):1057–1110, 2011.

[201] J. K. Asbóth, L. Oroszlány, and A. Pályi. *A short course on topological insulators.* Springer International Publishing, 2016.

[202] K. von Klitzing, G. Dorda, and M. Pepper. New method for high-accuracy determination of the fine-structure constant based on quantized Hall resistance. *Physical Review Letters*, 45(6):494–497, 1980.

[203] K. von Klitzing *et al.* 40 years of the quantum hall effect. *Nature Reviews Physics*, 2(8):397–401, 2020.

[204] F. Viñas Boström. *Theory of electronic structure and transport in heterostructure nanowires.* PhD thesis, Division of Solid State Physics, Department of Physics, Lund University, 2020.

[205] D. G. Rothe, R. W. Reinthaler, C.-X. Liu, L. W. Molenkamp, S.-C. Zhang, and E. M. Hankiewicz. Fingerprint of different spin–orbit terms for spin transport in HgTe quantum wells. *New Journal of Physics*, 12(6):065012, 2010.

[206] C. W. Groth, M. Wimmer, A. R. Akhmerov, and X. Waintal. Kwant: a software package for quantum transport. *New Journal of Physics*, 16(6): 063065, 2014.

[207] K. Björnson. TBTK: A quantum mechanics software development kit. *SoftwareX*, 9:205–210, 2019.

[208] R. Duda, J. Keski-Rahkonen, J. Solanpää, and E. Räsänen. tinie – a software package for electronic transport through two-dimensional cavities in a magnetic field. *Computer Physics Communications*, 270:108141, 2022.

[209] P. Moin. *Fundamentals of engineering numerical analysis.* Cambridge University Press, 2009.

[210] R. Landauer. Electrical resistance of disordered one-dimensional lattices. *Philosophical Magazine*, 21(172):863–867, 1970.

[211] M. Büttiker. Four-terminal phase-coherent conductance. *Physical Review Letters*, 57(14):1761–1764, 1986.

[212] Y. Meir and N. S. Wingreen. Landauer formula for the current through an interacting electron region. *Physical Review Letters*, 68(16):2512–2515, 1992.

[213] F. B. Anders. Steady-state currents through nanodevices: A scattering-states numerical renormalization-group approach to open quantum systems. *Physical Review Letters*, 101(6):066804, 2008.

[214] H.-P. Breuer and F. Petruccione. *The theory of open quantum systems*. Oxford University Press, 2007.

[215] J. König, H. Schoeller, and G. Schön. Cotunneling at resonance for the single-electron transistor. *Physical Review Letters*, 78(23):4482–4485, 1997.

[216] H. Schoeller. A perturbative nonequilibrium renormalization group method for dissipative quantum mechanics. *The European Physical Journal Special Topics*, 168(1):179–266, 2009.

[217] M. Leijnse and M. R. Wegewijs. Kinetic equations for transport through single-molecule transistors. *Physical Review B*, 78(23):235424, 2008.

[218] J. N. Pedersen and A. Wacker. Tunneling through nanosystems: Combining broadening with many-particle states. *Physical Review B*, 72(19): 195330, 2005.

[219] J. N. Pedersen and A. Wacker. Modeling of cotunneling in quantum dot systems. *Physica E: Low-dimensional Systems and Nanostructures*, 42(3): 595–599, 2010.

[220] G. Kiršanskas, J. N. Pedersen, O. Karlström, M. Leijnse, and A. Wacker. QmeQ 1.0: An open-source Python package for calculations of transport through quantum dot devices. *Computer Physics Communications*, 221: 317–342, 2017.

[221] M. G. Schultz and F. von Oppen. Quantum transport through nanostructures in the singular-coupling limit. *Physical Review B*, 80:033302, 2009.

[222] N. Sedlmayr and C. Bena. Visualizing Majorana bound states in one and two dimensions using the generalized Majorana polarization. *Physical Review B*, 92(11):115115, 2015.

[223] N. Sedlmayr, J. M. Aguiar-Hualde, and C. Bena. Majorana bound states in open quasi-one-dimensional and two-dimensional systems with transverse Rashba coupling. *Physical Review B*, 93(15):155425, 2016.

[224] S. V. Aksenov, A. O. Zlotnikov, and M. S. Shustin. Strong Coulomb interactions in the problem of Majorana modes in a wire of the nontrivial topological class BDI. *Physical Review B*, 101(12):125431, 2020.

[225] R. Winkler. *Spin-orbit coupling effects in two-dimensional electron and hole systems*. Springer-Verlag GmbH, 2003.

[226] C. R. Pidgeon, D. L. Mitchell, and R. N. Brown. Interband magnetoabsorption in InAs and InSb. *Physical Review Journals Archive*, 154:737–742, 1967.

[227] G. W. Winkler, D. Varjas, R. Skolasinski, A. A. Soluyanov, M. Troyer, and M. Wimmer. Orbital contributions to the electron g factor in semiconductor nanowires. *Physical Review Letters*, 119(3):037701, 2017.

[228] F. Kuemmeth, S. Ilani, D. C. Ralph, and P. L. McEuen. Coupling of spin and orbital motion of electrons in carbon nanotubes. *Nature*, 452(7186): 448–452, 2008.

[229] S. Csonka, L. Hofstetter, F. Freitag, S. Oberholzer, C. Schönenberger, T. S. Jespersen, M. Aagesen, and J. Nygård. Giant fluctuations and gate control of the g-factor in InAs nanowire quantum dots. *Nano Letters*, 8 (11):3932–3935, 2008.

[230] H. A. Nilsson, P. Caroff, C. Thelander, M. Larsson, J. B. Wagner, L.-E. Wernersson, L. Samuelson, and H. Q. Xu. Giant, level-dependent g factors in InSb nanowire quantum dots. *Nano Letters*, 9(9):3151–3156, 2009.

[231] Y. Aharonov and D. Bohm. Significance of electromagnetic potentials in the quantum theory. *Physical Review*, 115(3):485–491, 1959.

[232] J.-L. Zhu, X. Yu, Z. Dai, and X. Hu. Aharonov-bohm oscillation modes in double-barrier nanorings. *Physical Review B*, 67(7):075404, 2003.

[233] J. Planelles, F. Rajadell, and J. I. Climente. Electron states in quantum rings with structural distortions under axial or in-plane magnetic fields. *Nanotechnology*, 18(37):375402, 2007.

[234] V. D. Pham, K. Kanisawa, and S. Fölsch. Quantum rings engineered by atom manipulation. *Physical Review Letters*, 123(6):066801, 2019.

[235] J. A. van Dam, Y. V. Nazarov, E. P. A. M. Bakkers, S. De Franceschi, and L. P. Kouwenhoven. Supercurrent reversal in quantum dots. *Nature*, 442 (7103):667–670, 2006.

[236] I. O. Kulik. Magnitude of the critical Josephson tunnel current. *Journal of Experimental and Theoretical Physics (U.S.S.R)*, 22(4), 1966.

[237] L. N. Bulaevskii, V. V. Kuzii, and A. A. Sobyanin. Superconducting system with weak coupling to the current in the ground state. *Journal of Experimental and Theoretical Physics (U.S.S.R)*, 25(7):314, 1977.

[238] B. I. Spivak and S. A. Kivelson. Negative local superfluid densities: The difference between dirty superconductors and dirty Bose liquids. *Physical Review B*, 43:3740–3743, 1991.

[239] A. V. Rozhkov and D. P. Arovas. Josephson coupling through a magnetic impurity. *Physical Review Letters*, 82:2788–2791, 1999.

[240] E. J. H. Lee, X. Jiang, M. Houzet, R. Aguado, C. M. Lieber, and S. De Franceschi. Spin-resolved Andreev levels and parity crossings in hybrid superconductor–semiconductor nanostructures. *Nature Nanotechnology*, 9(1):79–84, 2013.

[241] E. O. Kane. Band structure of indium antimonide. *Journal of Physics and Chemistry of Solids*, 1(4):249–261, 1957.

Scientific publications

Author contributions

Co-authors are abbreviated as follows:
Martin Leijnse (ML), Rubén Seoane Souto (RSS), Jeroen Danon (JD), Karsten Flensberg (KF), Florinda Viñas Boström (FVB), Michael Hell (MH), Heidi Potts (HP), I-Ju Chen (IJC), Malin Nilsson (MN), Sebastian Lehmann (SL), Kimberly Dick (KD), Claes Thelander (CT), Rousan Debbarma (RD), Calle Janlén Stenberg (CJS), Markus Aspegren (MA).

Paper I: Creating and detecting poor man's Majorana bound states in interacting quantum dots

I was the main responsible for developing the theoretical model. This involved both analytical and numerical calculations and writing simulation software. I also made all the figures and contributed significantly to the writing.

Paper II: Roadmap towards Majorana qubits and nonabelian physics in quantum dot-based minimal Kitaev chains

I was the main responsible for developing the theoretical model in most sections of the paper. This involved both analytical and numerical calculations and writing simulation software. I also made most of the figures and contributed significantly to the writing.

Paper III: Electrical control of spins and giant g-factors in ring-like coupled quantum dots

I was the main responsible for developing the tight-binding model and the perturbation theory analysis. This involved analytical calculations and writing simulation software. I was also responsible for writing the corresponding part of the manuscript, as well as a detailed theory section in the supplementary material.

Paper IV: Effects of parity and symmetry on the Aharonov-Bohm phase of a quantum ring

I supervised CJS who performed the theoretical calculations. I also wrote the corresponding part of the manuscript, as well as a detailed theory section in the supplementary material.

Paper V: Supercurrent $\pi - 0$ transition induced by orbital hybridization in a double quantum dot

I was the main responsible for developing the theoretical model. This involved writing simulation software. I was also responsible for writing the corresponding part of the manuscript and the theory section in the supplementary material.

Paper VI: Band structure and end states in InAs/GaSb core-shell-shell nanowires

I was the main responsible for developing the tight-binding model. This involved analytical calculations and writing simulation software. I was also responsible for writing the corresponding part of the manuscript.